PROPERTIES OF COLLOIDAL HARD SPHERES AND MONODISPERSE EMULSIONS STUDIED BY LIGHT SCATTERING

by

HU GANG

A dissertation submitted to the Graduate Faculty in Physics in partial fulfillment of the requirements for the degree of Doctor of Philosophy, The City University of New York.

1995

This manuscript has been read and accepted for the Graduate Faculty in Physics in satisfaction of the dissertation requirement for the degree of Doctor of Philosophy.

September 1995
9/12/95
Date

Prof. L.A. Ferrari
Chair of Examining Committee

September 1995
Date 9/15/95

Prof. J. Krieger
Executive Officer

Dr. D.A. Weitz

Prof. H.Z. Cummins

Prof. A. Lisyansky

Prof. J. Neuberger

Supervisory Committee

The City University of New York

Abstract

PROPERTIES OF COLLOIDAL HARD SPHERES AND MONODISPERSE EMULSIONS STUDIED BY LIGHT SCATTERING

by

Hu Gang

Adviser: Dr. David A. Weitz

We have studied the properties of two different kinds of colloidal systems using laser light scattering techniques. One is a latex dispersion, which consists of hard sphere particles dispersed in a liquid; the other is an emulsion, which consists oil droplets dispersed in water. Using recently developed diffusing-wave spectroscopy (DWS), we have investigated time dependent hydrodynamic interactions in concentrated hard sphere systems. By varying the particle size and the volume fraction, we can probe the self and collective diffusion coefficients and we first found the collective time-dependent diffusion coefficient shows clear evidence of scaling as well as the self-diffusion coefficient. The computer simulations further prove the scaling behavior.

The emulsions we fabricate in our laboratory have a very uniform droplet size. To compare with the hard sphere system, we have studied the dynamic properties of flexible liquid droplets. We find emulsions made of high viscosity oil droplets exhibit similar dynamic properties to hard sphere latex at relatively low volume fractions. As the volume fraction reaches ϕ_c, the critical volume fraction for the liquid-glass transition, emulsions

also shows an ergodic to non-ergodic transition. We incorporate mode-coupling theory (MCT) of the glass transition and show that emulsions experience a liquid-glass transition similar to a hard sphere system. However, we find obvious difference between the two systems, i.e. in emulsions, α relaxation persists on the glass side of the transition. We attribute this to the deformability and flexibility of the liquid droplets. We have investigated the dynamic properties on a wider range of length scales by combining the conventional dynamic light scattering (DLS) and DWS.

Finally, we focus our attention on the flexibility of liquid droplets. We have generalized the theory of DWS by incorporating the effects of amplitude fluctuations in the scattering intensity of the particles. We apply this new method to study the thermally induced fluctuations in the shape of spherical emulsion droplets whose geometry is controlled by surface tension. We study the volume fraction dependence of relaxation of the shape fluctuations, and find that higher modes of fluctuations can be excited, and that the interactions between the droplets can change the time scale of the relaxation. We find a remarkable scaling curve for the relaxation of the shape deformations of liquid droplets at different volume fractions.

Acknowledgments

I wish to acknowledge many people who have helped and encouraged me during my thesis research at Exxon Corporate Research Labs and my graduate course work at the University of New Mexico and the Queens College of the City University of New York.

Dave Weitz has been a wonderful adviser to me over the past four years. He introduced me to the exciting field of colloidal science that I would never imagined in my life. I greatly appreciate his efforts in helping me gaining my knowledge and ability. I heartily thank him for teaching me how to approach a problem "like a physicist!". I thank him for his continuous positive attitude on my slow response. With his guidance and sometimes "magic" touch, I reached the beautiful scientific achievement contained herein.

Jerome Bibette has been a nice friend who taught me how to make and purify monodisperse emulsions, which is critical for my research. Tom Mason and Al Krall deserve special thanks for offering their expertise on emulsion rheology and light scattering. Jing Liu and Ming Lai have been good friends who I knew in New Mexico and kindly introduced me to Dave Weitz.

I thank Prof. Herman Cummins for helpful discussions regarding my experimental results and mode coupling theory. His profound knowledge and conscientious attitude inspires me. I also thank Prof. Larry Ferrari who is always ready to help me with course work at Queens College. Among other faculty at Queens, Profs. N.G. Garcia, A. Lisyansky, J. Neuberger also helped me with the arrangement of course work.

I thank all my buddies at Exxon who played Ping Pong with me at spare time. To be honest, without them I would have experienced my most dry and miserable life during the past four years. Among them I would like to thank Henry Shao, Zhiquan Huang, Chuheng Liu, Ke Liu, Jun Li, Jiuzhi Xue, Yiping Feng, Xiaozhong Wu. I also ask them to forgive me for seldom letting them win. I also thank Ping Sheng, Zhaoqing Zhang for

their being challenging Ping Pong players. I will never forget the good time and good friends at Exxon even though I might not be able to remember some of my research I did here. Special thanks go to Keding Xia and his wife who helped in many ways when I was in difficulty. Qiyao Zhang has been a knowledgeable consultant for me on a lot of my ignorance at Exxon.

I wish to thank my entire family for their love and encouragement even though they are far away in China. My mother and father, Li Baoyun, Hu Bingkun, have always shown their love for me. My brother Hu Yi, my sister Hu Jing, have given similar love and support. This work is dedicated to them.

I am grateful to Exxon Research and Engineering Company for the financial support.

Table of Contents

List of Figures

the first peak in the structure factor, and thus reflect the effects of interparticle interactions.

141

Fig. 3.4 Schematic diagram of experimental setup.

142

Fig. 3.5 A typical correlation function obtained in the DWS experiments, for a 1-mm thick sample cell containing 0.77-μm-radius polystyrene spheres at ϕ=0.2. The data were collected for about 12 hours to improve the signal-to-noise ratio. The data have been normalized by the measured background, which is the square of the average intensity; this background has also been subtracted from the data. The solid line through the data is a fit to the functional form, scaled to the volume-fraction-dependent hydrodynamic time scale. The second decay atlonger times is due to fluctuations in the laser intensity.

143

Fig. 3.6 The correlation function with the laser fluctuations subtracted. Over four decades of decay can be observed. The inset shows the first few data points on a linear scale, and demonstrates the absence of afterpulsing effects down to the shortest time scales. The fluctuations at the shortest time scale result from the very narrow sample times used and represent the largest noise in the data. The solid line through the data is a fit to the functional form, scaled to the volume-fraction-dependent hydrodynamic time scale.

144

Fig. 3.7 Comparison of the values of l^* obtained by fitting the measured data to ensure that $[H(t)]$ goes to the expected value at long times (circles) with those values obtained by independent static transmission measurements (triangles) and with calculations based on Mie scattering and a structure factor calculated from the Percus-Yevick equation (line). The small deviations reflect the uncertainties inherent in each of these approaches,

CHAPTER I

INTRODUCTION

In this thesis, we present the investigation of new physics in several colloidal systems. Colloid science has its roots in nineteenth-century discoveries concerning the behavior of minute particles[1]. Scientific interest, along with technological applications, fostered continued growth in the field since new technological problems never cease appearing in, for example, the manufacture of synthetic dispersions for coatings, enhanced oil recovery, the development of new fuels, environmental pollution, ceramics fabrication, corrosion phenomena, biotechnology, and separation processes. In addition, monodisperse suspensions of colloidal particles of diverse sorts became readily available, advancing our understanding of fluid mechanics on the colloidal scale. New techniques made possible direct, accurate measurements of size, shape, and concentration, as well as the complex effects of the interactions between the micron or submicron particles.

Colloidal particles are suspended in a liquid and execute Brownian motion. As is well known, Einstein first solved the problem of free Brownian motion[2]. In the study of Brownian particles the first concern has always been the observation of the mean square displacement of the particles. Light scattering has proved to be one of most powerful tools to experimentally study the static and dynamic properties of colloidal dispersions because the wavelength of light is comparable with the size of Brownian particles, and light is usually scattered strongly by the particles. With the advances of laser technology, laser light scattering experiments have become a chief tool for investigation of problems in chemistry, biology and physics in laboratory research and in industrial development. In this thesis, we extend the development of a recently developed technique called diffusing-wave spectroscopy[3-5] (DWS), which is an extension of dynamic light scattering[6,7] (DLS) to highly multiple scattering media. We apply DWS to study the dynamic

properties of two different kinds of colloidal systems. One is a latex dispersion, which consists of rigid particles dispersed in a liquid; the other is an emulsion, which consists of oil droplets dispersed in water. Diffusing-wave spectroscopy has a significant impact on the range of problems that can be addressed and on the type of systems that can be studied. This technique extends the analytical power of DLS to opaque samples such as concentrated suspensions without diluting or index matching. In addition, DWS can be used to study particle dynamics on length scales that are so short that the conventional DLS can not resolve their dynamics. In this chapter, we present an introduction to the underlying principles of DWS, and illustrate its applications to the study of the transient nature of hydrodynamic interactions between a particle and the surrounding fluid in latex dispersions. We also discuss the properties of emulsions and their importance from both scientific and practical standpoints.

The scattering of light from a coherent light source, such as a laser, from any random medium invariably results in a far field scattering pattern consisting of light and dark regions, called a speckle pattern. If the scattering medium changes in time, as for example if the scattering particles move, then the speckle pattern also changes in time, reflecting this motion. The analysis of the intensity fluctuations of a single speckle spot can provide information about the dynamics of the scattering medium, and this form of light scattering is called dynamic light scattering (DLS), or quasielastic light scattering. The traditional DLS experiment entails the measurement of the temporal autocorrelation function of intensity fluctuations of a speckle spot, and for singly scattered light, the time constant of the decay of this correlation function can be related to the dynamics of the scattering system through the knowledge of the scattering wave vector, q. This is a well developed form of light scattering spectroscopy, and traditional DLS has found many applications in the study of dynamics of a wide variety of systems.

If the light is multiply scattered, the far-field scattering pattern is still comprised of speckle spots, and these still fluctuate in time again reflecting the dynamics of the

scattering medium. The temporal correlation function of the intensity fluctuation can be measured in the same fashion as is done for traditional DLS. However, the interpretation of this correlation function is more difficult, and until recently, has limited the applicability of DLS to singly scattered light.

In the limit of very strongly multiply scattered light, the interpretation of the measured temporal correlation functions of the scattered intensity again becomes relatively straightforward. This form of dynamic light scattering is called diffusing-wave spectroscopy (DWS). It is based on the approximation that propagation of light in very strongly scattering media can be described as a diffusion process, which ignore any interference effects of the fields within the medium. Instead, only the intensity of the propagating light is considered. Actually, strong localization of light due to intense multiple scattering has not been observed since very few media scatter light sufficiently strongly. Therefore, the diffusion approximation for the propagation of light in strongly scattering media is quite adequate in almost all cases. Diffusing-wave spectroscopy exploits this approximation, taking advantage of the generality of these results. The second fundamental approximation inherent in DWS is in the treatment of the effect of the dynamics of the scatterers on the phase of light. Since each photon is scattered a large number of times as it is transported through the medium, the details of individual scattering events play a less critical role. In particular, the conservation of scattering momentum at every point along the full path can be neglected. Instead, the individual scattering events are approximated by the contribution of an average scattering event. Then the knowledge of the path length, obtained through the use of the diffusion approximation, determines the number of these average scattering events that contribute to each path. It is these two approximations that make the DWS approach tractable, and allow the calculation of the autocorrelation function. Instead of addressing the nature of the propagation of light through random media[8], DWS seeks to obtain new information

about the scattering medium itself. The development of DWS has been stimulated by its applicability in the study of a wide range of materials[9,10].

There are many similarities between diffusing-wave spectroscopy and conventional dynamic light scattering. Both entail the detection of the intensity of a single speckle spot of the scattered light and a measurement of its temporal fluctuations. In both cases, these fluctuations are characterized by their temporal autocorrelation function. In both cases, these intensity fluctuations reflect the dynamics of the scattering medium. By contrast, there are major differences in the length scales they probe. DWS is used to study a strongly scattering, opaque medium while DLS is used to a weakly scattering, transparent medium. DWS typically probes motions at a length scale much shorter than the wavelength of the light while DLS probes motions at a length scale about the wavelength. In traditional DLS, the decay of the temporal autocorrelation function is related to the dynamics of the medium through the length scale set by the inverse of the scattering wave vector, q^{-1}. Motion of the scatterers on this length scale leads to a change in the path length of the scattered light by a wavelength, resulting in a dephase of the detected light by 2π. The length scale of the motion of particles that causes the decay of the autocorrelation function of the multiply scattered light measured with DWS is much shorter. To cause the total path length of the scattered light to dephase by 2π, each individual scatterer needs to move only a very short distance since the light has been multiply scattered. This gives DWS a great advantage to detect very short length scale dynamics.

We concentrate our attention on the description of one key limit that DWS must address: media that not only scatter light very strongly, but are themselves strongly interacting. In particular, we are concerned with very strongly interacting colloidal systems. Because DWS exploits the very strong multiple scattering of light to probe the dynamics of the system, it is ideally suited for the study of highly concentrated suspensions. However a correct interpretation of the DWS data for these suspensions

requires knowledge not only about the effects of the multiple scattering of light, but also about the consequences of the high particle concentration, and the concomitant strong particle interactions, on the multiple scattering of the light. The effects of these interactions must be incorporated into the theory of DWS to make it a generally useful technique.

In an idealized suspension of monodisperse hard spheres, the dominant interactions are hydrodynamic; random forces arising from thermal fluctuations in the fluid excite fluctuations in the solid particle velocities which are subsequently damped by particle-induced viscous motion of the fluid. In the process, particles transmit hydrodynamic forces to one another on a time scale a^2/ν, where a is the particle radius and ν is the kinematic viscosity of the fluid. Since the diffusion coefficient of colloidal particles is about 5 orders of magnitude smaller than the kinematic viscosity of the fluid, there is a substantial time regime over which correlations in particle velocities specifically reflect the time evolution of the hydrodynamic interactions, without any additional complications due to the diffusion of the solid particles themselves. Our goal is to gain a deeper insight into the complex nature of hydrodynamic interactions by studying their temporal and spatial evolution. We use DWS to study the time dependent diffusion coefficient, in concentrated colloidal suspensions. At short times, the particle configuration is frozen and the diffusion coefficient probes the temporal and spatial evolution of hydrodynamic interactions, *via* their effects on the particle velocities. We find that both the time dependent self-diffusion coefficient and collective diffusion coefficient exhibit a surprising scaling behavior, suggesting that the suspension behaves as an effective medium for hydrodynamic interactions over a wide range of length scales and time scales.

Emulsions are oil-water mixtures, consisting of either oil droplets dispersed in water or water droplets dispersed in oil[11]. From a thermodynamic point of view, emulsions are metastable systems. They are prepared using an excess energy (mechanical in most cases) and the energy is stored in the form of surface energy at the interfaces of the

individual droplets. Coalescence of droplets may occur with time. In certain cases, e.g. with a proper choice of a surfactant, this time can be extremely long and no coalescence happens for years, making this kind of emulsion kinetically "stable". Moreover, unlike the case of microemulsions, the solubilization of one fluid in another is not limited by equilibrium thermodynamics. Under favorable conditions emulsification offers the opportunity to incorporate almost any ratio of one fluid in another. This leads to a wide range of important applications ranging from coating to cosmetics, and from foods to medicines[12]. A desirable emulsion that must be carefully stabilized to assist one stage of a process may be undesirable in another stage and necessitate a demulsification[13]. The interfacial properties are very important both in making an emulsion and in maintaining its stability.

We study emulsions which are made of oil droplets dispersed in water, stabilized by a surfactant, and focus our attention on their dynamic properties. Because of the deformability of the oil droplets, the volume fraction of the dispersed phase of the emulsions can be varied from zero to nearly 100%. At low volume fractions the suspension behaves like a viscous fluid, while at high volume fractions it behaves like a solid and exhibits viscoelastic characteristics. Since emulsions are one liquid dispersed in another liquid, they may differ from solid sphere colloidal dispersions in many ways, especially at high volume fractions. For example, both the stability and the rheological properties of emulsions differ significantly from hard sphere dispersions. A major limitation in elaborating a clear description of emulsions is the polydispersity in droplet sizes that is inherent in any emulsification process. This polydispersity complicates any interpretation of their static and dynamic properties. Fortunately, a purification process, called fractionated crystallization, was developed a few years ago, enabling the production of monodisperse emulsions[14], which provide an ideal model system for the study of liquid dispersions.

Oil droplets suspended in water execute Brownian motion because of thermal excitation in the fluid. Since oil droplets in water scatter light very strongly and they can be made very monodisperse, dynamic light scattering can be used to probe the motion of droplets. The deformability of liquid droplets allows the volume fraction of the dispersed phase to be increased to well above the highest possible value that hard spheres can reach. Similar to hard sphere dispersions, as the volume fraction approaches a critical volume fraction ϕ_c an emulsion also experiences the liquid-glass transition. Near this glass transition, the density fluctuations exhibit a two-step decay. The initial decay is connected with individual droplet diffusion; then it is followed by a regime where the decay of the correlation function is slowed down as each particle becomes trapped in a cage formed by its neighbors (in mode coupling theory, this is called the β-relaxation). Eventually the cage breaks up and long time diffusion leads to total loss of correlations (called the α-relaxation). At high volume fractions the motion of the deformed droplets are severely restricted by their neighbors and the system becomes non-ergodic, i.e., density fluctuations are partially frozen. Diffusing-wave spectroscopy is an ideal method to probe the particle motion on very short length scales. We take advantage of the multiple scattering and use DWS to detect the microscopic motion of the emulsion droplets. Understanding the dynamics of emulsions over a full range of volume fractions can give us deeper insight into many macroscopic properties of the system such as the rheological properties, the stability and the phase behavior of the emulsions. We are able to extract the elastic modulus of emulsions by measuring the mean square displacement from dynamic light scattering and comparing with the mechanical measurement. This technique provides a promising method to determine the modulus of complex fluids.

The liquid droplets are flexible and the interfaces of the droplets are subject to thermal fluctuations, so the shape of the emulsion droplets are dynamic variables. This extra degree of freedom introduced by thermal fluctuations may have consequences for the properties of emulsions. Especially as volume fraction is increased, the interaction

between droplets may change the macroscopic properties. It is of considerable technological importance to characterize and modify the interfacial behavior of emulsion systems. The physical aspects of the interfaces directly control the properties of the systems such as formation and stability. One important issue is the connection between coalescence and shape fluctuations of emulsion droplets. In order to induce coalescence, rupture of the liquid film between the droplets must take place. The rupture of the thin film can result from thermal or mechanical fluctuations, which results in the stretching of the liquid surface by means of a surface wave that can grow in amplitude and result in droplet coalescence. Detection of shape fluctuations of emulsion droplets directly probes the flexibility of droplets. It may lead to an improved understanding of stability and some rheological properties of the system.

We use DWS to probe the dynamics on very short length scales. However, to study shape fluctuations of emulsion systems, we must generalize the applicability of the theory for DWS. In the case that the scatterers are fluctuating liquid droplets, the scattered light carries not only information about translational motion but also about the dynamics of the fluctuating shapes of the liquid droplets. We generalize the theory of diffusing-wave spectroscopy to incorporate the effects of shape fluctuations on the scattering amplitude. The relaxation behavior of the shape fluctuations is probed and the volume fraction dependence of the fluctuations provides new insight into the interaction between liquid droplets.

This thesis is organized as follows: in Chapter II contains the principle of diffusing wave spectroscopy and experimental techniques to make DWS measurements. In Chapter III, we apply DWS to the study of the transient hydrodynamic interactions of latex suspensions and make comparisons with computer simulations. In Chapter IV, we briefly describe the principle and procedures to prepare monodisperse emulsions. In Chapter V, we present the investigations of dynamic behaviors of concentrated emulsions near the glass transition, which includes both conventional DLS and DWS results. Finally, we

present the study of shape fluctuations of interacting monodisperse emulsion droplets using DWS.

REFERENCES

1. W.B. Russel, D.A. Saville and W.R. Schowalter, *Colloidal Dispersions*, Cambridge; New York, 1989.
2. A Einstein, *Ann. d. Physik* **17** 549 (1905).
3. D.J. Pine, D.A. Weitz, P.M. Chaikin and E. Herbolzheimer, *Phys. Rev. Lett.* **60** 1134 (1988).
4. D.A. Weitz and D.J. Pine, *Dynamic Light Scattering*, W. Brown, ed. Oxford University Press, Oxford (1992).
5. D.J. Pine, D.A. Weitz, J.Z. Zhu and E. Herbolzheimer, *J. Phys.* France **51** 2101 (1990).
6. B.J. Berne and R. Pecora, *Dynamic light Scattering*, Wiley; New York, 1976.
7. B. Chu, *Laser Light Scattering*, Academic; New York, 1974.
8. A. Ishimaru, *Wave propagation and Scattering in Random Media.* Academic; New York, 1978.
9. J.X. Zhu, D.A. Weitz and R. Klein, in *Localization and Propagation of classical Waves in Random and Periodic Structures*, C.M. Soukoulis, Ed., Plenum, New York 1993.
10. D.J. Pine, D.A. Weitz, G. Maret, P.E. Wolf, P. Chaikin and E. Herbolzheimer, in *Scattering and Localization of Classical Waves in Random Media*, P. Sheng, Ed., World Scientific, Singapore, 1990.
11. P. Becher, *Emulsions: Theory and Practice* (Reinhold, New York, 1965).
12. K.J. Lissant, *Emulsion and Emulsion Technology*, vol. **6**, (M. DEkker, New York, 1974).
13. L.L. Schramm, *Emulsions:* Fundamentals and Applications in the Petroleum Industry, ACS, Washington, DC 1992.
14. J. Bibette, *J. Colloid Interface Sci.* **147** 474 (1991).

CHAPTER II

THE PRINCIPLES OF DIFFUSING-WAVE SPECTROSCOPY AND EXPERIMENTAL TECHNIQUES

In this chapter, we present the theoretical principles underlying diffusing-wave spectroscopy (DWS) and the experimental techniques of making DWS measurements. We do not attempt to exhaustively describe the details of the derivations of the analytical expressions. Some recent literature about the theoretical underpinnings of DWS have been published[1-3]. We here emphasize the physical picture and range of validity of this new spectroscopy. The scattering media can be studied using DWS are concentrated dispersions such as colloids, emulsions and other systems which are characterized by strong multiple scattering. We start by exploiting the diffusive nature of the transport of light in strongly scattering media and relate the temporal fluctuations of multiply scattered light to the motion of the scatterers. In this chapter we restrict our treatment to the translational motion of the scatterers. The generalization of DWS to include shape fluctuation dynamics will be given in Chapter VI. We then discuss the details of the experimental methods.

2.1 Principles of Diffusing-Wave Spectroscopy

In DWS, just as in conventional DLS, we measure the temporal fluctuations of the intensity in a single speckle spot of the scattered light, or in a single spatial coherence area. We parameterize these fluctuations by their autocorrelation function[4], $g_2(t)$. This is related directly to the autocorrelation function of the scattered electric fields,

$$g_1(t) = \frac{\langle E(0)E^*(t)\rangle}{\langle |E(0)|^2 \rangle}, \tag{2.1}$$

which is a simpler quantity to calculate. We begin by discussing a system of noninteracting particles and consider a colloidal suspension made up of identical, spherical particles, suspended in a fluid. In the limit of very low concentration, the self diffusion coefficient of these particles is given by the Stokes-Einstein relationship,

$$D_0 = \frac{k_B T}{6\pi\eta a}, \tag{2.2}$$

where k_B is Boltzmann's constant, T is the temperature, η the viscosity of the fluid, and a the particle radius. It is also convenient to define a characteristic time scale for diffusion of these particles by $\tau_0 = 1/k_0^2 D_0$, where $k_0 = 2\pi n/\lambda$, with n the index of refraction of the medium and λ the wavelength of light in vacuum. This is the time it takes for a particle to diffuse a distance of the wavelength of light divided by 2π.

To analyze the data obtained with DWS requires calculation of the autocorrelation function of the multiply scattered light[1,5]. This is calculated by dividing the photons into separate, diffusive paths. The distribution of these paths, and the probability that a photon will follow a path of length, s, is determined through the use of the diffusion equation for the light. The contribution of each path to the total correlation function is calculated, taking advantage of the long length of the path, and the concomitant large number of scattering events[6]. The total correlation function is determined by summing the contributions of all possible paths, weighted by their probabilities. If the scattering particles in each path are completely uncorrelated, we need consider only the contribution of an individual path. These can then be added, assuming that all interference that contributes to the signal comes only outside the sample, at the detector. Within this approach, the phase correlation of scattered waves within the medium are ignored, only scattered intensities are considered[6]. Thus the path followed by an individual photon

can be described as a random walk. This assumption is valid for nearly all cases of practical random systems. Therefore, the transport of light can be described in terms of intensity or energy density.

We begin by determining the correlation function of an nth-order path, consisting of n scattering events[6]. Since the number of scattering events is large, we approximate each event by an average scattering event, and neglect the conservation of momentum at each step. The scattering events are all independent, so the total correlation function is simply the product of n correlation functions of single scattering events, but averaged over scattering angle so as to reflect the average scattering event in the path. This gives,

$$g_1^n(t) = \left\langle e^{-i\mathbf{q}\cdot\Delta\mathbf{r}(t)} \right\rangle_q^n, \tag{2.3}$$

where the subscript q refers to an average over all scattering vectors, weighted by the scattering probability or form factor. At short times, we can use a cumulant expansion and bring the ensemble average to the exponent. Furthermore, for each scattering event, the scattering vector is independent of the particle's mean square displacement, each can be averaged independently, and the phase term is treated as a Gaussian random variable, giving,

$$g_1^n(t) = e^{-n\left\langle q^2 \right\rangle_q \left\langle \Delta r^2(t)/6 \right\rangle}, \tag{2.4}$$

where again the subscript q indicates an average over scattering vectors. Finally, we identify the path as $s = nl$, where l is the scattering mean free path of the light. Then, we use the relationship[7],

$$\frac{l}{l^*} = \frac{\left\langle q^2 \right\rangle}{2k_0^2}, \tag{2.5}$$

for $\left\langle q^2 \right\rangle$, where l^* is the transport mean free path, the distance over which a photon must travel before its direction is randomized. For noninteracting, diffusion particles,

$$\left\langle \Delta r^2(t) \right\rangle = 6D_0 t. \tag{2.6}$$

We can further simplify the expression by introducing the characteristic time scale, $\tau_0 = 1/k_0^2 D_0$. Then we obtain

$$g_1''(t) = e^{-2(t/\tau_0)(s/l^*)}. \tag{2.7}$$

The autocorrelation function does not depend on the scattering length, l, but only on the transport mean free path, l^*. This is the only parameter to be determined independently to relate the temporal correlation function to the motion of the scatterers. The expression in Eq. (2.7) has a simple physical significance: The first part of the exponent, $2t/\tau_0$, reflects the decay of the correlation function due to a single scattering event but averaged over all scattering vectors, weighted by the form factor of the particle. The additional quantity, s/l^*, reflects the effects of the multiple scattering. In following this diffusive path, the light is scattered through $n^* = s/l^*$ randomizing steps. It is only steps of order l^* that can lead to decay of the correlation function, as a single scattering step, of length l, is insufficient to change the direction of the light. Thus the decay rate of the total path is increased by a factor of n^*. Physically, the decay of this correlation reflects the time it takes for the total path length to change by a wavelength. This change results from the cumulative motion of a large number of particles. Thus long paths decay more rapidly since they are scattered from a large number of particles, and each individual particle must move a shorter distance, and hence take a shorter time, for the cumulative path to change by a wavelength. By contrast, shorter paths decay more slowly as the light is scattered by fewer particles and each individual particle must move a relatively larger distance, and hence take a longer time, before the total path changes by a wavelength. We note, however, that the correlation function for each path has a linear dependence in the exponential on both the path length, s, and on time, t.

To obtain the full autocorrelation function, we sum over the contributions from all paths, weighted by the probability $P(s)$, that the light follows the path,

$$g_1(t) = \int_0^\infty P(s) e^{-2(t/\tau_0)(s/l^*)} ds. \qquad (2.8)$$

With this expression, we implicitly assume that each path is uncorrelated with other paths and thus simply add the contributions of the different paths. The quantity $P(s)$ depends explicitly on the geometry of the experiment, but can be determined through the use of the diffusion equation for light. The method of its determination can be physically understood by considering what happens to a very narrow pulse of light incident on one side of the scattering medium. This light must travel roughly l^* into the medium before it has scattered a sufficient number of times that its transport becomes diffusive. The pulse exiting from the other side will reflect the distribution of paths followed by the diffusing photons. Some of the photons will follow very short paths and will exit the sample after a short time. Many more of the photons will follow longer paths and will be delayed before they exit. Some photons will follow very long paths and will exit much later. Thus, the pulse that exits the other side of the sample will exhibit considerable dispersion. Since the speed of light in the medium, c, is known, the dispersion in time of the transmitted pulse directly reflects the distribution of paths the light takes in passing through the medium. This allows $P(s)$ to be determined.

The diffusion equation can be solved for the geometry of the experiment to actually calculate the path distribution, $P(s)$. Since it is a partial differential equation, the boundary and initial conditions must be specified. The boundary conditions are chosen to ensure that there is no flux of diffusing photons into the sample at the boundaries[8,9]. The initial condition are chosen to provide a delta function in time of diffusing photons a distance l^* into the sample on the side that a laser is incident. We then solve the diffusion equation to obtain the flux of diffusing photons emitted from the sample at the detector, and use the transformation, $s = ct$ to obtain $P(s)$. In fact the solution of autocorrelation function is actually somewhat simplified by recognizing that Eq. (2.8) is the Laplace transform of

$P(s)$, so that we need only obtain the solution of the Laplace transform of the diffusion equation to recover the autocorrelation function directly.

The correlation function measured with DWS can be calculated for several experimentally relevant geometries[1-3,5]. Here, we consider the case where the light is transmitted through the sample, which we take to be a slab of infinite extent and of thickness, L. If the incident laser is focused to a point on one side of the sample, and the scattered light is collected from a point on the other side of the sample, on the same axis as the incident light, the normalized field correlation function is given by,

$$g_1(t) = \int_{(L/l^*)\sqrt{(6t/\tau_0)}}^{\infty} \left[A(s)\sinh s + e^{-s(1-4l^*/3L)} \right] ds \tag{2.9}$$

where

$$A(s) = \frac{\left(\frac{2l^*}{3L}s - 1\right)\left[\frac{2l^*}{3L}se^{-4sl^*/3L} + \left(\sinh s + \frac{2sl^*}{3L}\cosh s\right)e^{s(1-4sl^*/3L)}\right]}{\left(\sinh s + \frac{2sl^*}{3L}\cosh s\right)^2 - \left(\frac{2sl^*}{3L}\right)^2}. \tag{2.10}$$

If the incident laser beam is expanded to fill the full surface of the sample, the autocorrelation function is obtained by integrating over all the point sources on the incident side. This yields a closed form rather than an integral,

$$g_1(t) = \frac{\left(\frac{L}{l^*} + \frac{4}{3}\right)\sqrt{\frac{6t}{\tau_0}}}{\left(1 - \frac{8t}{3\tau_0}\right)\sinh\left[\frac{L}{l^*}\sqrt{\frac{6t}{\tau_0}}\right] + \frac{4}{3}\sqrt{\frac{6t}{\tau_0}}\cosh\left[\frac{L}{l^*}\sqrt{\frac{6t}{\tau_0}}\right]} \tag{2.11}$$

In either case, the form of the autocorrelation function is nearly exponential, and the characteristic decay time is $\tau_0(l^*/L)^2$. While complicated, these expressions are readily evaluated, and provide excellent agreement with the data.

Since DWS is ideally suited for the study of very concentrated suspensions, it is also essential to consider the correlation function for a suspension of strongly interacting particles. We can do this by analogy to the case of noninteracting particles[10]. However, when the particles are interacting, we can not ignore the coherent addition of the fields from some of the particles. Therefore, we must allow some of the paths to be correlated with each other, and we must coherently add the fields of these paths. Thus the total scattered field of the correlated n^{th} order scattering sequences is

$$E^n(q,t) = \sum_{i=1}^{N_\xi} E_i^n(t) = \sum_{k=1}^{N_\xi} \prod_{\alpha=1}^{n} b(q_i^\alpha) e^{-i\mathbf{q}_k^\alpha \cdot \mathbf{r}_k^\alpha(t)} \tag{2.12}$$

Here, the superscript α refers to one of the n scattering events that comprise each path. However, each of these α scattering events is coherently correlated with scattering events from some neighboring particles; this results in the correlation between adjacent diffusive paths. Thus, we allow N_ξ paths to be correlated, and denote the contribution from each scattering sequence which includes these correlation is

$$G_1^n(t) = \left\langle \sum_{i,j=1}^{N_\xi} \prod_{\alpha,\beta=1}^{n} b(q_i^\alpha) b(q_j^\beta) e^{-i\mathbf{q}_i^\alpha \cdot \mathbf{r}_i^\alpha(t) + i\mathbf{q}_j^\beta \cdot \mathbf{r}_j^\beta(0)} \right\rangle \tag{2.13}$$

To simplify this expression, we consider the scattering within the α^{th} scattering sequence. To remain fully correlated, the individual paths must follow very nearly the same route; thus we approximate the scattering wave vectors within the sequence, but for different paths, as being equal, so that $q_k^\alpha = q_k^\beta$. In addition, we make the further assumption that only one scattering event can occur in each correlation volume; this requires that $l > \xi$, where l is the scattering mean free path and ξ is the length scale over which the particles are correlated. For a system of concentrated hard spheres, ξ will extend over a length of several particle diameters. This places a constraint on the degree of the multiple scattering; it can not be so great as to have a high probability of several scattering events within each correlated volume. With these assumptions, particles from different scattering sequences

are not correlated in time, and terms with $\alpha \neq \beta$ average to zero, removing the product over β in Eq. 2.13. Since all the scattering particles are identical, we have

$$G_1^n(t) = \left\langle \prod_{\alpha=1}^{n} F(q^\alpha) \sum_{i,j=1}^{N_\xi} e^{-\mathrm{iq}^\alpha \cdot \left[\mathrm{r}_i^\alpha(t) - \mathrm{r}_j^\beta(0)\right]} \right\rangle \tag{2.14}$$

We can now identify the summation as the dynamic structure factor, $S(q,t)$ with the slight difference that the upper limit does not extend over the whole system, but rather only over a correlation volume. Thus,

$$N_\xi S(q^\alpha, t) = \left\langle \sum_{i,j=1}^{N_\xi} e^{-iq^\alpha \cdot \left[r_i^\alpha(t) - r_j^\beta(0)\right]} \right\rangle \tag{2.15}$$

where N_ξ is the number of particles within a correlation volume.

This relates the contribution of the correlation function from a diffusive light path to the dynamic structure factor that is measured in a single scattering experiment. The essential approximation is that only a single scattering event occurs within a correlation volume; the multiple scattering results from the transport of the light through many independent correlation volumes. As in the case of DWS from optically non-interacting particles, we assume that the scattering events from the different correlation volumes are statistically independent, and that there are a sufficient number of them that neglect the details of the momentum conservation between each scattering event. Thus, we replace each term in the product by the contribution of an average scattering event; we calculate this by averaging the correlation function from the single scattering sequence over q. Performing this q average and normalizing by the $t = 0$ value, we obtain the normalized correlation function for an n^{th} order sequence.

$$g_1^n(t) = \frac{\langle F(q)S(q,t)\rangle_q^n}{\langle F(q)S(q)\rangle_q^n}, \tag{2.16}$$

The average integral extends over all possible scattering angle from 0° to 180°, corresponding to $q = 2k_0$, where k_0 is the wave vector of the incoming light. To express this in a form suitable for use with the diffusion equation to describe the propagation of the light, we expand the dynamic structure factor at short time,

$$S(q,t) \approx S(q)\left[1 - \frac{q^2}{2S(q)} W(q,t)\right] \tag{2.17}$$

where we will define the meaning $W(q,t)$ later. We first use Eq. (2.17) to put Eq. (2.16) into a form that is suitable to use in the Laplace transform of Eq. (2.8). This can be accomplished by making a cumulant expression of Eq. (2.12),

$$g_1^n(t) = \left[1 - \frac{\frac{1}{2}\left\langle q^2 F(q) W(q,t)\right\rangle_q}{\left\langle F(q)S(q)\right\rangle_q}\right]^n, \tag{2.18}$$

and then by again restricting ourselves to short times and replacing Eq. (2.18) by the exponential,

$$g_1^n(t) \approx e^{-n\left\langle q^2 F(q) W(q,t)\right\rangle_q / 2\left\langle F(q)S(q)\right\rangle_q}. \tag{2.19}$$

We emphasize here that the averages over q in both Eqs (2.18) and (2.19) must now be performed while taking into account the interactions of the particles, and their effect on the light scattering. Finally, to express Eq. (2.19) in a form suitable for use with the diffusion equation for light we re-express the denominator of the exponent using the relation between the scattering and transport mean free paths for interacting particles[1,7],

$$\frac{l}{l^*} = \frac{\left\langle q^2 F(q) S(q)\right\rangle_q}{2k_0^2 \left\langle F(q)S(q)\right\rangle_q}. \tag{2.20}$$

From this, we obtain the normalized field autocorrelation function for nth-order paths,

$$g_1^n(t) \approx e^{-2k_0^2 (s/l^*)\left\langle q^2 F(q) W(q,t)\right\rangle_q / 2\left\langle q^2 F(q)S(q)\right\rangle_q} \tag{2.21}$$

Here s is the length of the path, while l^* is the transport mean free path for interacting system. This expression for the correlation function for nth-order paths is now suitable for use directly in the Laplace equation that describes the full correlation function, Eq. (2.8). Moreover, the result obtained for the transmission geometries, Eqs. (2.9), (2.10) and (2.11) can be used directly for interacting systems as well, by substituting t/τ_0 by $\left\langle q^2F(q)W(q,t)\right\rangle_q \Big/ 2\left\langle q^2F(q)S(q)\right\rangle_q$. Thus for interacting system, DWS measures an average over q of $W(q, t)$, weighted by $q^2F(q)$.

To make use of this result, we expand the dynamic structure factor for short times and thereby determine $W(q,t)$. The dynamic structure factor is

$$S(q,t)=\frac{1}{N}\left\langle \sum_{i,j=1}^{N} e^{-i\mathbf{q}\cdot\left[\mathbf{r}_i(t)-\mathbf{r}_j(0)\right]} \right\rangle \tag{2.22}$$

where $\mathbf{r}_i(t)$ is the position of ith particle at time t, and the summation extends over N particles. To expand this for short times we first use a theorem valid for ergodic systems, where the time and ensemble average are equivalent[11],

$$\frac{d^2}{dt^2}\left\langle A(0)\cdot B(t)\right\rangle=\left\langle \dot{A}(0)\cdot \dot{B}(t)\right\rangle \tag{2.23}$$

Substituting the dynamic structure factor in this equation, we obtain

$$\frac{d^2}{dt^2}S(q,t)=-\frac{1}{N}\sum_{i,j=1}^{N}\left\langle \mathbf{q}\cdot\mathbf{v}_i(t)\mathbf{v}_j(0)\cdot\mathbf{q}e^{-i\mathbf{q}\cdot\left[\mathbf{r}_i(t)-\mathbf{r}_j(0)\right]}\right\rangle \tag{2.24}$$

where $\mathbf{v}_i(t)$ is the velocity of the ith particle at time t. This enables us to express the dynamic structure factor in terms of the velocities of the particles. At very short times, the particles have not moved significantly from their positions at $t=0$, so the quantity in the brackets in the exponential can be replaced by its initial value, $\mathbf{r}_{ij}=\mathbf{r}_i(0)-\mathbf{r}_j(0)$. In making this approximation, we assume that the correlations in the structure of the particles

change much more slowly than the time scale of the particle motion being probed by DWS. Eq. (2.24) can be then written as

$$\frac{d^2}{dt^2}S(q,t) = -\langle \mathbf{q}\cdot\mathbf{v}(0)\mathbf{v}(t)\cdot\mathbf{q}\rangle - \frac{1}{N}\sum_{i\neq j}^{N}\left\langle \mathbf{q}\cdot\mathbf{v}_i(0)\mathbf{v}_j(t)\cdot\mathbf{q}\right\rangle e^{-i\mathbf{q}\cdot\mathbf{r}_{ij}} \tag{2.25}$$

where we have split the summation into two parts, the self part, where $i = j$, and the distinct part, where $i \neq j$. The first term is the velocity autocorrelation function of single particles, and reflects the self-diffusion of the particles, whereas the second term involves the correlation between velocities of different particles. To obtain $S(q,t)$ at short times, we integrate Eq. (2.25) twice giving

$$S(q,t) \approx S(q)\left[1 - \frac{q^2}{2S(q)}\left\{\frac{1}{3}\left\langle \Delta r^2(t)\right\rangle + \frac{1}{N}\sum_{i\neq j}^{N}\left\langle \hat{\mathbf{q}}\cdot\Delta\mathbf{r}_i(t)\hat{\mathbf{q}}\cdot\Delta\mathbf{r}_j(t)e^{-i\mathbf{q}\cdot\mathbf{r}_{ij}}\right\rangle\right\}\right] \tag{2.26}$$

from which we define

$$W(q,t) = \frac{1}{3}\left\langle r^2(t)\right\rangle + \frac{1}{N}\sum_{i\neq j}^{N}\left\langle \hat{\mathbf{q}}\cdot\Delta\mathbf{r}_i(t)\hat{\mathbf{q}}\cdot\Delta\mathbf{r}_j(t)e^{-i\mathbf{q}\cdot\mathbf{r}_{ij}}\right\rangle \tag{2.27}$$

and obtain the desired expansion for $S(q,t)$, used in Eq. (2.17). Diffusing wave spectroscopy provides a measure of $W(q,t)$, defined in Eq. (2.27). This measure is always with DWS, an average over q, weighted by $q^2F(q)$.

To better appreciate the physical significance of $W(q,t)$, it is useful to consider its behavior in some limiting cases. First, we consider the situation of noninteracting particles, in which case $S(q) = 1$ and the second term of Eq. (2.27) does not contribute because the value of r_{ij} is always sufficiently large compared to that of q to ensure that the summation over the exponential averages to zero. Then $W(q,t) \approx \frac{1}{3}\left\langle \Delta r^2(t)\right\rangle$, and is simply the mean square displacement of the particles. At longer times the expansion of the dynamic structure factor must reduce to the more familiar form that was originally developed for single scattering from interacting systems[12], and $W(q,t) = D_0H(q,t)t$,

where $H(q,t)$ reflects the effects of hydrodynamic interactions (we will give detailed discussion on $H(q,t)$ in Chapter III). In this case DWS probes quantities that are analogous to the case of DLS in the single scattering limit. We recall that DLS from interacting particles measures $D_{eff}(q) = D_0 H(q)/S(q)$. By comparison, DWS measures the same quantities, but averaged over q, and weighted by $q^2F(q)$[13,14],

$$\left[D_{eff}\right] = D_0 \frac{\left\langle q^2 F(q) H(q) \right\rangle_q}{\left\langle q^2 F(q) S(q) \right\rangle_q}. \tag{2.24}$$

We note that the evaluation of the average over q entails the integration,

$$\left\langle q^2 F(q) X(q) \right\rangle = \int q^3 F(q) X(q) dq. \tag{2.25}$$

This results in a factor of q^3 weighting the integral; a factor of q^2 because DWS is sensitive to the motion of the particles, and a factor of q to properly average over phase space. As a result, this average is heavily weighted towards the contributions at the large values of q.

While the approximation using $H(q)$ is often adequate, the reason for performing the expansion in terms of the velocity correlation functions is that DWS can, in principle, probe particle motion at sufficiently short length scales, and hence time scales, that the time dependence of $H(q)$ must be considered. When this must be done, we can still consider two different cases, both using Eq. (2.27) for $W(q,t)$. In the first case, when the particles are large, the summation in Eq. (2.27) again averages to zero, and $W(q,t)$ reduces to the mean square displacement. Physically, the particles are so large that only a single particle can fit into the average volume of a scattering event, which is roughly $\langle q \rangle^{-3}$, and DWS is sensitive only to the motion of the individual particles, or the self-diffusion coefficient. This is analogous to the case of DLS from large particles, which is also sensitive only to the self-diffusion coefficient, even for interacting particles[12]. It is only in the case of small particles that the full form of Eq. (2.27) must be used. Then DWS is sensitive to a combination of the self-diffusion coefficient of the particles, as well

as a term that reflects the relative motion of neighboring particles. In this case, more than one particle fits into the volume probed by a scattering event, and both the motion of individual particles and their relative motion affect the light scattering. This is again analogous to the situation of DLS, which measure collective diffusion if the particles are sufficiently small compared to q^{-1}. Thus DWS measures quantities that are very similar to DLS, but are averaged over q and weighted by $q^2F(q)$.

2.2 Experimental Methods

A schematic of the experimental setup is illustrated in Fig. 2.1. The Ar^+ laser operates in a single longitudinal and transverse (TEM_{00}) mode, at a wavelength of 514.5 nm. We use a temperature stabilized etalon inside the laser cavity to ensure lasing of a single longitudinal mode. This is essential because our correlator is sufficiently fast to be able to detect the beats between neighboring longitudinal modes, which occur at 125 MHz. Moreover, operating in a single mode ensures that the temporal correlation length of the light is larger than the longest diffusive light paths in the sample. As shown in Fig. 2.1, we use the transmission geometry.

The laser beam is focused to a point on the surface of one side of the sample. The multiply scattered light from the other side of the sample is imaged and coupled into an optical fiber detection optics.

The scattering sample cell is a thin optical cuvette, 1 cm wide. Thickness is chosen according to the transport mean free path of the scattering sample to ensure that L/l^* >20 so that the diffusion approximation could be safely applied. The sample is immersed in a water bath to allow the temperature to be maintained constant to better than 0.5 °K over the course of the measurements. This is essential to ensure that viscosity does not vary over the course of the data collection. Immersion in the water also reduces the effects of internal reflections at the interface[9]. The correlation functions are collected in

successive 10 minute intervals and the results are averaged. The sample cell is mounted on a motorized wheel and for a large size particle dispersion we rotate and shake the sample every 10 minutes to negate the effects of sedimentation.

To enable us to study the very fast phenomena of interest, we use a cross-correlation technique. The signal is divided into two equal portions and is detected with two photomultiplier tubes (PMT). The output of these are cross-correlated. This method reduces the deleterious effects of afterpulsing in the individual PMT's. Afterpulsing is the generation of secondary pulses triggered either by electron absorption on a dynode or the anode, or by ionization of atoms inside the tube. The occurrence of afterpulsing introduces a spurious correlation at short times in a single PMT, and this is greatly reduced by the cross-correlation of the signals from the two tubes. The cross-correlation technique also reduces the effects of dead time in the PMT and counting electronics. The dead time is the time for most amplifier discriminators used with PMTs to recover after detecting a photon. The time scale is on the order of tens of nanoseconds. Suppose at $t = 0$ a photon arrives and is registered by PMT1. At any small time τ later, a second photon arrives. This second photon will have 50% chance to be detected by PMT2. Since PMT2 did not register at $t = 0$, it is able to register the second photon and enable us to measure the desired intensity correlation function at times shorter than the dead time. So this cross correlation technique allows measurements at even faster time scales, provided that the count rate in each tube is not too large.

Our detection optics are fiber optic receivers. We use two different types, single mode and multi-mode. In both cases, the beam splitter is integrated into the fibers. The optical fiber beam splitter is a simple and an ideal solution to the cross correlation technique. It makes the experimental setup very compact and greatly simplifies the alignment[15-18]. The multimode fiber has a core diameter of 100 μm, and standard two pinhole optics is used to collect the light. A lens is used to image the fiber face onto the face of the sample and an aperture at the lens is adjusted to limit the range of scattering

vectors collected by the fiber core, which serves as the second pinhole. The multimode fiber here works as a light guide and feeds the received light into the PMT. Using the optical fiber as detection optics saves an additional aperture and allows remote location of the PMTs.

Single mode optical fibers have found their application in dynamic light scattering (DLS) in recent years[18,19]. They have been recognized as the ultimate receiving devices for DLS. Single mode fiber receivers offer a number of fundamental and practical advantages. From the practical point of view, they allow the construction of simple miniature DLS-instruments with a performance considerably surpassing that of the classical two-pinhole setup. Another advantage is they permit more rigorous analysis of a DLS experiment. Therefore, we here present more details about single mode fiber receivers since we believe they will ultimately replace other kinds of receiver optics.

Single mode fibers are optical waveguides with small core diameters (3-4 μm) that are comparable with the light wavelength. They are more than just light transmission guides with micrometer sized entrance aperture. The boundary conditions imposed on the electromagnetic field in a single mode wave guide are such that only one certain transverse structure, or only one mode of the field, is propagated, no matter what kind of input field impinges on the fiber entrance. Thus the fiber acts as a mode selective cavity. A practical single mode fiber receiver consists of collimation optics and a single mode fiber. The collimator is a micro graded index (GRIN) lens. The lens is made of gradient index material that refracts light continuously like a graded index wave guide. It is made into a rod shape with radial index profile which is typically parabolic: $n(r) = n_0(1 - Ar^2/2)$, where A is the gradient constant. The diameter of the rod ranges from 1 to 3 mm. Light travels through the rod in sinusoidal fashion. The GRIN lens offers several advantages over a conventional lens. Its geometric shape is easy to use and affords a more compact design. In the DLS setup, the scattered light is collected by a GRIN lens of 0.25 pitch, which is integrated on the fiber cable. A pitch of one describes the length of a GRIN rod

needed for light of a certain wavelength to execute one cycle, or sine wave. The 0.25 pitch lens focuses parallel incident light on the exit surface of the lens. The single mode fiber collects only the basic spatial mode of light on the focal plane of the GRIN lens. In classical two-pinhole detection optics, we measure the temporal correlation of a single speckle, while the single mode fiber seems to select much less than one coherence area from the scattered field. Equivalently, it picks the basic spatial mode and measures the correlation of time-varying speckle near the focal plane[20]. This results in a much larger intercept in the correlation function, while maintaining a high light-collection efficiency. In Reference 19 Ricka did theoretical calculations showing that the collection efficiency of a single mode fiber is four times higher than that of a two pinhole setup with a coherence factor of 0.8. The alignment of the apparatus is actually more accurate and easier. We just need to couple a laser beam into the exit end of the receiver and see if the output beam intersects the scattering volume of interest. Because of the high angular resolution of a single mode fiber receiver, we have great flexibility in arranging the receiver probe; we can even put the probe in the scattering medium itself. Then, a single mode fiber receiver offers the possibility of working with an arbitrarily large scattering volume and with an arbitrary working distance. In DWS the scattering volume is always much larger than that of conventional DLS; so without any confinement of scattering volume, the speckel size is much smaller. Using single mode fiber receivers, we don't need to care about scattering volume, the signal which can be transmitted through the receiver is always just what we want, no more, but no less. With the advances of silicon technology, we mention here an ideal detector companion to the fiber receiver is a single-photon avalanche diode[21,22], which can be made very compact. Therefore, the whole setup of laser light scattering can be practically made portable and as small as palm size.

REFERENCES

1. D.P. Pine, D.A. Weitz, G.Maret, P.E. Wolf, P.M. Chaikin and E. Herbolzheimer, Dynamical Correlations of Multiply Scattered Light, *in* "*Scattering and Localization of Classical Waves in Random Media*," P. Sheng, eds., World Scientific, Singapore (1990).
2. D.A. Weitz and D.J. Pine, Diffusing-Wave Spectroscopy, *in*: "*Dynamic Light Scattering*," W. Brown, eds., Oxford University Press, Oxford (1992).
3. D.A. Weitz, J.Z. Zhu, D.J. Durian and D.J. Pine, Principles and Applications of Diffusing-Wave Spectroscopy, *in*: "*Structure and Dynamics of Strongly Interacting Colloids and Supramolecular Aggregates in Solution*," S.H. Chen, J.S. Huang and P. Tartaglia, eds., Kluwer, Dordrecht (1992).
4. B.J. Berne and R. Pecora, "*Dynamic Light Scattering*: with Applications to Chemistry, Biology and Physics" (Wiley, New York 1976).
5. D.J. Pine, D.A. Weitz, J.X. Zhu and E. Herbolzheimer, J. Phys. France **51**, 2101 (1994).
6. G. Maret and P. Wolf, *Z. Phys.* **B65**, 409 (1987).
7. P.E. Wolf, G.Maret, E. Akkermans and R. Maynard, *J. Phys.* France **49**, 63 (1988).
8. A. Lagendijk, R. Vreeker and P. DeVries, *Phys. Lett.* **A136**, 81 (1989).
9. J.X. Zhu, D.J. Pine, D.A. Weitz, *Phys. Rev.* **A44**, 3948 (1991).
10. J.X. Zhu, D.A. Weitz and R. Klein, Dynamical Correlation of Multiply Scattered Light from Strongly Interacting Suspensions *in* "*Localization and Propagation of Classical Waves in Random and Periodic Structure*," Eds., C.M. Soukoulis, Plenum, New York 1993
11. J.P. Hansen and I.R. McDonald, *Theory of Simple Liquid*, Academic Press, 1985.
12. P.N. Pusey and R.J. Tough, *Faraday Disc. Chem. Soc.* **76**, 123 (1983).
13. S. Fraden and G. Maret, *Phys. Rev. Lett.* **65**, 512 (1990).

14. X. Qiu, X.L. Wu, J.Z. Xue, D.J. Weitz and P.M. Chaikin, *Phys. Rev. Lett.* **65**, 516 (1990).
15. T. Tanaka and G.B. Benedek, *Appl. Opt.* **14**, 189 (1975).
16. H. R. Haller, C. Destor and D.S. Cannel, *Rev. Sci. Instrum.* **54,** 973 (1983).
17. H.S. Dhadwal and B. Chu, *Rev. Sci. Instrum.* **60**, 845 (1989).
18. R.G.W. Brown, *Appl. Opt.* **26**, 4846 (1987).
19. Jaroslav Ricka, *Appl. Opt.* **32**, 2860 (1993).
20. K.A. O'Donnell, *J. Opt. Soc. Am.* **72**, 191 (1982).
21. R.G.W. Brown, K.D. Ridley, and J.G. Rarity, *Appl. Opt.* **26**, 2383 (1987).
22. H. Dautet, P. Deschamps, B. Dion, A.D. MacGregor, D. MacSween, R.J. McIntyre, C. Trottier, and P.P. Webb, *Appl. Opt.* **32**, 3894 (1993).

CHAPTER III

TEMPORAL AND SPATIAL DEPENDENCE OF HYDRODYNAMIC CORRELATION: SIMULATION AND EXPERIMENT

ABSTRACT

Time-dependent hydrodynamic interactions in a colloidal suspension of hard spheres are studied, both experimentally and through computer simulation. The focus is on the behavior at small wavevectors, which directly probes the temporal evolution of hydrodynamic interactions between nearby particles. The computer simulations show that the time dependent diffusion coefficient has the same functional form for all wavevectors, with a single characteristic scaling time for each length scale and for each volume fraction. Wavevector-averaged effective diffusion coefficients, measured experimentally using diffusing wave spectroscopy, also scale to the same functional form. In this case, the scaling time is dependent on both volume fraction and particle size; it decreases sharply with decreasing particle radius, reflecting the greater contribution from smaller wavevectors that is contained in the scattering from the smaller particles. For a direct comparison of simulation and experiment, we simulate the experimentally observed correlation functions, by averaging the wavevector-dependent computer-simulation data with the weighting appropriate to the experimental technique. Although the overall scaling is similar there are quantitative differences in the simulated and measured relaxation times. We suggest these differences are due to the compressibility of the suspension, and that the resultant pressure waves make an unexpectedly significant contribution to the hydrodynamic interactions.

3.1 Introduction

In this chapter we report experimental and numerical studies of the spatial and temporal evolution of hydrodynamic interactions in colloidal suspensions of micron sized spheres. When a sphere is set in motion by an external force or by a thermal fluctuation, it sets the surrounding fluid in motion by transferring momentum to it. Part of this momentum is carried off as sound waves, and spreads out in time over a spherical volume of radius $c_s t$ (c_s is the velocity of sound). The majority of the momentum transferred to the fluid diffuses throughout the system at a rate controlled by the kinematic shear viscosity of the fluid $\nu(\nu = \eta/\rho)$. Thus momentum that is initially localized near the particle spreads out over a spherical volume of radius $\sqrt{\nu t}$. This leads to a slow decay of the velocities of both the sphere and the surrounding fluid, which asymptotically vary as $(\nu t)^{-3/2}$ in three dimensions and as $(\nu t)^{-1}$ in two-dimensions. In concentrated suspensions, the hydrodynamic flow fields interact with the solid particles giving rise to a complex, many-body scattering problem. These hydrodynamic interactions are ubiquitous to all particle-fluid suspensions. The aim of this work is to study the development of these hydrodynamic interactions, both in time and in space. We do this by investigating time-dependent correlations in particle motion, in dilute to concentrated suspensions, using a combination of light-scattering experiments and numerical simulation.

Since the colloidal particles are much larger than fluid molecules, there is a very large time scale separation between the diffusion of fluid momentum and the diffusion of particles; the ratio D/ν is of theorder of 10^{-6}. Therefore there is a substantial time regime (typically between 10^{-8} and 10^{-5} seconds) during which the hydrodynamic flow fields and the particle velocities are evolving to a quasi-stationary state, whereas the particle coordinates are essentially fixed. Within this time range, we can study the temporal evolution of the hydrodynamic interactions without the added complications of changes in particle configuration. However, the experimental measurements must then probe particle

motion over distances of order tens of Angstroms. This can only be accomplished by using diffusing-wave spectroscopy (DWS),which is an extension of traditional dynamic light scattering into the multiple scattering regime.

Dynamic light-scattering experiments measure the phase shift between light scattered by different particles, via fluctuations in intensity of the scattered light; by time-correlation, *relative* motion between particles can be detected[1]. However, single-scattering experiments can only observe motion on length scales of order 1000 Å, a significant fraction of a particle radius. By the time the particles have moved such distances (*i.e.* times of the order of milliseconds), the hydrodynamic interactions have long since reached the quasi-static or "creeping-flow" limit. Recently, a multiple-scattering technique, DWS, has been used to dramatically increase the spatial and temporal resolution of light-scattering experiments[2-4]. Diffusing-wave spectroscopy works because the phase shifts from each scattering event accumulate in a stochastic fashion, thereby increasing the resolution by the square root of the number of scattering events. In the strong-scattering limit, the photon path is purely diffusive and the experimental data can be deconvolved to obtain information about particle motions at very short length scales (10^{-8} cm in these experiments), and therefore, at very short times (10^{-8} seconds). However, each of the many scattering events along a particular photon path has a different scattering angle, between 0^0 and 180^0; hence DWS probes an average over many different wavevectors[5], rather than a specific (and variable) wavevector as measured in a single-scattering experiment. Thus, while very short time scales can be resolved with DWS, the full spatial dependence of the hydrodynamic interactions can not be determined.

To overcome this limitation of DWS, and to better understand the complex behavior of the hydrodynamic interactions, we use numerical simulations[6.7] as an important complement to the experimental data. These simulations provide the essential wavevector dependent resolution of the time dependent hydrodynamic interactions. Our most important finding is that all the data, at any solids volume fraction, ϕ, and at any

wavevector, q, can be scaled onto a single master curve[8]. The functional form of this curve corresponds to the time dependent motion of a single suspended sphere, and can be calculated analytically. The data suggests that at a particular wavelength and volume fraction, the temporal evolution of hydrodynamic interactions is governed by a single relaxation time.

In order to directly compare the results of the numerical simulations with experimental DWS data, we have averaged the q-dependent simulation data over a range of wavevectors. We use a theoretically determined weighting factor, that depends on the particle radius we wish to compare with, and the wavelength of the laser light. We find that the wavevector-averaged data also scale to the single-sphere curve; the relaxation time now depends on particle radius, a, (instead of wavevector) and volume fraction. Similar scaling is also seen experimentally. However, a significant discrepancy between the simulated and measured relaxation times persists; we suggest that this discrepancy actually reflects an important role that is played by sound waves, which carry a significantly larger fraction of the momentum in the experiment than in the simulations.

The chapter is organized as follows. In the next section (3.2) the basic concepts of time and space dependent hydrodynamic interactions are introduced; we also discuss earlier results for both single-particle and collective diffusion. In section 3.3 we present a theoretical description of the use of DWS to probe these highly concentrated, and therefore strongly scattering suspensions; this presentation emphasizes the physical concepts rather than the formal description. The experimental set up and the experimental results are described in the two subsequent sections (3.4 and 3.5). In section 3.6 the simulation techniques are described and the key results are presented in the section 3.7. Section 3.7 also includes a direct comparison between the simulation results and the experimental results; the observed discrepancies motivate a discussion of the effects of sound waves. The chapter ends with a brief concluding section.

3.2. Previous Results

A. Self diffusion

It has been established, both experimentally[9,10], and by simulation[11], that the time evolution of the mean-square displacement of a tagged sphere, $\langle \Delta R^2(t) \rangle$, in a multi-particle suspension, can be characterized by a single relaxation time $\tau(\phi)$, at all solids volume fractions, ϕ. This scaling law is expressed in terms of the *hydrodynamic interaction function*

$$H(t) = \frac{1}{2D_0 t} \left\langle \frac{1}{3N} \sum_{i=1}^{N} \Delta R_i^2(t) \right\rangle; \tag{3.1}$$

$D_0 = k_B T / 6\pi\eta_0 a$ is the diffusion coefficient of an isolated sphere of radius a in a solvent of viscosity η_0. All the experimental and numerical data for $H(t,\phi)$ can be fitted to a single master curve $H_0(t^*)$, which is a function of a reduced time $t^* = t/\tau$, and a volume-fraction dependent scaling time $\tau(\phi)$:

$$H(t,\phi) = H^{\infty}(\phi) H_0(t/\tau(\phi)), \tag{3.2}$$

where $H^{\infty}(\phi)$ is the long-time limit of $H(t,\phi)$. To avoid confusion, we point out that our long-time limit refers to the development of hydrodynamic interactions, rather than to the motion of the solid particles themselves. Thus $H^{\infty}(\phi)$ is related to short-time self-diffusion coefficient $D_s(\phi) = D_0 H^{\infty}(\phi)$. If the scaling relations described by Eq. 3.2 are to be valid at low concentrations, it follows that $\tau(0) = \tau_0 = \rho a^2 / \eta_0$ and that $H_0(t^*)$ is the normalized mean-square displacement of an isolated sphere. If the fluid is assumed to be incompressible, then $H_0(t^*)$ is a known function of the reduced time and the ratio of the mass density of the solid particle to that of the fluid ρ_R [12]: its asymptotic expansions are

$$H_0(t^*) = \frac{1}{2\alpha} t^* - \frac{8}{15\sqrt{\pi\alpha^2}} + O(t^{*2}), \qquad t^* \ll 1, \tag{3.3}$$

$$H_0(t^*) = 1 - \frac{2}{\sqrt{\pi}} t^{*-1/2} + (1-\alpha) t^{*-1} + O(t^{*-3/2}), \qquad t^* \gg 1, \tag{3.4}$$

the parameter $\alpha = (2\rho_R + 1)/9$ includes the added-mass correction.

The experimental results[9] show that at higher volume fractions the time-dependent mean-square displacement has the same functional form as at low density, but with a relaxation time governed by the high-frequency viscosity of the suspension $\eta(\phi)$, rather than that of the pure fluid; *i.e.* $\tau(\phi) = \rho a^2 / \eta(\phi)$. Thus in this picture, the suspension behaves as an effective fluid medium with a viscosity $\eta(\phi)$. However, additional experiments[10], probing an even shorter time regime, suggested that the scaling may extend to very short times $t/\tau < 1$. This is somewhat puzzling, in that these times are too short for hydrodynamic interactions to propagate over typical interparticle separations by viscous diffusion. Numerical simulations[11], incorporating accurate hydrodynamic interactions and thermal fluctuations, also found a scaling of the mean-square displacement over a very wide time regime, from reduced times $t/\tau = 0.1$ on up.

The simulations reproduced the experimentally observed scaling with acceptable accuracy; our earlier analysis[11] is reproduced in Fig. 3.1a. However, the simulation data can actually be fitted more accurately by a slightly different time scaling $\tau(\phi) = H^{\infty}(\phi)\tau_0$, as shown in Fig. 3.1b; thus the scaling time is here proportional to the self-diffusion coefficient, rather than the inverse of the viscosity. If the time-dependence of the hydrodynamic interactions is a single-relaxation process, as suggested by the scaling relation described by Eq. 3.2, then we would expect that the velocity autocorrelation function,

$$J(t) = \left\langle \frac{1}{3N} \sum_{i=1}^{N} U_i(t) \cdot U(0) \right\rangle = \frac{d^2}{dt^2}[D_0 t H(t)], \tag{3.5}$$

will also scale with the same volume-fraction dependent relaxation time[13]. According to Eq. 3.2,

$$J_0(t,\phi) = \frac{k_B T}{M} \frac{H^{\infty}(\phi)\tau_0}{\tau(\phi)} J_0(t/\tau(\phi)), \tag{3.6}$$

where M is the particle mass and $J_0(t^*)$ is the velocity correlation function for an isolated sphere,

$$J_0(t^*)=\left(\alpha-\frac{1}{9}\right)\frac{d^2}{dt^{*2}}[t^*H_0(t^*)]. \tag{3.7}$$

The asymptotic expansions of $J_0(t^*)$ are

$$J_0(t^*)=\left(1-\frac{1}{9\alpha}\right)\left(1-\frac{2}{\sqrt{\pi\alpha}}t^{*1/2}\right)+O(t^*), \qquad t^*\ll 1; \tag{3.8}$$

$$J_0(t^*)=\left(\alpha-\frac{1}{9}\right)\frac{1}{2\sqrt{\pi}}t^{*-3/2}+O(t^{*-5/2}), \qquad t^*\gg 1. \tag{3.9}$$

It can be seen that at short times $J_0(t^*)$ does not asymptotically reach unity but to a smaller quantity $(1+\rho_R/2)^{-1}$. This is a consequence of the incompressible fluid model, used to derive the expression for $H_0(t)$; it neglects the part of the initial momentum that is carried off by sound waves. It is *assumed* that this initial relaxation is so rapid that it makes a negligible contribution to the mean-square displacement. While this is clearly true for an isolated sphere, the situation in a dense many-body suspension is more complex. We will discuss this point in section 3.7D, in the light of our results.

It is clear from Eq. 3.6 that the velocity correlation functions will *not* scale to a single curve unless the relaxation time is proportional to $H^\infty(\phi)$; *i.e.* $\tau(\phi)=H^\infty(\phi)\tau_0$. Thus it is interesting that precisely this scaling produces the best fit to the simulation data; the scaled velocity correlation functions are shown in Figs. 3.1c and 3.1d. The simulation data (scaled as in Figs. 3.1b and 3.1d by $H^\infty(\phi)\tau_0$) imply that there is a single relaxation process, so that a scaled velocity correlation function can be integrated to give a mean-square displacement with similar scaling. This is not true of the experimentally measured $H(t)$; they clearly scale better using the inverse of $\eta(\phi)$ rather than $D_S(\phi)$. Thus, it would not be possible to generate a scaled set of velocity correlation functions by just differentiating the scaled experimental $H(t)$ data with respect to time(Eq. 3.6 and 3.7). This suggests that there may be an additional relaxation process in the experiments which

is absent from the simulations. One possible cause is the different mass density ratios of solid particles and fluid. Experimentally $\rho_R \approx 1$, whereas in the simulations (for computational reasons, discussed in section 3.6) is usually around 10 and in all cases at least 5. If sound waves do make a significant contribution to the mean-square displacements in dense suspensions of neutrally buoyant particles, then we might expect a noticeable difference in relaxation times when compared with more massive particles used in the simulations, for which the sound-wave contributions would be much smaller. This is discussed in more detail later in the chapter (section 3.7D).

B. Collective diffusion

We investigate the spatial dependence of hydrodynamic interactions by probing a wavevector dependent analogue of the mean-square displacement, $H(q,t)$;

$$H(q,t) = \frac{1}{2D_0 t}\left\langle \frac{1}{N}\sum_{i,j=1}^{N} \hat{\mathbf{q}}\cdot[\mathbf{R}_i(t)-\mathbf{R}_i(0)][\mathbf{R}_j(t)-\mathbf{R}_j(0)]\cdot\hat{\mathbf{q}}e^{i\mathbf{q}\cdot\mathbf{R}_{ij}}\right\rangle, \qquad (3.10)$$

where $\hat{\mathbf{q}} = \mathbf{q}/q$. $\mathbf{R}_{ij} = \mathbf{R}_i - \mathbf{R}_j$. For large values of q, terms with $i \neq j$ average to zero; in this limit the time-dependent hydrodynamic interaction function $H(q,t)$ reduces to the one-particle interaction function $H(t)$, which is independent of q. At longer wavelengths (smaller q) collective motions make important contributions to $H(q,t)$. Thus, it is useful to decompose $H(q,t)$ into the sum of $H(t)$ and an interaction contribution $H_I(q,t)$;

$$H(q.t) = H(t) + H_I(q,t) \qquad (3.11)$$

The interaction contribution $H_I(q,t)$ consists exclusively of the terms with $i \neq j$ and directly measures the effects of interparticle hydrodynamic interactions; it shows how the trajectory of one particle is affected by the motion of its neighbors. By examining how the time evolution of $H_I(q,t)$ varies with q, we can begin to understand the spatial dependence of hydrodynamic interactions as well as the time dependence. In the DWS

experiments, it is not possible to measure $H(q,t)$ directly; instead what is measured is a weighted average over a range of wavevectors, denoted by $[H(t)]$. The weighting function that determines [H(t)] depends on the particle radius a (see section 3.3); thus, by varying the particle size, different ranges of wavevector can be probed. Surprisingly, the same scaling of $[H(t)]$ data, that was previously observed for large particles[9], is reproduced for small particles as well [8]. The interesting implication of this result is that the collective hydrodynamic interactions, $(H(q,t)$, must scale in a similar way to the single-particle interactions. To verify this supposition we have used computer simulations to calculate $H(q,t)$ directly, rather than the weighted average over q determined by DWS. Scaling *is* observed in the numerical simulations at each individual q; $H(q,t)$ can be scaled onto the single particle curve, with a scaling time, $\tau(q,\phi)$, that depends on both q and ϕ. The q dependence of the scaling time is similar to $H^{\infty}(q,\phi)$.

To compare the simulation results more directly with experiment, we have averaged the simulated $H(q,t)$ over different q values using a theoretically determined weighting function for each particle radius that matches the expected DWS weighting. We find a rather large discrepancy between the measured and predicted relaxation times, factors of 2 or more [8]. The differences in the single-particle (large-sphere) scaling times are not as large, about 35% at ϕ = 0.45%, and could even be explained by the combined uncertainties in the simulations and experiments. However, the differences in the scaling times for collective diffusion (small spheres) are too large to be accounted for by experimental uncertainty; we speculate that both discrepancies have the same physical origin, resulting from the effects of momentum transported away by the sound waves.

3.3. **Diffusing wave spectroscopy of optically interacting particles**

The key assumption in interpreting the results of a DWS experiment, is that the propagation of light through the scattering medium can be described by a diffusion

equation[2,14]. Thus the photon paths through the scattering volume are described by a random walk; the distribution of these paths is determined by a solution of the diffusion equation for the experimental geometry. Each photon path is ascribed a phase, which evolves in time with the motion of the scattering particles that comprise the path. Moreover, since each path is comprised of a different set of scattering particles, these paths are statistically uncorrelated. Thus, the field correlation function from each path can be calculated individually and the total correlation function is just the sum of the contributions from the individual paths, weighted by the probability that a diffusing photon follows that path. The correlation function of each path is calculated by summing the contributions of all the scattering events which make up the path. Since the light must scatter a large number of times in traversing the sample, the contributions of the individual scattering events are averaged over all scattering angles, with a weighting factor determined by the angular scattering probability of the light. The interpretation of DWS data is more complex than in the case of single-scattering experiments. To show how the data can be interpreted to extract information about particle motion, we present a summary of the theory of DWS for optically interacting particles[15,16]. Our derivation is motivated by a physical picture for the multiple scattering process, and explicitly demonstrates how DWS experiments probe an average of $H(q,t)$ as defined in Eq. 3.10. We obtain the same results as other less specific derivations[15], as well as other more formal diagrammatic techniques[17]. Before proceeding with the more complicated calculation for multiply scattered light, it is instructive to considerthe case of singly scattered light in order to indicate how $H(q,t)$ (Eq. 3.10) can be determined from a light scattering measurement.

In the weak-scattering limit, the scattered electric field from a suspension of identical particles is given by the sum of the scattered fields from each particle

$$E(q,t) = b(q)\sum_{i=1}^{N} e^{-iq\cdot\mathbf{R}_i(t)}; \tag{3.12}$$

here we neglect q-independent constants that will cancel in the normalization. The scattering amplitude $b(q)$ is related to the form factor of a particle,

$$F(q) = b(q)b^*(q). \tag{3.13}$$

The interpretation of dynamic light scattering experiments follows from the normalized electric-field autocorrelation function[18]

$$g_1(t) = \frac{\langle E(0)E^*(t)\rangle}{\langle E(0)E^*(0)\rangle} = \frac{S(q,t)}{S(q)}, \tag{3.14}$$

where the dynamic structure factor is defined by

$$S(q,t) = \left\langle \frac{1}{N}\sum_{i,j=1}^{N} e^{iq\cdot(\mathbf{R}_i(t)-\mathbf{R}_j(0))} \right\rangle \tag{3.15}$$

The static structure factor, $S(q) = S(q,0)$, reflects the coherence of light scattered by particles whose positions are correlated and which lie within a volume of order q^{-3}; the dynamic structure factor reflects the temporal decay of these correlations. A schematic representation of the contributions to the structure factor is illustrated in Fig. 3.2a. The lines represent the path of light scattered from each particle at a given **q**. Light scattered from particles within the correlated region is coherent (or at least has a coherent contribution); thus the fields scattered from each of the correlated particles must be added in order to calculate the total scattered intensity. However, particles outside the correlation volume do not scatter coherently with those inside it; on average, the randomness of the phases causes their scattered fields to cancel, so they make no contribution. Thus the total scattered intensity is an incoherent summation of contributions from each correlation volume. The scattering from each correlation volume

is again proportional to the dynamic structure factor, but summed over only the N_ξ particles within that volume,

$$S(q,t)=\left\langle \frac{1}{N_\xi}\sum_{i,j=1}^{N_\xi} e^{i\mathbf{q}\cdot(\mathbf{R}_i(t)-\mathbf{R}_j(0))}\right\rangle. \tag{3.16}$$

We will use this result below.

We can express $g_1(t)$ in terms of $H(q,t)$ by making use of the relation[19]

$$\frac{d^2}{dt^2}\left\langle \mathbf{A}(t)\cdot\mathbf{A}^*(0)\right\rangle=-\left\langle \dot{\mathbf{A}}(t)\cdot\dot{\mathbf{A}}^*(0)\right\rangle: \tag{3.17}$$

substituting the dynamic structure factor into Eq. 3.17, we obtain the relation

$$\frac{d^2}{dt^2}S(q,t)=-q^2\left\langle \frac{1}{N}\sum_{i,j=1}^{N}\hat{\mathbf{q}}\cdot\mathrm{U}_i(t)\hat{\mathbf{q}}\cdot\mathrm{U}_j(0)e^{i\mathbf{q}\cdot(\mathbf{R}_i(t)-\mathbf{R}_j(0))}\right\rangle, \tag{3.18}$$

where $\mathbf{U}_i(t)$ is the velocity of the i^{th} particle. In single-scattering experiments, particle motion can only be detected at relatively long times, when the velocity correlation function has decayed to zero. By contrast, in a DWS experiment the times are so short that the particles have not moved a significant distance compared with the wavelength of light; thus we can ignore the time dependence of the phase factor and approximate Eq. (3.18) as

$$\frac{d^2}{dt^2}S(q,t)=-q^2\left\langle \frac{1}{N}\sum_{i,j=1}^{N}\hat{\mathbf{q}}\cdot\mathrm{U}_i(t)\hat{\mathbf{q}}\cdot\mathrm{U}_j(0)e^{i\mathbf{q}\cdot\mathbf{R}_{ij}}\right\rangle, \tag{3.19}$$

Integrating Eq. 3.19 twice with respect to time, we obtain an expression for the structure factor which is valid for small particle displacements,

$$S(q,t)=S(q)\left[1-\frac{q^2}{2S(q)}\left\{\frac{1}{3N}\sum_{i=1}^{N}\left\langle \Delta R_i^2(t)\right\rangle+\left\langle \frac{1}{N}\sum_{i,j=1}^{N}\hat{\mathbf{q}}\cdot\Delta\mathbf{R}_i(t)\hat{\mathbf{q}}\cdot\Delta\mathbf{R}_j(0)e^{i\mathbf{q}\cdot\mathbf{R}_{ij}}\right\rangle\right\}\right], \tag{3.20}$$

where $\Delta\mathbf{R}_i(t)=\mathbf{R}_i(t)-\mathbf{R}_i(0)$. The two terms in braces are proportional to the self and interaction parts of $H(q,t)$ respectively (Eq. 3.11). Using the definition of the q-

dependent hydrodynamic interaction function $H(q,t)$ (Eq. 3.10), Eq. 3.20 can be rewritten as

$$S(q,t) = S(q)\left[1 - \frac{q^2 D_0 H(q,t) t}{S(q)}\right]. \tag{3.21}$$

We note that this form is similar to the traditional expansion of the dynamic structure factor in terms of a collective, q-dependent diffusion coefficient[19],

$$S(q,t) = S(q)e^{-q^2 D(q) t} \approx S(q)\left[1 - \frac{q^2 D_0 H(q,t) t}{S(q)}\right]; \tag{3.22}$$

here, the hydrodynamic interaction function, $H(q)$, is q-dependent, but not time dependent, since it describe slight scattering experiments that are insensitive to the time evolution of the hydrodynamic interactions. By contrast, we have now included an explicit time dependence to account for the temporal evolution of the hydrodynamic interactions. To extend this treatment to the case of multiple scattering, we must calculate the correlation function for a typical diffusive light path. The scattered field from a single path with n scattering events is the product of the scattered fields from each event,

$$E^n(t) = \prod_{\alpha=1}^{n} b(q^\alpha) e^{-i\mathbf{q}^\alpha \cdot \mathbf{R}^\alpha(t)} \tag{3.23}$$

$\mathbf{q}^\alpha$ is the scattering vector for the event α, and $\mathbf{R}^\alpha$ is the particle involved in this scattering event. However, each of these α scattering events is coherently correlated with scattering events from some neighboring particles; this results in the correlation between adjacent diffusive paths. Thus, we must coherently add the scattered fields from correlated paths, and the total scattered field of this n^{th} order scattering sequence is[16]

$$E^n(t) = \sum_{i=1}^{N_\xi} E_i^n(t) = \sum_{i=1}^{N_\xi} \prod_{\alpha=1}^{n} b(q_i^\alpha) e^{-i\mathbf{q}_i^\alpha \cdot \mathbf{R}_i^\alpha(t)}; \tag{3.23}$$

here the subscript k refers to one of the N_ξ correlated scattering paths. We schematically illustrate these coherent scattering paths in Fig. 3.2b, where we show the contributions

from two adjacent correlation volumes, α and β. The paths labeled i and j scatter from particles within each of the correlation volumes and must, therefore, be added coherently. The other scattering paths shown do not follow a path that retains their coherence, and therefore need not be added coherently. Thus, the time-dependent field correlation function for n^{th} order scattering sequences, which maintain their coherence is

$$G_1^n(t) = \left\langle E^n(t)E^{n*}(0)\right\rangle = \left\langle \sum_{i,j=1}^{N_\xi} \prod_{\alpha,\beta=1}^{n} b(q_i^\alpha)b(q_j^\beta)e^{-i\mathbf{q}_i^\alpha\cdot\mathbf{R}_i^\alpha + i\mathbf{q}_j^\beta\cdot\mathbf{R}_j^\beta} \right\rangle \tag{3.25}$$

To simplify this expression, we consider the many scattering paths within the α^{th} scattering event. To remain fully correlated, these individual paths must follow very nearly the same route; thus we approximate the scattering wave vectors within the event, but for different paths, as being equal, so that $\mathbf{q}_i^\alpha = \mathbf{q}_j^\beta$. In addition, we make the further assumption that onlyone scattering event can occur in each correlation volume; this requires that the scattering mean free path, l, is greater than the correlation length, ξ, which is of the order of a few particle diameters. This places a limit on the degree of multiple scattering; there should not be more than one scattering event in each correlated volume. With these assumptions, particles from different scattering events are not correlated in time, and terms with $\alpha \neq \beta$ average to zero; thus

$$G_1^n(t) = \left\langle \prod_{\alpha=1}^{n} F(q^\alpha) \sum_{i,j=1}^{N_\xi} e^{-i\mathbf{q}\cdot[\mathbf{R}_i^\alpha(t) - \mathbf{R}_j^\beta(0)]} \right\rangle \tag{3.26}$$

Here the summation extends over each correlation volume which contains N_ξ particles. We can identify this summation as the dynamic structure factor for the α^{th} scattering event, Eq. 3.16. Thus we can simplify Eq. 3.26 to

$$G_1^n(t) = \left\langle \prod_{\alpha=1}^{n} F(q^\alpha) NS(q^\alpha, t) \right\rangle \tag{3.27}$$

Equation 3.27 relates the contribution of the correlation function from a diffusive light path to the dynamic structure factor that is measured in a single scattering experiment. The essential approximation is that only a single scattering event occurs within a correlation volume; the multiple scattering results from the transport of the light through many independent correlation volumes. We assume that the scattering events from the different correlation volumes are statistically independent, and that there are a sufficient number of them that we can neglect the details of the momentum conservation between each scattering event in any path.

The ensemble average in Eq. 3.26 ensures that each scattering event includes contributions from many different paths. Thus each of the α scattering events in Eq.3.26 can be replaced by an average over all possible scattering vectors,

$$\frac{N_\xi \int_0^{2k_0} qF(q)S(q,t)dq}{\int_0^{2k_0} qdq}$$

The integral extends over all possible scattering angles from 0 to 180^0, corresponding to the limits q=0 and $q = 2k_0$; k_0 is the wave vector of the incoming light. The form factor $F(q)$ determines the relative weighting at each value of q; in addition, averaging over all possible scattering angles θ (see Fig. 3.2) introduces a further factor of q ($q = 2k_0 \sin \theta/2$). In terms of the average scattering,

$$G_1^n(t) = \left[\frac{N_\xi}{2k_0^2}\int_0^{2k_0} qF(q)S(q,t)dq\right]^n \tag{3.28}$$

and the normalized correlation function for an n^{th} order sequence is therefore

$$g_1^n(t) = \frac{\left[\int_0^{2k_0} qF(q)S(q,t)dq\right]^n}{\left[\int_0^{2k_0} qF(q)S(q)dq\right]^n}. \tag{3.29}$$

Using the short time expansion of $S(q,t)$, Eq. 3.21, we obtain

$$g_1^n(t)=\left[1-\frac{D_0 t\int_0^{2k_0} q^3F(q)H(q,t)dq}{\int_0^{2k_0} qF(q)S(q)dq}\right]^n=\exp\left\{-nD_0 t\frac{\int_0^{2k_0} q^3F(q)H(q,t)dq}{\int_0^{2k_0} qF(q)S(q)dq}\right\}. \quad (3.30)$$

In order to describe the multiple scattering by a diffusion equation, we must express $g_1^n(t)$ (Eq. 3.30) in terms of the path length of the scattered light $s=nl$, where l is the mean free path between scattering events [15]. However, the direction of a photon is not completely randomized by a single scattering event; instead there is a persistence in direction over a longer distance, the transport mean free path, l^* [20]. In terms of the scattering angle θ (see Fig. 3.2),

$$l^*=\frac{l}{1-\langle\cos\theta\rangle} \quad (3.31)$$

this is analogous to the persistence length of a semi-rigid polymer chain [21]. The scattering angle θ is geometrically related to k_0 and q by $1-\cos\theta=q^2/2k_0^2$; therefore

$$\frac{l^*}{l}=\frac{2k_0^2}{\langle q^2\rangle}=2k_0^2\frac{\int_0^{2k_0} qF(q)S(q)dq}{\int_0^{2k_0} q^3F(q)S(q)dq}. \quad (3.32)$$

Thus the correlation function for an n^{th} order scattering sequence, $g_1^n(t)$, can be expressed in terms of the contour length, s, of the scattering path and the *transport* mean free path, l^* [22],

$$g_1^n(t)=\exp\left\{-2D_0tk_0^2\frac{s}{l^*}\frac{[H(t)]}{[S]}\right\}; \quad (3.33)$$

The average of $H(q,t)$ measured by DWS, $[H(t)]$, is given by [22]

$$[H(q,t)]=\frac{\int_0^{2k_0} q^3F(q)H(q,t)dq}{\int_0^{2k_0} qF(q)dq}; \quad (3.34)$$

the square brackets around S indicates the same average over q. The transport mean free path, l^*, is the characteristic length for photon diffusion; l^* is the number of steps in a random walk that is statistically equivalent to the photon path. Thus the total field correlation function is [5,15]

$$g_1(t) = \int_0^\infty P(s) \exp\left\{-2D_0 t k_0^2 \frac{s}{l^*} \frac{[H(t)]}{[S]}\right\} ds \tag{3.35}$$

where $P(s)$ is the probability that diffusing photons follow a path of length s; it is calculated by solving the diffusion equation for thelight, in the experimental geometry, subject to appropriate initial and boundary conditions. We can rewrite Eq. 3.35 in terms of a reduced time,

$$t_D^* = 2D_0 k_0^2 \frac{[H(t)]}{[S]} \tag{3.36}$$

and a reduced contour length, $s^* = s/l^*$;

$$g_1(t_D^*) = \int_0^\infty P(s^*) e^{-s^* t^*} ds^*. \tag{3.37}$$

The solution of Eq. 3.37 has been discussed extensively elsewhere [14,23]; it depends on the experimental geometry. In this work the sample is slab of thickness L and of essentially infinite lateral extent. A transmission geometry is used; the incident light is focused on one side of the sample, and the scattered light is collected from a point on the other side of the sample. The correlation function is given by [23]

$$g_1(t) = \int_{\sqrt{3t_D^*} L/l}^\infty \left\{ A(s^*) \sinh s^* + e^{-s^*\left(1-\frac{4l^*}{L}\right)} \right\} ds^* \tag{3.38}$$

where

$$A(s^*) = \frac{\left(\frac{2l^*}{3L}s^* - 1\right)\left\{\frac{2l^*}{3L}e^{\frac{4s^*l^*}{3L}} + \left(\sinh s^* + \frac{2s^*l^*}{3L}\cosh s^*\right)e^{s^*\left(1-\frac{4l^*}{3L}\right)}\right\}}{\left(\sinh s^* + \frac{2s^*l^*}{3L}\cosh s^*\right)^2 - \left(\frac{2s^*l^*}{3L}\right)^2} \qquad (3.39)$$

These equations provide an excellent description of the correlation functions obtained from DWS experiments in the transmission geometry, as has been confirmed by studies of optically non-interacting particles [5]. Assuming that the data is described by these equations, a zero crossing routine can be used to invert the data and obtain t_D^* from the lower limit of the integral in Eq. 3.38. Then we can determine the time evolution of $[H(t)]$ through Eq. 3.36. The transport mean free path of the light, l^*, can be determined through another experimental measurement such as the total transmission, or by a theoretical calculation.

Even with the averaging over q inherent in DWS, it is still possible to obtain information about the q dependence of hydrodynamic interactions, by studying the scattering from particles of different sizes [8]. The relevant parameter is the product qa; thus the upper limit of integration in Eq. 3.34 is effectively $2k_0a$. Physically, this reflects the fact that the scattering dynamics are sensitive to the number of particles in a volume of order q^{-3}. If large particles are used, only a single particle can fit into this volume, and most of the contribution to the average arises from values of $qa > 1$. Then the DWS measurement reflects the high q limit of $H(q,t)$, corresponding to the time dependent self-diffusion coefficient $H(t)$. By contrast, if smaller particles are used, more than a single particle can fit into this volume, and the average reflects increasing contributions from values of $qa \leq \pi$, so that $H_I(q,t)$ makes a larger contribution.

The effects of using different size particles can be seen more quantitatively by examining the weighting factor in Eq. 3.34, $q^3F(q)$. The overall q^3 factor arises from

two contributions; a factor of q arises from the phase space available for scattering, while the remaining factor of q^2 arises because of the diffusive dynamics. The q^3 factor ensures that the dominant contribution to the average arises from the larger values of q. We plot $q^3F(q)$ as a function of qa in Fig. 3.3, for several of the particle sizes used in our experiments. The form factors were calculated using Mie theory [24], and the results for each particle size were normalized by their maximum value. The weighting factors are plotted to the maximum value of qa in each case, *i.e.* $2k_0^2$, where $k_0 = 16.24\mu\text{m}^{-1}$ The strong oscillations reflect the Mie resonances in the form factor. For the larger particles, the dominant contribution to the integral in Eq. 3.34 comes from values of qa greater than the first peak in the structure factor ($qa = \pi$); as a result the integral reflects the self contribution, $H(t)$, only. By contrast, for the smallest particles, all of the weight in the integral arises from values of qa less than the first peak of the structure factor, making the contribution of collective effects much more important, so that in this case $H_I(q,t)$ makes a significant contribution.

3.4. Experimental method

Our samples are aqueous suspensions of highly monodisperse polystyrene latex spheres. These particles are stabilized against aggregation by charges adsorbed on their surface; their Coulombic repulsion prevents the particles from touching when they approach one another. The range of this repulsive interaction is determined by the screening length, which is set by the total concentration of charges in the solution. Since the screening length is much smaller than the particle radius, the particle-particle interactions closely approximate those of hard spheres. We estimate that the screening length is roughly 50 Å, compared with a typical particle radius of 1 μm; for the smallest particles (radius 0.1 μm), we add additional acid to the solution to reduce the screening length still further, and ensure that it remains much less than the particle size. We believe

that the particle positions, as reflected by the pair correlation function, $g(r)$, are very well characterized by the hard sphere distribution. However, there is a possibility that the interactions between the particles will be affected by the slightly softened potential due to the finite range of the screened Coulombic repulsion. This will be increasingly likely for the smaller particles, where the screening length becomes a more appreciable fraction of the radius. Although we cannot rule out this possibility completely, we have no direct evidence for it.

The radii of the particles studied included 0.099 μm, 0.206 μm,0.380 μm, 0.765 μm and 1.55 μm; the precise values were determined by dynamic light scattering measurements of the hydrodynamic radius, performed at very low concentrations. This range in particle size allows us to probe both the high-q, single-particle limit of $H(q,t)$ (using the larger spheres), as well as collective motions at smaller qa (using the smaller spheres). There is a lower limit to theparticle size; particles smaller than 0.1 μm do not scatter strongly enough to enable the diffusion approximation, inherent in DWS, to be used. The samples were initially prepared in a stock solution with $\phi = 0.1$. Lower concentrations were prepared by diluting with water to the desired concentration. Higher concentrations were prepared by sedimentation, using gravity for the larger spheres or a centrifuge for the smaller spheres. Water was removed from the top of the sediment to attain the desired volume fraction, and the samples were remixed. In all cases the volume fraction was measured directly by weighing a portion of the sample before and after drying in a vacuum oven, maintained at room temperature. The weight fractions were converted to volume fractions by assuming that the particle density was equal to the density of bulk polystyrene.

A schematic of the experimental setup is shown in Fig. 3.4. The laser was an Ar^+ ion laser, operating at a wavelength of 0.5145 μm. A temperature controlled etalon in the laser cavity forced it to operate on a single longitudinal mode. This was essential because our detection system was sufficiently fast to be able to detect the beats between

neighboring modes, which occurred at 125 MHz for our laser cavity. Moreover, operating in a single mode ensures that the temporal correlation length of the light is larger that the longest diffusive light paths in the sample. If this is not done, the correlation function can be seriously degraded, and its shape changed from the predicted form,since the phase of the light traveling the longest paths is randomized by the loss of coherence rather than by the particle motion. The laser beam was focused onto one side of the sample, and the light was collected from the other side. The laser power incident on the sample was typically about 100 mW, and was adjusted for the different samples to attain sufficient count rates for each. The scattering cells were thin optical cuvettes, 1 cm wide. Thicknesses of 1, 2 or 5 mm were used, with the choice dictated by ensuring that $L/l^* > 20$ so that the diffusion approximation could be safely applied, and so that boundary effects were minimized [25]. The samples were immersed in a water bath which allowed the temperature to be maintained constant to within less than 0.1 K over the course of the measurements. This is essential to ensure that the viscosity does not vary over the course of the data collection. Immersion in the water bath also reduces the effects of internal reflections at the interface. Data for the larger spheres were all collected at room temperature; data for the smaller spheres were collected at an elevated temperature of about 40°C. This decreased the viscosity of the water, thereby increasing the characteristic hydrodynamic time scale, $\tau_0 = \rho a^2/\eta_0$, and allowing us to make measurements at shorter relative time scales.

To study the very fast time scales of interest, we used across-correlation technique[26]. The signal was divided into two equal portions, each of which was detected with a photomultiplier tube (PMT). The outputs of the two PMT's were cross-correlated. This method reduces the deleterious effects of afterpulsing in the individual PMT's. Afterpulsing is caused by the generation of secondary pulses induced either by ionization of atoms inside the tube, or by emission of photons due to electron absorption on a dynode or on the anode. The occurrence of afterpulsing introduces a spurious

correlation at short times when the signal from a single PMT is autocorrelated; this is greatly reduced by cross-correlating the signals from two PMT's. The cross-correlation technique also reduces the effects of dead-time in the PMT's and the electronics, since only the rising edge of each pulse triggers the counter in either channel. Provided that the count rate in each tube isnot too large, this allows measurements to be made at significantly faster time scales than would be possible with a single PMT.

Our detection optics used either multi-mode or single mode optical fibers [27]. In both cases, the beam splitter was integrated into the fibers, greatly simplifying the alignment. The multimode fiber had acore diameter of 100 μm, and standard, two-pinhole optics were used to collect the light. The fiber aperture itself acted as one of the pinholes, and a lens imaged the fiber face onto the collection side ofthe sample. Thus, the fiber diameter determined the area over which the light was collected. A second aperture at the lens was adjusted to limit the range of scattering vectors collected by the fiber, thereby increasing the size of the speckle spot so that it matched the size of the fiber core; this ensured a relatively large value for the intercept, β, of the measured intensity correlation function. In some experiments, we used a single mode fiber, instead of the multi-mode fiber; in this case the light was collected by a graded index (GRIN) lens with a 0.25 pitch. The single mode fiber collects only the light incident on the face of the GRIN lens which is in a single spatial mode. This results in an even larger intercept, β, while maintaining a high efficiency for light collection. Moreover, a single mode fiber receiver offers the possibility of working with an arbitrarily large scattering volume and with an arbitrary working distance.

The correlation functions were calculated using a correlator capable of measuring delay times as short as 12.5 nsec. At longer times, the channels were spaced in an increasing geometric progression with delay time. This provided sufficient accuracy to measure the decay of the correlation function down to levels of about 10^{-4}. The very short delay times of the early channels made obtaining data with good statistical accuracy

quite challenging. This problem was exacerbated by the need to maintain the count rate at a relatively low level to avoid dead-time problems in the cross-correlation technique. As a result, we typically collected data for about 12 hours to obtain sufficiently good statistics at the shortest times. The correlation functions were collected in successive 10 minute intervals, and the results were averaged. The samples were mounted on a motorized wheel, and the larger spheres were rotated and shaken every 10 minutes to minimize the effectsof sedimentation.

3.5. Experimental results

In a DWS experiment, as in all dynamic light scattering experiments,we measure time correlations in the intensity of the scattered light $\langle I(t)I(0)\rangle$. Since the average intensity is non zero, $\langle I(t)I(0)\rangle$ does not decay to zero at long times, but to the square of the average value of the intensity, $\langle I\rangle^2$; thus we normalize the data to its long time limit and obtain a normalized intensity autocorrelation function,

$$g_2(t)=\frac{\langle I(0)I(t)\rangle}{\langle I\rangle^2} \tag{3.40}$$

Since the fluctuations in electric field are Gaussian, the fluctuations in intensity can be replaced by the square of the fluctuations in electric field (the Siegert relationship), allowing us to express $g_2(t)$ in terms of the normalized field autocorrelation function $g_1(t)$ (Eq. 3.35)

$$g_2(t)=1+\beta|g_1(t)|^2 \tag{3.41}$$

β is the coherence factor which determines the intercept of the data at zero delay time. The value of β depends on the optical arrangement used in the experiment and reflects the number of coherence areas detected; as the number increases, the modulation of the intensity, and thus β, decreases. For polarized scattering detected with a single mode optical fiber, $\beta\approx 1$; for the typical two pinhole receiver, β is somewhat less than 1. However, multiply scattered light is completely depolarized, and there is no correlation

between the intensities of the two polarizations in a single speckle; thus the value of β is reduced by a factor of 2, so that $\beta \approx 0.5$.

A typical set of data, collected for about 12 hours from asample of 1.53-μm-diameter spheres at a volume fraction of $\phi = 0.20$, is shown in Fig 3.5; we plot $g_2(t)-1$ versus time. The signal-to-noise ratio of the data is good enough that over two and a half decades of decay in the correlation function are observed. At longer times there is an additional correlation observed in the data, due to fluctuations in the laser intensity. Independent measurements of this correlation function were made, allowing the contributions of the laser fluctuations to be subtracted from the DWS data. This was done by fitting the contributions of the laser fluctuations to an exponential decay, and subtracting this from the data. The corrected correlation function is shown in Fig. 3.6; the subtraction procedure is sufficiently accurate that the corrected correlation function can be measured over more than four decades of decay.

The inset displays the data over the first 0.5 μsec in a linear plot. It confirms the absence of afterpulsing effects, even down to the very short time scales accessible with our fast correlator and cross-correlation scheme. It also illustrates the level of the random fluctuations, or noise, in the data at the shortest time scales. This represents the largest fluctuations in the data because the time scale is so short; at longer times, these fluctuations are substantially reduced. The measured intercept is ≈ 0.42, somewhat less than 0.5 as expected for the two pinhole, multimode optical fiber receiver used. The actual value of the intercept must be determined experimentally; for very short times (*i.e.* for small decays of the correlation function), the uncertainty in β is the limiting factor in the accuracy of the data. To determine the most reliable value of β, a smooth polynomial is fitted to the first few data points. The data are normalized by the fitted value of β and the electric-field correlation function, $g_1(t)$, is then obtained using Eq. 3.41. A zero crossing routine is used to invert the data, which are assumed to follow the equation for a point-source geometry, Eq. 3.38. From this inversion, we obtain t_D^* (Eq. 3.36). This is

multiplied by $[S(q)]$, which is calculated using the Percus-Yevick equation for the structure factor [28] and the Mie-theory scattering results forthe form factor (Fig. 3.3). The final result from this analysis is the DWS-averaged $[H(t)]$ defined in Eq. 3.34.

To set the absolute level of the $[H(t)]$ data, a knowledge of the transport mean-free path, l^*, is required. It can, in principle, be obtained by two independent methods: l^* can be calculated theoretically [29], using Mie scattering theory for the form factor, and correcting for the particle correlations using the Percus-Yevick structure factor; alternatively, it can be determined experimentally by a measurement of the static transmission through the sample [15]. The static transmission is proportional to l^*; by comparing the measured transmission with that through a reference sample of identical thickness, and in the same geometry, the value of l^* relative to the reference can be measured [30,31]. By using a sample of relatively low volume fraction, the value of l^* can be calculated with reasonable accuracy, allowing the unknown l^* at higher volume fractions to be determined. However, in practice, we find that either of these techniques can introduce experimental uncertainties ofthe order of 5% in the value of l^*, which translate into uncertainties of the order of 10% in the absolute magnitudes of $[H(t)]$ determined from the data. Thus, we instead determine the absolute level of the data by scaling its long-time asymptote to the expected value of $[H^\infty]$, which is calculated using the theoretical values for $H^\infty(q)$ [32]. This ensures that the data at the different volume fractions and particle sizes are normalized in a consistent fashion. The uncertainty in this method can be tested by comparing the resulting values of l^* with those obtained from independent static transmission measurements and from a Mie scattering calculation. This comparison is shown in Fig. 3.7 for three different particle sizes. In all cases, the values of l^* obtained by these different procedures are in good agreement with one another. The largest discrepancies between the two experimental measurements of l^* (scaling $[H(t)]$ to the theoretical long-time asymptote $[H^\infty]$ and static transmission data) are within about 5%, consistent with the experimental uncertainties in the measurements. The

discrepancies with the Mie scattering theory are somewhat larger, as much as 30% in the worst case. We conclude that this scaling procedure provides a consistent method for determining $[H(t)]$, without introducing further uncertainties resulting from additional experiments.

The measured $[H(t)]$ are shown in Fig. 3.8 for several different particle sizes, and for a series of different volume fractions. The values of $[H(t)]$ are normalized by D_0, the limiting value of the diffusion coefficient at low volume fractions. The data are plotted as a function of the normalized time scales, t/τ_0, where $\tau_0 = \rho a^2/\eta_0$ is the viscous relaxation time of the suspension at low volume fractions. We are able to probe much shorter reduced times using larger particles; for the smallest particles, we can collect data only at times greater than several τ_0, even though we have reduced the viscosity of the suspension by making the measurements at an elevated temperature. The dashed line in each figure represents the behavior expected for a single particle in the fluid [12]. It includes the effects of the hydrodynamic interactions between the particle and the fluid, and thus approaches the asymptotic value very slowly, reflecting the algebraic decay of the velocity correlation function. The data for the lowest volume fractions follow this curve for all the different particle sizes; however, for the smallest particles, it is necessary to go to extremely low volume fractions (0.5%) to obtain agreement with the single particle theory. At higher volume fractions, the data have lower asymptotic values, as expected; they also deviate from the single particle curve at successively shorter times as the volume fraction is increased. However, in all cases, the data approach their asymptotic values rather slowly. The most remarkable feature of the experimental data is that, for all volume fractions and for all sphere sizes, the measured $[H(t)]$ can be scaled onto a single master curve [8]. This curve is given by the time-dependent mean-square displacement of an isolated sphere, $H_0(t^*)$, which can be calculated analytically (Eqs. 3.3 and 3.4) [12]. The scaling of the experimental data is shown in Fig. 3.9 for the same set of particle sizes. For the largest size shown, a=0.77μm, the experimental data are not sensitive to the

interaction portion of $[H(t)]$, and thus reflect the time-dependent mean-square displacement, of individual particles. By contrast, the data for the smaller spheres are sensitive to the interaction contribution to $[H(t)]$, and thus the data can no longer be interpreted in terms of the mean-square displacement, but rather represent an average overtime-dependent collective diffusion coefficients at various wavevectors.

The scaling of the data for the smaller spheres was unexpected; the measured $[H(t)]$ reflects a sum of two contributions, one from the self correlations $H(t)$, and a second from the interparticle hydrodynamic interactions, $H_I(q,t)$. The data for large spheres measures the selfcorrelation $H(t)$ only, and this can be scaled to the master curve. There is no reason to expect the interaction contribution to have the same functional form as $H(t)$; in fact it has a quite different time dependence (see section 3.7B). Nevertheless, the sum of the two contributions does scale to the same master curve; however, the scaling times, $[\tau(\phi)]$, are different for the different particle sizes. The ϕ-dependences of these scaling times, normalized by $\tau_0 = a^2\rho/\eta_0$, are shown for all the different particle sizes in Fig. 3.10. The data for the largest spheres follow the inverse of the ϕ-dependent, high-frequency viscosity [9], $\eta_0/\eta(\phi)$, as shown by the solid curve in Fig. 3.10. However, for a given volume fraction, $[\tau(\phi)]$ decreases rapidly with decreasing particle size. Even at very low volume fractions $[\tau(\phi)]$ is still sensitive to particle size; only at volume fractions ϕ<0.5% is it independent of particle radius.

The fact that the small sphere data scale in the same way as the large sphere data suggests that the approximation of a single relaxation time is still valid, independent of particle size. In a single relaxation time approximation, $[\tau] = [H^\infty]\tau_0$. However, the scaling time, $[\tau]$, measured in the DWS experiments for small particles is much shorter than would have been expected from experimental measurements of the wavelength-dependent diffusion coefficient [33]. Moreover, for the smallest particles, the measured relaxation time, $[\tau(\phi)]$, is even smaller than the q=0 relaxation time, $H^\infty(0)\tau_0$, which is

the shortest time we would have expected to measure. We discuss this point in more detail in section 3.7D.

Since we have a simple analytic form for $[H(t)]$, we can both check and refineour data analysis by working backwards to the original experimental correlation function $g_2(t)$. Using the analytic form for $H_0(t^*)$ [12], and our values for the scaling time $[\tau]$, we calculate $g_1(t)$ directly from Eqs. 3.36 and 3.38. The correlation function $g_2(t)$, calculated using Eq. 3.41, can be compared with the original, and the intercept then adjusted to provide the best agreement with the data. We typically found that only small changes in β were required. An example of the quality of the fit to the original data is illustrated by the solid line shown in Fig. 3.6; clearly the agreement is excellent. We can also use this back calculation to check for the possibility of absorption. Although both water and polystyrene latex exhibit very weak absorption, the optical path lengths are sufficiently long that absorption can have some influence. The effects of absorption can be included in the back calculation of the correlation function, $g_2(t)$, by incorporating an absorption length [31]. However, we found that the data showed virtually no effects of absorption, and so the shapes of the correlation functions were not modified.

3.6. Simulation method

Numerical simulations have begun to make significant contributions to the study of particle suspensions, by incorporating accurate calculations of the low Reynolds number or creeping-flow hydrodynamic interactions between spheres [34,35]. Nevertheless, these methods are very expensive computationally, and cannot easily be applied to large systems. Moreover, extensions of these methods to time-dependent hydrodynamic interactions would be even more time consuming; it would be necessary to calculate the hydrodynamic interactions at many different frequencies and then take an inverse Laplace transform. Theoretical results for time-dependent hydrodynamic interactions are only

available for dilute suspensions [36]. However, numerical algorithms based on discrete-velocity (lattice) gases [11,37] simulate the time-dependent Navier-Stokes equations directly, including thermal fluctuations; these techniques can therefore probe the temporal and spatial evolution of hydrodynamic interactions in complete detail. In this paper we use lattice-Boltzmann simulations [6,7] to help interpret the DWS results. It may well be that an improved understanding of these time-dependent interactions will lead to new and more efficient methods for computing time-independent (creeping-flow) hydrodynamic interactions.

The simulations used in this work are based on a combination of molecular dynamics, which is used to track the motion of the solid particles, and a fluctuating lattice-Boltzmann model of the fluid. The motivation behind the development of lattice-gas and lattice-Boltzmann models was the desire for a simplified molecular-like model of the fluid, which, although lacking some of the detailed mechanics of molecular dynamics, would still reproduce correct hydrodynamics at sufficiently large scales. It turns out that such models are remarkably effective at reproducing the hydrodynamic forces that occur in the dynamics of colloidal suspensions [7], although it has become apparent that the lattice-Boltzmann equation is, by and large, a better simulation tool for hydrodynamics than lattice gases. However, in its normalstate the lattice-Boltzmann equation cannot model the molecular fluctuations in the solvent that give rise to Brownian motion. Nevertheless, on length scales and time scales intermediate between the molecular and the hydrodynamic, thermally-induced fluctuations can be reduced to random fluctuations in the fluxes of the conserved variables [38]. In the present context, this means that the time evolution of the lattice-Boltzmann velocity distribution includes a stochastic term representing the thermally-induced fluctuations in the stress tensor [11]. These random stress fluctuations are uncorrelated in space andtime and are sampled from a Gaussian distribution; the variance of the fluctuations serves to define the effective temperature of the fluid [38]. Numerical tests show that the resulting particle motions, in dilute to

concentrated suspensions, closely match experimental results[9,10], even at very short times where particle inertia plays an important role. Since, a detailed account of the algorithm has already been published [6], together with extensive numerical tests [7], this discussion will not be repeated here. Instead we will describe specific details of the calculation of time and space dependent hydrodynamic interactions.

Diffusing-wave spectroscopy probes times that are very short compared with the time it takes a particle to diffuse a hydrodynamically significant distance; typical particle displacements are around 10^{-3} of the particle radius. We can most easily reproduce this situation on the computer by constraining the particle coordinates to their initial values. Thus the particles sit at fixed positions and interact hydrodynamically via fluctuations in translational and rotational velocity; in this case the long-time limit of $H(q,t)$ is related to the short-time wavevector-dependent diffusion coefficient, $D(q)/D_0 = H^{\infty}(q)/S(q)$. However we cannot measure particle displacements directly, as is done experimentally, since the particle coordinates are fixed. Instead we calculate $H(q,t)$ indirectly, via its second derivative, the longitudinal velocity correlation function $J(q,t)$; from Eq. 3.10

$$J(q,t) = \frac{d^2}{dt^2}\left[D_0 t H(q,t)\right] = \left\langle \frac{1}{N}\sum_{i,j=1}^{N}\left[\hat{\mathbf{q}}\cdot\mathbf{U}(t)\mathbf{U}(0)\cdot\hat{\mathbf{q}}\right]e^{i\mathbf{q}\cdot\mathbf{R}_{ij}}\right\rangle \tag{3.42}$$

The initial value of the correlation function $J(q,0) = k_B T/M$, where M is the particle mass.

We calculate $J(q,t)$ from the particle coordinates and velocities, by averaging over 10^4 time steps, or about 500 times the typical relaxation time of the correlation functions. In addition, the simulations were run for 10^3 steps before any data was collected, to allow time for the hydrodynamic interactions to develop and for the particle velocities to come to thermal equilibrium. Since the particle configuration does not change during the course ofthe simulation, it is necessary to average over an ensemble of initial conditions, which were generated from a hard-sphere Monte-Carlo program. Thus in addition to the time

averaging, we also ensemble averaged each set of results over 10 statistically independent configurations. The statistical errors in $H(q,t)$ are of the order of 10% at long times and significantly less at shorter times; this is adequate for the present purposes. It would have been desirable to use a more extensive ensemble averaging, say 100 configurations, but the computational demands would have been excessive. Simulations were run at volume fractions of about 5% (dilute), 25% (semi-dilute), and 45% (concentrated). The effects of varying particle size, particle mass, number of particles and fluid viscosity have all been studied. A compilation of the parameters characterizing each run is reported in Table I. It should be noted that the variations in particle size reported in the simulations do not correspond to different physical systems; the different particle sizes affect only the numerical accuracy of the results [7].

For a direct comparison with experiment, we have simulated the DWS average $[H(t)]$ (Eq. 3.34) using the Mie scattering form factor $F(q,a)$ (see Fig. 3.3) appropriate to each particle size. In the simulated DWS average, the particle size enters only through the choice of form factor; it has nothing to do with the particle radius reported in Table I. The q^3 factor in Eq. 3.34 weights the average towards the high-q components of $H(q,t)$. Thus for sufficiently large particles, that is for particles with a radius greater than about 1 μm, DWS probes only the motion of individual particles (the high-q limit of $H(q,t)$). For smaller particles, the DWS average includes some of the collective motions as well.

A drawback of the current computer code is that it cannot simulate neutrally buoyant particles, but only rather massive ones ($\rho_R > 4$). This makes a comparison with the DWS data rather indirect, as we must scale both sets of data to different $H_0(t^*)$ functions, appropriate to the different mass ratios, rather than compare the data directly. On the other hand, this difficulty has allowed us to probe somewhat different physical systems and perhaps learn something new about hydrodynamic interactions (see section 3.7D). The technical reason for the limitations on particle mass is that the velocities are updated explicitly,with information at one time step being used to calculate the velocities at the

next time step. Such numerical schemes can be unstable if insufficiently damped; in the present context this leads to a stability criterion which sets a lower bound to the particle mass [7]. This problem can be corrected by using a more complicated implicit update of the particle velocities, which uses information from both old and new velocities; this is planned in future work.

3.7. Simulation results

Our simulations of the long-time hydrodynamic interactions, $H_N^\infty(q)$, show a significant dependence on system size,or number of particles, N. The deviations of $H_N^\infty(q)$ from the large system limit ($H_N^\infty(q)$) arise from the spatially-correlated flow fields of the periodic images; they are of order a/L or $(\phi/N)^{1/3}$. In previous work [39], it has been shown that a correction for the system size dependence of in the q=0 and $q \to \infty$ limits can be calculated analytically. In the Appendix, these results are generalized to arbitrary q; the final result for a system of N spheres is

$$H^\infty(q;\phi) = H_N^\infty(q;\phi) + 1.76S(q;\phi)\frac{\eta_0}{\eta(\phi)}\left(\frac{\phi}{N}\right)^{1/3} \tag{3.43}$$

where H_N^∞ is the simulation measurement. These corrections lead to consistent estimates of $H^\infty(q)$ over the a range of system sizes from N=16 spheres to N=1024 spheres and over the whole range of volume fractions, from dilute to concentrated. We have used Eq. 3.43 to correct all our simulation data for $H^\infty(q)$; the results are shown in Fig. 3.11. Dynamically, the data for finite systems $H_N(q,t)$ begin to deviate from the large-system limit at times of the order L^2/ν; beyond this time, vorticity generated by the periodic images interferes with the flow in the unit cell of interest and $H(q,t)$ asymptotes rapidly to $H_N(q)$. Thus the accessible time range over which reliable simulation data for $H(q,t)$ can be obtained is proportional to $N^{2/3}$. We have found empirically that systems of 128 spheres are sufficiently large to enable $H(q,t)$ to be calculated out to times of order

$100\tau(\phi)$ which is the range of experimental interest; thus most of our simulations are for 128 spheres.

A. Wavelength-dependent diffusion coefficients

The long-time asymptote of $H(q,t)$ can be obtained from a single integral of the longitudinal velocity correlation function (Eq. 3.42),

$$H^{\infty}(q) = \lim_{t\to\infty} H(q,t) = \lim_{t\to\infty} \frac{d}{dt}[tH(q,t)] = D_0^{-1}\int_0^{\infty} J(t)dt \qquad (3.44)$$

this integral asymptotes to H^{∞} much more rapidly than $H(q,t)$ itself. In Fig. 3.11 we show simulations of $H^{\infty}(q)$ and $D_0/D(q) = S(q)/H^{\infty}(q)$, for comparison with theory and experiment; the data has been corrected for finite-size effects as described in Eq. 3.43. The different symbols correspond to solid particles of different size and mass, and to systems with different numbers of particles. The parameters characterizing each simulation are describedin Table I. Within the statistical uncertainties, the corrected data for $H^{\infty}(q)$ are independent of number of particles, particle size and particle mass. The results are in quite good agreement with Beenakker and Mazur's theoretical calculation [32]. However there are some discrepancies at intermediate concentrations ($\phi = 0.25$) which is also the region with the largest errors in the theoretical calculations of the limiting cases of low q ($H^{\infty}(0)$) and high q (H^{∞}). The simulation results are in better agreement with the known results [39]; the theoretical calculations are too small by 10-20%. At high concentrations, both simulations and theory deviate from the correct results at high q [39] by 10-20%; simulations with larger particles are necessary to completely capture the short-range hydrodynamic interactions at high concentrations. Results for $D_0/D(q) = S(q)/H^{\infty}(q)$ are also shown in Fig. 3.11, for comparison with experiment [33]. Again the agreement is quite good, but a detailed comparison is hindered by obvious uncertainties in both the simulation and the experimental data. However the general

behavior is similar; the peaks and troughs in $D_0/D(q)$ appear at the same values of qa and have quite similar magnitudes. The experiments would predict a higher first peak in $H^{\infty}(q)$ at $\phi = 0.45$, but this discrepancy is probably due mostly to the coarse sampling of qa in the simulations.

B. The interaction contribution $H_I(q,t)$

In Fig. 3.12 we show a small sample of our simulation results, for two characteristic wavevectors; $qa \approx 1.8$, a relatively long wavelength (Fig. 3.12a), and $qa \approx 3.6$, near the first peak of the structure factor (Fig. 3.12b). The q-dependence of the correlation functions is similar at all volume fractions, but more pronounced at higher concentrations; we show results at a volume fraction $\phi = 45\%$ to indicate the maximum variation with q. The scaled single-particle contribution, $H(t/\tau(\phi))/H^{\infty}(\phi)$, is indistinguishable from the theoretical curve for one sphere, shown in Fig. 3.12 by the solid line.

By contrast, under these same scaling conditions, $H_I(q,t)$ exhibits very different behavior that is strongly dependent on q. For small q ($qa < 2$) the interaction contributions are negative. At first sight this might be a little surprising; because of hydrodynamic interactions, the motion of one sphere tends to cause its neighboring spheres to move in the same direction. However, for sufficiently large volumes (*i.e.* for sufficiently small q), the average flow across any plane in the system must vanish. Thus, the motion of a particle induces a backflow of displaced fluid, which in turn sweeps the other particles along with it; this motion of particles and fluid opposes the motion of the primary sphere. Therefore, on sufficiently large length scales, there is an overall anti-correlation of particle velocities. By contrast, the wavevectors $qa \approx \pi$ probe primarily the first shell of neighbors; for such closely spaced particles the direct hydrodynamic interactions dominate the much weaker backflow effect, so that these contributions are

positive. Finally, for very large q, there is no phase correlation between different spheres, and the interaction contribution vanishes.

C. Scaling of $H(q,t)$

The most remarkable result shown in Fig. 3.12 is that, although the interaction contributions (circles) do not scale to the single-sphere curve, the sum of the self-contribution and the interaction contribution at a particular wavevector (squares) *does* scale to the single-sphere curve, but with a different normalization-$H^{\infty}(q)$ rather than H^{∞}-and a different relaxation time $\tau(q)$. This is a general result, independent of q and independent of ϕ. An additional set of $H(q,t)$ data ($\phi = 0.25$, $N = 1024$) is shown in Fig. 3.13, to illustrate the scaling over the whole range of wavevectors. The wavevectors are proportional to the number of wavelengths, n, within the periodic unit cell $q = 2\pi n/L$ (the length of the unit cell $L = (4\pi N/3\phi)^{1/3}a$); in this case (#3) qa = 0.24n (Table I). Results for a system of 128 spheres are essentially identical for even values of n where the wavevectors are coincident. Simulations at other volume fractions show similar behavior and are not shown. Once again we see that the $H(q,t)$ data scale very well to the single-sphere master curve. There are deviations from scaling at small q ($n \leq 2$), but these are artifacts, which arise because the simulated systems are much more compressible than the experimental ones. As a result, the time scale for sound propagation, a/c_s (c_s is the speed of sound) is not negligible compared with the viscous time scales, $\rho a^2/\eta_0$; with the parameters chosen for these simulations, the dimensionless quantity $\rho c_s a^2/\eta_0$ is of order 10, whereas experimentally it is of order 1000. The simulated velocity correlation functions show a pronounced oscillation at low q, due to the effects of sound waves; the period of the oscillation is proportional to q (Fig 3.14a). These oscillations in the velocity correlations cause the deviations from scaling in $H(q,t)$ observed in Fig. 3.13. To confirm that these deviations are a compressibility effect, we have run a calculation with a much

smaller viscosity, so that the ratio $\rho c_s a^2/\eta_0$ is now about 200. The velocity correlation function for this system is monotonically decaying at all q; an example is shown in Fig. 14b. Thus fortruly incompressible systems, we expect to see scaling of $H(q,t)$ over the whole range of length scales. It is also worth noting that these low-q correlation functions make next to no contribution to the DWS averages, since their weighting is very small.

The scaling of $H(q,t)$, observed in the simulations, implies that time-dependent hydrodynamic interactions can be characterized by a single time scale at each value of q, suggesting that the suspension is behaving as an effective medium at all length scales, and at all time scales. The relaxation times required to scale the simulation data to the single-sphere master curve are shown in Fig. 3.15. The relaxation time scale is quite short at low q; it peaks around $qa = \pi$, and then, at large q, reaches the asymptotic value expected for theself-diffusion coefficient. The q-dependence of the relaxation times is similar to the long-time asymptote $H^{\infty}(q)$ (Fig. 3.11), although there are noticeable deviations at small values of q ($qa < 1$); overall, this is reasonably consistent with a single relaxation time for $H(q,t)$.

We emphasize that this observed scaling is not a trivial result. Although $H(q,t)$ has very little structure, the overall fit is still sensitive to variations in system parameters. For instance, if one should attempt to scale $H(q,t)$ data to the single-sphere function for a particle with the incorrect mass density, no manner of adjustment of the relaxation time will produce a good fit. Although we do not claim that this scaling is necessarily exact over the whole time range, nevertheless, within the accuracy of both simulations and experiment we cannot detect any significant deviations from scaling.

The most important question is why should the data at various q scale onto the single-particle curve. We do not, as yet, have a complete explanation for these observations. At asymptotically long times the velocity correlation functions $\langle U_i(t)U_j(0)\rangle$ are known to decay with an algebraic $t^{-3/2}$ dependence, regardless of the separation between the

spheres [40]. Thus any spatially-weighted average of these correlation functions will also decay as $t^{-3/2}$ with some effective relaxation time [41]. However, the most interesting observation is that the correlation functions apparently see the same single-time-scale relaxation mechanism, regardless of spatial scale and concentration, modulated only by an effective viscosity $\eta(q,\phi)$; the origin of this is not understood.

D. Scaling of $[H(t)]$

We have already observed that both the simulation data for $H(q,t)$ and the experimental data for $[H(t)]$ can be scaled to the single-sphere curve $H_0(t^*)$. This scaling is strikingly similar to our earlier observations for single-particle motion [9,11]. However, the effects of the collective hydrodynamic interactions are very evident in the behavior of the time scale, both in the experiments (Fig. 3.10) and in the simulations (Fig. 3.15). At a given volume fraction ϕ, the experimentally measured ratio $[\tau]/\tau_0$ decreases rapidly with decreasing particle size. At first sight, the monotonic decrease of the measured $[\tau]$ seems inconsistent with the variation in $\tau(q)$ shown in Fig. 3.15. To investigate the origin of this apparent discrepancy, we used the q-dependent simulation resultsto calculate the DWS-weighted average value, $[H(t)]$. We used the expected DWS weighting factors shown in Fig. 3.3[5]. The behavior of the DWS-weighted simulation data is quite consistent with experimental observations; as shown in Fig. 3.16, the results for different particle sizes and different concentrations can again be scaled to the single-particle curve. The relaxation times, shown in Fig. 3.17, decrease monotonically with decreasing particle radius, as well as with concentration. Thus the pronounced variationsin relaxation time with wavevector, observed in the simulations (Fig. 3.15), are washed out by the averaging over wavevector sinherent in the DWS experiment. The simulated DWS averages are insensitive to the details of the averaging process, and to the exact form of the weighting function; even

using the asymptotic Rayleigh-Gans form factor instead of the Mie expression makes little difference to the result.

Although both the experimental and simulated $[H(t)]$ data scaleto $H_0(t^*)$, the experimentally measured relaxation times (Fig. 3.10) for the smaller particles are much shorter (by about a factor of two) than predicted by the simulations (Fig. 3.17). We can make an independent estimate of the expected DWS relaxation times, based on the ratio of the integral of the longitudinal velocity correlation function ($H^{\infty}(q)$) to its initial value k_BT/M; if there is a single dominant relaxation process, this equivalence is exact. We can take experimental data for wavevector-dependent diffusion coefficient, $D(q) = H^{\infty}(q)/S(q)$ [33], and use it to estimate the DWS-averaged relaxation times. The resulting estimates of $[\tau]$ are close to the simulation results shownin Fig. 13.7 but quite different from the DWS-measured relaxation times. Moreover, for the smallest (0.1 μm) particles, the measured $[\tau]$ is even shorter than the q=0 relaxation time, $H^{\infty}(0)\tau_0$, which is the shortest time one would have expected to observe. These considerations strongly suggest that there is an additional relaxation process in the DWS experiments that is absent from the simulations. We believe that the excitation of collective motions of the particles by the scattering of sound waves may provide the extra relaxation mechanism. A quantitative theory for hydrodynamic interactions in a compressible fluid (*i.e.* including the propagation, scattering, and damping of sound waves) has not been developed as yet; even the theory for asingle sphereis quite complex [42]. In the absence of a proper theory we suggest a mechanism, which seems to us to be physically reasonable,and which can account for the very short relaxation times observed in the experimental data for small particles.

When a sphere undergoes a fluctuation in its velocity, an impulse of momentum is transferred to the fluid. Part of this momentum impulse diffuses by viscous flow and givesrise to the hydrodynamic correlations which require some time totake effect (of the order τ_0; see Fig. 3.12). However, additional momentum is carried off by sound waves,

which causes a rapid decay of the particle velocity at very short times (of the order a/c_s). Thus, in a very dilute suspension, the velocity of a neutrally buoyant particle decays almost instantaneously from a root-mean-square value of $\sqrt{k_B T/M}$ to a smaller value of $\sqrt{2k_B T/3M}$. This rapidly decaying portion of the velocity correlation function makes no contribution to the mean-square displacement, and simply rescales the initial value (see section 3.2). In more concentrated suspensions the sound waves are scattered by neighboring particles, inducing collective motions at very short times; we have observed this effect visually in some two-dimensional computer simulations. Thus the velocities of *different* spheres can be correlated by sound propagation even at very short times, $t \approx a/c_s \ll \tau_0$ The effect of the scattered sound waves on the test sphere would be negligible, as only a tiny fraction of the initial momentum would be scattered back to the originall location. Thus we would not expect the sound waves to significantly alter the shape of the self-correlation function, $H(t)$ (which dominates the large particle data), but only the collective , $H_1(q,t)$, probed by the smaller particles.

The sound waves should perturb the collective particle motions until they are damped out by viscous dissipation, roughly on a time scale $\tau_0 = \rho a^2/\eta_0$. Thus the scattering of sound waves from particle to particle would produce additional contributions to $H(q,t)$ at small q and at short times.At longer times, the sound waves would be damped out; eventually we expect the mean-square displacement to track the incompressible fluid result. The overall effect of the sound waves would then be to increase the measured values of $[H(t)]$ for small particles andat short times. Because the experimental measurements of $[H(t)]$ for small particles are so flat (see Fig. 3.8), and because the absolute amplitudes are not well known, a relatively small change in the short-time behavior of $[H(t)]$ (*i.e.* for times less than τ_0) could have a large effect on the estimated relaxation time.

This picture satisfactorily accounts for the main qualitative features of our observations. The primary difference between the experimental and the simulated systems

is the mass density of the particles. In the DWS experiments they are nearly neutrally buoyant (minimizing sedimentation effects), whereas in the simulations the particles have a much larger mass density than the surrounding fluid. This provides a possible explanation for the discrepancy between the simulated relaxation times and the experimental measurements. The total momentum carried off by sound wavesis independent of particle mass; it depends only on the mass of the equivalent volume of fluid. Thus for particles with mass densities much larger than the surrounding fluid (as in the simulations) this effectis small and almost all the momentum transfer is by viscous flow. However, for neutrally buoyant particles (as in the experiments), the momentum in the sound waves is a significant fraction of the total (1/3) and there are instantaneous correlations in particle velocities which are essentially absent for the more massive spheres used in the simulations.

There is another possible source of the discrepancy in the simulated and measured relaxation times. As we noted earlier (see section 3.4), a small number of pairs of particles may lie within the range of the screened Coulomb potential. There are approximately $8\pi N^2 a^2 \lambda g_c / V$ such pairs, where λ is the screening length and g_c is the value of the pair distribution function at contact. These pairs of particles will repel each other electrostatically as long as they remain within the screening length; the interaction time t_λ is of order $\lambda\sqrt{m/k_B T}$, assuming the particle motion is ballistic in this time regime. Estimating the screening length as $\lambda = 50\,\text{Å}$, gives an interaction time $t_\lambda \approx 0.2\mu\text{s}$ for the 0.1μm spheres; this is in the appropriate time range to modify the measured $[H(t)]$ at short times. We can also estimate the magnitude of the possible correction to the mean-square displacement. A pair of particles within the screening length will exert a force on one another of order $k_B T/\lambda$; over the interaction time, this produces an additional displacement of order $(k_B T/2m\lambda)t_\lambda^2$. Multiplying this mean square displacement (λ^2) by the estimated number of interacting pairs, we can estimate that the correction to $[H(t)]$ is of order $\lambda^3/aD_0 t_\lambda \approx \lambda^2 \eta/\sqrt{mk_B T}$. This factor is of order unity for the smallest particles.

For the larger particles, the effectis much less pronounced. The magnitude of the correction scales as $a^{-3/2}$ and the time scale over which it operates is proportional to $a^{3/2}$. Thus changes in the shape of $[H(t)]$ due to electrostatic interactions scale as a^{-3}.

3.8. Conclusions

In this work we have shown that the scaling relations first observed for the self-diffusion coefficient [9,11] apply to collective diffusion as well. Computer simulations show that the wavevector-dependent diffusion coefficient has the same functional dependence ontime for all wavevectors and at all solids volume fractions. These results suggest that monodisperse suspensions behave hydrodynamically as continuous media, over a substantial range of space and time scales, with only avarying effective viscosity. The characteristic time that scales the simulation data for the diffusion coefficient has a qualitatively similar dependence on wavevector to the structure factor of the suspension. The validity of the computer simulations was examined by a detailed comparison with diffusing wave spectroscopy experiments, which are sensitive to particle motions at the very small length scales and time scales required to observe the temporal evolution of the hydrodynamic interactions. The effective diffusion coefficient probed by the light scattering reflects an average over many wavevectors; however, by using particles of different sizes, the contributions from smaller wavevectors can be measured. Again the time-dependent data are found to scale to the same single-sphere functional form, with the characteristic scaling time decreasing with decreasing particle size, reflecting the larger contribution from the smaller wavevectors. A detailed comparison of wavevector-averaged simulation data, weighted to match the light scattering, exhibits the same qualitative trends as the experiment; however, differences in relaxation time persist. We believe that these differences suggest that sound wave propagation may play an important role in the development of hydrodynamic interactions.

Acknowledgments

All the computer simulations reported in this chapter were performed by Tony Ladd. We thank Patrick Warren, Pep Espanol, Rudy Klein, Scott Milner, Dave Pine and Paul Chaikin for useful discussions. This work was partially supported by NASA and by the U.S. Department of Energy and Lawrence Livermore National Laboratory under Contract No. W-7405-Eng-48.

*

*The work reported in this chapter will appear in *Physical Review* E., Anthony J.C. Ladd, Hu Gang, J.X. Zhu, and D.A. Weitz, "Temporal and Spatial Dependence of Hydrodynamic Correlation: Simulation and Experiment". A short version has been published in *Physical Review Letters*, Anthony J.C. Ladd, Hu Gang, J.X. Zhu, and D.A. Weitz, "Time-Dependent Collective Diffusion of Colloidal Particles" **74** 318(1995).

REFERENCES

[1] R.B. Jones and P.N. Pusey, Annu. Rev. Phys. Chem. **42**, 137 (1991).

[2] D.J. Pine, D.A. Weitz, P.M. Chaikin, and E. Herbolzheimer, Phys. Rev. Lett. **60**, 1134 (1988).

[3] D.A. Weitz, D.J. Pine, P.N. Pusey, and R.~J.~A. Tough, Phys. Rev. Lett. **63**, 1747 (1989).

[4] S. Fraden and G. Maret, Phys. Rev. Lett. **65**, 512 (1990).

[5] D.A. Weitz *et al.*, Physica Scripta **T49**, 610 (1993).

[6] A.J.C. Ladd, J. Fluid Mech. **271**, 285 (1994).

[7] A.J.C. Ladd, J. Fluid Mech. **271**, 311 (1994).

[8] A.J.C. Ladd, H. Gang, J.X. Zhu and D.A. Weitz, Phys. Rev. Lett. **74**, 318 (1995).

[9] J.X. Zhu *et al.*, Phys. Rev. Lett. **68**, 2559 (1992).

[10] M.H. Kao, A.G. Yodh, and D.J. Pine, Phys. Rev. Lett. **70**, 242 (1993).

[11] A.J.C. Ladd, Phys. Rev. Lett. **70**, 1339 (1993).

[12] E.J. Hinch, J. Fluid Mech. **72**, 499 (1975).

[13] I. Zúñiga and P. Español, Phys. Rev. Lett. **71**, 3665 (1993).

[14] D.A. Weitz and D.J. Pine, in *Dynamic Light Scattering. The Method and Some Applications*, edited by W. Brown (Clarendon Press, Oxford, 1993).

[15] J.Z. Xue, X.L. Wu, D.J. Pine, and P.M. Chaikin, Phys. Rev. **A45**, 989 (1992).

[16] J.X. Zhu, D.A. Weitz, and R. Klein, in *Photonic Band Gaps and Localization*, edited by C. Soukoulis (Plenum, New York, 1993).

[17] F.C. MacKintosh and S. John, Phys. Rev. B **40**, 2383 (1989).

[18] B.J. Berne and R. Pecora, *Dynamic Light Scattering with Applications to Chemistry, Biology and Physics* (Wiley, New York, 1976).

[19] P.N. Pusey and R.J.A. Tough, in *Dynamic Light Scattering: Applications of Photon*

Correlation Spectroscopy, edited by R. Pecora (Plenum, New York, 1985).

[20] G. Maret and P.E. Wolf, Z. Phys. **B65**, 409 (1987).

[21] P.G. deGennes, *Scaling Concepts in Polymer Physics* (Cornell University Press, Ithaca, 1979).

[22] X. Qiu *et al.*, Phys. Rev. Lett. **65**, 516 (1990).

[23] D.J. Pine, D.A. Weitz, J.X. Zhu, and E. Herbolzheimer, J. Phys. (Paris) **51**, 2101 (1990).

[24] M. Kerker, *The Scattering of Light* (Academic, New York, 1969).

[25] J.X. Zhu, D.J. Pine, and D.A. Weitz, Phys. Rev. **A44**, 3948 (1991).

[26] H.C. Burstyn and J.V. Sengers, Phys. Rev. **A27**, 1071 (1983).

[27] J. Ricka, Appl. Opt. **32**, 2860 (1993).

[28] W. Hess and R. Klein, Adv. Phys. **32**, 173 (1983).

[29] P.E. Wolf, G. Maret, E. Akkermans, and R. Maynard, J. Phys. (Paris) **49**, 63 (1988).

[30] A. Ishimaru, *Wave Propagation and Scattering in Random Media* (Academic, New York, 1978).

[31] D.J. Pine *et al.*, in *Scattering and Localization of Classical Waves in Random Media*, edited by P. Sheng (World Scientific, Singapore, 1990).

[32] C.W.J. Beenakker and P. Mazur, Physica **A126**, 349 (1984).

[33] W. van Megen, R.H. Ottewill, S.M. Owens, and P.N. Pusey, J. Chem. Phys. **82**, 508 (1985).

[34] J.F. Brady and G. Bossis, Ann. Rev. Fluid. Mech. **20**, 111 (1988).

[35] A.J.C. Ladd, J. Chem. Phys. **88**, 5051 (1988).

[36] H.J.H. Clercx and P.P. J.M. Schram, Physica **174A**, 325 (1991).

[37] A.J.C. Ladd, M.E. Colvin, and D. Frenkel, Phys. Rev. Lett. **60**, 975 (1988).

[38] L.D. Landau and E.M. Lifshitz, *Fluid Mechanics* (Addison-Wesley, London, 1959).

[39] A.J.C. Ladd, J. Chem. Phys. **93**, 3484 (1990).

[40] W. Van Saarloos and P. Mazur, Physica **A120**, 77 (1983).

[41] S.T. Milner and A.J. Liu, Phys. Rev. E **48**, 449 (1993).

[42] R. Zwanzig and M. Bixon, Phys. Rev. **A2**, 2005 (1970).

[43] J. Happel and H. Brenner, *Low-Reynolds Number Hydrodynamics* (Martinus Nijhoff, Dordrecht, 1986).

[44] H. Hasimoto, J. Fluid Mech. **5**, 317 (1959).

[45] C.W.J. Beenakker and P. Mazur, Physica **A120**, 388 (1983).

[46] T. Dodd, A.S. Sangani, D.A. Hammer, and D.L. Koch, J. Fluid Mech. (1995), in press.

TABLES

TABLE I. Specification of the system parameters used in the computer simulations; the labels in Figs. 11 and 15 correspond to the entries below.

	ϕ	N	a	ρ_R
#1	0.050	128	1.54	8.7
#2	0.243	128	2.61	10.0
#3	0.243	1024	2.61	10.0
#4	0.255	128	4.53	5.0
#5	0.451	128	4.53	11.0
#6	0.451	16	4.53	11.0
#7	0.451	128	4.53	5.0

APPENDIX; FINITE SIZES EFFECTS

At long times, the hydrodynamic interactions between spatially fixed (or very slowly moving) particles can be computed from the quasi-staticor "creeping-flow" fluid equations[43]. The velocities of the spheres $\mathbf{U}_i$ are linearly related to the forces $\mathbf{F}_j$,

$$\mathbf{U} = \sum_{j=1}^{N} \mu_{ij} \mathbf{F}_j ; \tag{A1}$$

the mobilities μ_{ij} are dependent on the configuration of all N spheres in the system. For a single sphere $\mu_0 = (6\pi\eta_0 a)^{-1}$. The hydrodynamic interaction function $H^{\infty}(q)$ is given by an ensemble average of μ_{ij} [32]

$$\mu_0 H^{\infty}(q) = \left\langle \frac{1}{N} \sum_{i,j=1}^{N} \hat{\mathbf{q}} \cdot \mu_{ij} \cdot \hat{\mathbf{q}} \right\rangle. \tag{A2}$$

It describes the average response of the system $\langle U(q) \rangle$,

$$\langle U(q) \rangle = \left\langle \frac{1}{N} \sum_{i=1}^{N} \hat{\mathbf{q}} \cdot \mathbf{U}_i e^{i\mathbf{q}\cdot\mathbf{R}_{ij}} \right\rangle, \tag{A3}$$

to a spatially periodic external force $F(q)$,

$$\mathbf{F}_j = \hat{\mathbf{q}} F(q) e^{-i\mathbf{q}\cdot\mathbf{R}_j} ; \tag{A4}$$

from Eqs. A1 through A4

$$\langle U(q) \rangle = \mu_0 H^{\infty}(q) F(q). \tag{A5}$$

For a very dilute suspension, $H^{\infty}(q) \to 1$ at all q. However, for a periodic system, $H_N(q)$ differs from 1 by terms proportional to a/L (L is the length of the unit cell). The coefficient can be calculated by summing the flow fields from an infinite cubic array of spheres [44]; the correction to $H_N^{\infty}(q)$ is given by [39]

$$H(q) = H_N^{\infty}(q) + 1.76(\phi/N)^{1/3} + O(\phi/N) \tag{A6}$$

Except for very small systems, terms of order ϕ/N can be ignored.

At higher volume fractions, the hydrodynamic interactions between a sphere and its periodic images are screened by the other particles in the suspension. Since these interactions are at distances of order $L \gg a$, the screening can be accounted for by an effective medium, with viscosity $\eta(\phi)$ [45]. Thus if a force is applied to a particular sphere in a periodic system, that sphere experiences the flow field from all its periodic images, but modulated by the suspension viscosity, $\eta(\phi)$, rather than the pure fluid viscosity, η_0. This gives acorrection to the high-q (single-particle) limit [39],

$$H^{\infty} = H_N^{\infty} + 1.76\frac{\eta_0}{\eta(\phi)}(\phi/N)^{1/3} \tag{A7}$$

It has been shown that this correction accounts for the system size dependence of the short-time self-diffusion coefficient, $D_s(\phi) = H^{\infty}D_0$ essentially exactly [39].

At longer wavelengths a particular test sphere sees not only the flow field from its periodic images, but also the flow field from images of neighboring spheres. We can approximate this flow field as an average flow field located at the image of the test sphere (sphere 1) but with an effective force

$$F_{eff} = \left\langle \sum_{j=1}^{N} \hat{\mathbf{q}}F(q)e^{i\mathbf{q}(\mathbf{R}_i - \mathbf{R}_j)} \right\rangle = \hat{\mathbf{q}}F(q)S(q); \tag{A8}$$

$S(q)$ is the structure factor defined in Eq. 3.15. Thus our correction for $H^{\infty}(q)$, valid at all wavevectors and volume fractions, is

$$H^{\infty}(q) = H_N^{\infty}(q) + 1.76S(q,\phi)\frac{\eta_0}{\eta(\phi)}(\phi/N)^{1/3} \tag{A9}$$

as given in Eq. 3.43. Similar arguments have been used toderive corrections for the collective mobilities ($\mu_0 H^{\infty}(0)$) of spheres [39] and disks [46].

CHAPTER IV

THE PRINCIPLES OF PURIFICATION FOR MONODISPERSE EMULSIONS

Emulsions are a special kind of colloidal dispersion, comprised of one liquid dispersed in a second liquid[1,2]. The two liquids are immiscible; usually one of the liquids is aqueous, and the other is oil. For example emulsions can be oil dispersed in water, or water dispersed in oil. Emulsions of any significant stability contain oil, water, and at least one emulsifying agent, usually called a surfactant[3]. Their structure can be described as spherical droplets coated with surfactant molecules and dispersed in the continuous phase (solvent). The surfactant molecules consist of two well-defined regions: one of which is oil soluble (lipophilic, or hydrophobic) and the other of which is water soluble (hydrophilic). The hydrophobic part is non-polar and usually consists of aliphatic or aromatic hydrocarbon residues. The hydrophilic part consists of polar groups which can interact strongly with water. The most significant characteristic of this type of amphiphile is the tendency to adsorb very strongly at the interface between water and oil. The substances at the interface lower the interfacial tension. They therefore make the formation of new surface easier.

In order to produce an emulsion from two mutually insoluble liquids, it is usually necessary to put a considerable amount of mechanical energy into the system. The minimum energy required for the emulsification process is the extra surface free energy, $F = \Gamma \Delta A$, where Γ is the interfacial tension and ΔA is the increase in surface area when a large drop is broken into several smaller ones. The actual energy required is much larger because excess energy is needed to overcome the Laplace pressure gradient. Laplace pressure is the pressure difference between fluids separated by an interface, resulting from interfacial tension and the curvature of the interface, which is Γ/a, where a is the radius of the droplet. To break the droplet, the shear stress $\eta\dot{\gamma}$, where η is the viscosity of the

dispersion and $\dot{\gamma}$ is the exerted shear rate, must at least exceed the interfacial pressure Γ/a, which prevents the droplet from deforming. So we need either create high η or high $\dot{\gamma}$ to enhance the formation of emulsions. The presence of surfactants lowers the interfacial tension Γ, and hence reduces the energy requirements for emulsification. However, another important function of the surfactants is that they provide a physical barrier against coalescence once the droplets are formed. Therefore surfactants are an essential component in the formation of emulsions and are required to maintain the stability of the systems.

The emulsion's macroscopic properties are determined from the microscopic properties. It is important to understand emulsion properties at colloidal scales for understanding the properties on macroscopic scales. On microscopic scale, particle interactions and dynamic properties (such as translational and rotational diffusion) are sensitive to the size and the shape of emulsion droplets. Emulsion droplets with well defined shape and very narrow size distribution are of great importance in the studies of the dynamics and the stability of emulsions, because experimental results from particles with well defined sizes are more convincing in addressing questions that depend critically on the size of the droplets. In the classical method of emulsion preparation, oil, water and surfactant are mixed using a mixer like a colloid mill, yielding polydisperse emulsion droplets. Several years ago Bibette[5-7] developed a purification technique called fractionated crystallization, that enables the production of monodisperse emulsions. In the following we describe the method to make crude emulsions and the principles of the purification technique to produce monodisperse emulsions.

The method used to make crude emulsion is the classical phase inversion technique. We choose a silicone oil (polydimethysiloxane) as the dispersed phase, because it has an extremely low solubility in water. The low solubility of the oil in water prevents coarsening in size of oil droplets because oil molecules tend to transport from smaller to larger droplets, driven by their difference in interfacial pressure, provided the solubility is

significant. An ionic surfactant, sodium dodecylsulfate (SDS), is used as the emulsifying agent. We first dissolve 5 grams of SDS in 10 grams of water and slowly mix the solution in a Kitchen Aid mixer. At the same time, 100 grams of silicone oil is added to the mixer drop by drop. The mixing speed is kept low (around 1Hz) to avoid foaming. This step leads to a water-in-oil emulsion with very large droplets (>10 μm). We note that before the oil is completely mixed with the water it is very easy to produce a foam unless the mixing speed is kept low. If the mixture foams, the stirrer of the mixer becomes useless, because little shear stress can be exerted on the oil water mixture to break up large droplets. After the mixture becomes plastic-like, this emulsion is then inverted to an oil-in-water emulsion by increasing the mixing speed. The high shear rate breaks the large droplets into smaller ones. The emulsion is mixed for an hour until the droplet sizes reach the desired value. During the mixing, a few droplets of water must be added occasionally to compensate for the evaporated water. Usually we check the samples under an optical microscope to make sure the size distribution is good. At this stage the volume fraction of the dispersed phase (oil) is around 90% and the droplet diameter varies from about 0.2 μm to 2 micrometers. We keep this high volume fraction emulsion in a container as a stock. When the container is shaken, it vibrates as if an elastic material is inside. We note that there are other efficient methods to make crude emulsions depending on the average size desired. For example, a microfluidizer can be used to make smaller and more uniform emulsions.

The method of the purification is based on the liquid-solid phase transition introduced by the attractive depletion interaction. It is well known that when the surfactant concentration is above the critical micelle concentration (CMC), the excess surfactant will form micelles in water. For SDS, CMC = 0.008 mol/l. Micelles are aggregates of surfactant molecules in solution. Such aggregates form spontaneously at sufficiently high surfactant concentration. They are structures in which the hydrophobic portions of the surfactant molecule associate together to form regions from which the solvent, water is

excluded. The hydrophilic head groups remain on the outer surface to maximize their interaction with water. Micelles of SDS are very small objects with a diameter, $d_m = 40\,\text{Å}$, and an aggregation number of 80 molecules. They are much smaller than the oil droplets which have a diameter of d~1 μm. Because of thermal motion, the small micelles keep bombarding the large oil droplets which feel a pressure from the small micelles. When two oil droplets come close to each other than the micelle diameter, the inter-droplet spacing becomes an excluded volume for micelles. Because micelles are expelled from this region due to the close proximity of the droplet interfaces, the pressure exerted over the surfaces of the two droplets becomes non-uniform. This results in an attraction between drops due to the non-compensated pressure. In the ideal gas approach developed by Vrij[8], a pressure of $n_m k_B T$ is exerted outside the exclude volume, where n_m is the micelle concentration, k_B is the Boltzmann constant and T is temperature. For the case of two oil droplets in contact, the depletion potential can be expressed as,

$$u(d) = -\frac{3}{2} k_B T \Phi_m \frac{d}{d_m}, \tag{4.1}$$

where d is the diameter of droplets, Φ_m is the micelle volume fraction. This equation provides a simple linear dependence of the contact potential on the micelle volume fraction Φ_m and on the ratio d/d_m. The range of the potential is equal to the micelle diameter, d_m.

The attractive depletion interaction described by Eq. 4.1 will cause phase separation if the interaction is stronger than the thermal energy, $k_B T$, causing the droplets to aggregate into clusters or flocs. With time, these flocs separate from the dilute phase and form a cream on the top of the sample because of the density difference of the oil and water. Since the interaction increases with droplet size, at a certain micelle concentration Φ_m, only droplets larger than some size can flocculate and cream to cause phase separation. We refer to the cream as the solid state phase, by comparison with the droplets dispersed

uniformly in water which are the liquid phase. For a monodisperse sample the equation describing the liquid-solid phase boundary has been shown to be[7],

$$\Phi_m = \frac{d_m}{9d}(-\ln\phi + \Delta\mu_0 - 6w), \tag{4.2}$$

where ϕ is the volume fraction oil droplets; $\Delta\mu_0$ is the difference between the two reference chemical potentials in the solid phase and the liquid phase; and w is the van der Waals interaction potential at contact. From a thermodynamic point of view, it is the chemical potential difference that causes the solid-liquid phase transition. This flocculation phenomena can then be used to produce monodisperse samples because of the extreme sensitivity of the liquid-solid transition (via the depletion interaction) to the droplet size. We note that the phase transition occurs at higher surfactant concentrations values as the droplet diameter decreases; thus, at a certain surfactant concentration, small droplets remain dispersed while larger droplets phase separate. This is the key point of this method.

For the purpose of purification, the polydisperse emulsion is diluted with pure water to volume fraction of 10%. The surfactant (SDS) is added to the emulsion so that the concentration is above the critical micelle concentration (0.008 mol/l) to maintain stability. Figure 4.1a shows the initial polydisperse emulsion with a volume fraction of 10%. When we add more surfactant, we observe the effects of the depletion interactions. Figure 4.1b shows the phase separation. In this case the surfactant is added to a value of 0.03 mol/l. We see the sensitivity of the phase separation to the size of the droplets; the bigger droplets are mainly trapped in the flocs which, under gravity, will become the upper cream at the macroscopic level. Most of the small droplets are still dispersed in the water. When we do the purification, we want to fractionate the size of droplets as narrowly as possible. Usually several steps of purification are needed to reach a very monodisperse sample. The added amount of SDS is adjusted to the point where large droplets start to flocculate. A good way to check this is by observing the emulsion under an optical microscope; we can

see the large droplets start to flocculate while most of the small droplets remain dispersed. The emulsion is then poured into a cylindrical beaker. After 24 hours the upper cream which has separated from the dilute phase is removed and retained. More surfactant is then added to the dilute phase.. After another 24 hours, the cream is again removed and saved, and more surfactant is again added to the dilute phase. However, before we add surfactant to the dilute phase, we first clean the beaker because large droplets always tend to stick on the wall of the beaker. After these operations have been done, a set of creamed samples have been separated, each with oil volume fraction close to 50%. To further purify these, each sample is then diluted with filtered and deionized water to an oil volume fraction of 10%, and the preceding operations are repeated with different suitable surfactant concentration. To facilitate the purification, we usually keep the volume fraction of emulsion at a moderate value (~10%) so that the droplets have enough chance to encounter each other but also enough room to separate from each other. In Reference 6, Bibette draws a schematic diagram to illustrate the further purification steps. If the sample is precious (for example, if we want to purify an expensive isotopic oil-water emulsion), it is better to follow the diagram, and save the sample in each step. However, we often wish to focus on just one size, depending on our needs and the size distribution of the crude emulsion. In this case we repeat the purification operation several times by cutting the front and the tail of the size distribution. First, we adjust the surfactant concentration to cause only a small amount of droplets to form a cream, which contains mostly the largest emulsion droplets; we then remove the cream. Second, we add more surfactant to allow the central part (most of the dispersed droplets) to cream, and keep it while disposing of the dilute dispersion, which contains the smallest emulsion droplets. We go on to purify the central part of the droplet distribution in the cream by repeating the operation until we reach the required polydispersity. The strategy of adding surfactant each time is to use a larger step in the first two purification stages, for example, 0.005 ~ 0.01 Mol/l, and a finer step (0.002 Mol/l) for later steps. The finer the step, the more

uniform the size. This method of purification is most effective to purify particle sizes from 0.2 μm to 2 μm, independent of whether the density of the dispersed phase is higher or lower than that of the suspending fluid. For particles larger than 2μm Brownian motion becomes too slow and thermodynamic equilibrium is not easily achieved with gravity. To purify even smaller droplet sizes, we can use an ultra-centrifuge to separate different sizes by controlling the speed.

The procedure is stopped when the size distribution becomes so narrow that strong iridescence is clearly visible when the cream is deposited between glass plates. Fig. 4.2 shows a microscope picture of the purified monodisperse emulsion. The sample has been purified using eight steps. We see beautiful crystallization of emulsion droplets under an optical microscope. If we shine a laser on the sample we can see Bragg diffraction peaks on the scattering screen, confirming that there is a long range order in our sample. It has been shown in calculations, computer simulations and experiments[9], that the crystallization of a hard sphere colloidal suspension is suppressed when polydispersity, defined as the standard deviation of the particle size distribution divided by its mean, exceeds a critical value which lies in the range 6 to 12%. We have also measured the polydispersity of the sample using dynamic light scattering[10] and static light scattering. In dynamic light scattering, we dilute a emulsion sample to $\phi = 10^{-4}$, and measure the temporal intensity correlation function of the scattered light. The correlation function has an exponential decay; the decay time of the exponential and the scattering angle are used to determine the diffusion coefficient D_0. From the Stokes-Einstein relation $D_0 = k_B T/6\pi\eta a$, we get the hydrodynamic radius $\bar{a}$, the cumulants fit of the correlation function gives the standard deviation δa. Static light scattering has also been used to determine the polydispersity of the droplets. The time-averaged intensity as function of angle is measured, and a fit of the intensity profile with peeks and minima using Rayleigh-Gans approximation with Gaussian distribution of droplet sizes determined $\bar{a}$ and δa. The measured polydispersity, $\delta a/\bar{a}$ is 5%. In fact, given enough time for the system to

reach equilibrium, like hard sphere dispersions, our emulsion samples form bulk crystals at a appropriate volume fraction. This gives another proof that our monodisperse samples can be as monodisperse as commercial hard sphere dispersions. The monodisperse emulsions provide us a model system to study the properties of liquid droplet dispersions.

REFERENCES

1. P. Becher, *Emulsions: Theory and Practice* (Reinhold, New York, 1965).
2. C.G. Sumner, *Clayton's The theory of Emulsions and Their Technical Treatment,* 5th Ed.; Blakiston: New York, 1954.
3. M.J. Roson, *Surfactants and interfacial Phenomena*, 2nd ed.; Wiley: New York, 1989.
4. K.J. Lissant, *Demulsification: Industrial Applications*; Surfactant Science Series 13 Dekker: New York, 1983; Vol 13.
5. J. Bibette, D. Roux and F. Nallet, *Phys. Rev. Lett.* **65** 2470 (1990).
6. J. Bibette, *J. Colloid Interface Sci.* **147** 474 (1991).
7. J. Bibette, D. Roux and B. Pouligny, *J. Physique* II **2** 401 (1992).
8. A. Vrij, Pure *Appl. Chem.* **48** 471 (1976).
9. P.N. Pusey, *J. Physique* **48** 709 (1987); and references therein.
10. B.J. Berne and R. Pecora, *Dynamic Light Scattering*, Wiley; New York, 1976.

CHAPTER V

CONCENTRATED MONODISPERSE EMULSIONS NEAR THE GLASS TRANSITION STUDIED BY LIGHT SCATTERING

5.1. Introduction

There has been a substantial recent increase in the understanding of liquid-glass transitions(GT), both theoretically and experimentally[1-8]. A glass is a metastable state, which is formed when the rate of cooling is much higher than the rate of structure adjustment of the liquid to form a crystal. Similar to atomic fluids, colloidal suspensions also exhibit transitions from a fluid-like phase to a glass phase[5]. Usually, for an atomic fluid, a transition from a liquid to a glass is controlled by temperature; by contrast, for a colloidal suspension, the volume fraction of the dispersed phase is the parameter that controls the transition. As the dynamics of colloidal particles are much slower than those of atoms, crystallization takes place slowly enough to allow the study of the dynamics of glass states.

Among many theoretical descriptions of liquid-glass transitions, mode coupling theory (MCT) has been shown to give a good description of the dynamics of liquid-glass transitions for both simple liquids and colloidal suspensions[1,3]. The physical picture is the concept of caging: as the density increases the particles in supercooled liquids or concentrated colloidal suspensions become trapped for increased periods of time in cages formed by their neighbors. As neighboring particles are themselves caged, any mechanism for transport over larger distances must be cooperative in nature, i.e., many particles have to move collectively, leading a prolonged decay of correlation of density fluctuations.

It has been shown that MCT can be applied to the analysis of the glass transition in suspensions of identical particles with hard-sphere like interactions[4,5]. Dynamic and

static light scattering techniques were used to study the dynamics near the glass transition. The critical volume fraction and the MCT exponent parameter, which depend on the nature of the microscopic interactions, were extracted from the data analysis, and the scaling behavior predicted by MCT was observed. Thus there is clearly a need for further investigation of different systems, varying the interaction potential and, possibly, the shape of the particles.

Emulsions are dispersions of one liquid dispersed in a second liquid. The shapes of liquid droplets are flexible even though the equilibrium shape is spherical. Because of the deformability of liquid droplets, the packing fraction of the dispersed phase is allowed to be much higher than that of hard spheres. Like a hard sphere colloidal dispersion, an emulsion behaves like a viscous fluid at a low volume fraction of dispersed phase, while it behaves like a solid at a very high volume fraction. The origin of the high elasticity of these compressed emulsion has attracted considerable attention. Here, we investigate whether there also exists a glass transition in an emulsion, which is similar to the glass-transition in a solid sphere colloidal dispersion . Because of the flexibility of the dispersed phase we expect different dynamic properties, especially near and above the glass transition. With the successful fabrication of stable and monodisperse emulsions, we can study the dynamics of emulsion systems using light scattering techniques.

Conventional dynamic light scattering (DLS) probes dynamics on the length scale of the laser wavelength. It is therefore suitable to measure the structure relaxation as the glass transition occurs in emulsions. On the temporal scale modern correlators can measure from 10^{-8} sec to 10^{4} sec. Concentrated emulsions, both oil-water and water-oil, scatter light very strongly due to the mismatch of refractive indices between the oil and water. To make DLS feasible in this system, we have to restrict the scattered light to the single scattering limit. We do this by choosing a solution as a continuous phase whose refractive index matches that of the dispersed phase so that the sample looks nearly transparent. Then, the temporal correlation function of scattered light reflects dynamics of

density fluctuations of the scattering system. As the system approaches the glass transition, an individual droplet nearly touches the neighboring droplets. Due to thermal excitations, the individual droplet can only diffuse a very short distance before it collides with its neighbors. At these high volume fractions, conventional DLS can not resolve the motion of an individual droplet because the distance it can move is much less than the laser wavelength. Moreover, at such high volume fractions the individual droplet motion may exhibit non-diffusive behavior because of the strong interparticle interactions and because of the flexibility of the droplet shapes. To resolve the dynamics on such short length scales, we apply diffusing-wave spectroscopy (DWS) to measure the highly restricted particle motion. Diffusing-wave spectroscopy extends conventional dynamic light scattering to the highly multiple scattering limit, and probes dynamics on length scales much shorter than the laser wavelength. Because concentrated emulsions scatter light very strongly, DWS is an ideal technique to study short length scale dynamics by taking advantage of multiple scattering.

It is important to study the microscopic dynamic properties of concentrated emulsions near the glass transition, and to understand the corresponding macroscopic properties and their microscopic origin. Partial arrest of density fluctuations occurs near the glass transition and there exists a maximum mean square displacement for individual droplets. DWS is able to probe the small amount of displacement. From the equipartition principle, we know each droplet carries the translational energy of order of $k_B T$. By making very simple assumptions we can extract the storage modulus of the emulsion. This technique provides a promising method to determine the elasticity of colloidal systems[9].

In the following section(5.2), we present our experimental study of the liquid-glass transition in concentrated emulsions using conventional DLS and we apply the MCT to analyze our data. In Section 5.3, we apply DWS to study the microscopic motion of individual droplets, and we present a simple method to extract the storage modulus of

emulsions using light scattering techniques. A brief conclusion is given at the end of this chapter.

5.2. Liquid-Glass Transition of Monodisperse Emulsions Studied by Dynamic Light Scattering

Monodisperse emulsion samples were prepared using the method of fractionation[10]. The monodisperse emulsion is comprised of silicone oil droplets in water, stabilized with sodium dodecylsulfate(SDS). In order to make conventional laser light scattering applicable, we add glycerol into the continuous phase of the emulsion so that the refractive index of the glycerol-water mixture matches that of the oil droplets. Then the dilute emulsions are concentrated to higher volume fractions using centrifugation. The emulsion droplets cream under high effective gravity due to their density difference with the solvent. We then take out the extra solvent (glycerol-water mixture). Using a desk-top centrifuge an emulsion can be concentrated to $\phi \approx 70\%$, where the emulsion is apparently in a glass state since it does not flow at all under normal gravity. To vary the volume fraction of dispersed phase, we dilute the concentrated emulsion by adding a carefully measured mass of glycerol-water mixture. As the volume fraction is further decreased, the emulsion starts to show very viscous flow. We use dynamic light scattering to quantitatively characterize the liquid-glass transition.

Dynamic light scattering measures the temporal autocorrelation function of the intensity, $I(q,t)$, of the scattered light defined by

$$g_T^{(2)}(q,t) = \frac{\langle I(q,0)I(q,t)\rangle_T}{\langle I(q,t)\rangle_T^2}, \tag{5.1}$$

where t is the correlation delay time and $\langle\ \rangle_T$ symbolizes a time average. The scattering wave vector, q, is given by

$$q = \frac{4\pi n}{\lambda}\sin(\theta/2), \tag{5.2}$$

where n is the refractive index of the continuous medium, λ the wave-length of the laser light in vacuum, and θ the scattering angle. If the scattering system is ergodic, the electric field amplitude is a zero mean Gaussian variable, and the time average is equal to the ensemble-averaged intensity correlation function, $g_E^{(2)}(q,t)$, which is related to the qth mode of the density fluctuations, the so called intermediate scattering function(ISF), $f(q,t)$, via

$$g_E^{(2)}(q,t) = \frac{\langle I(q,0)I(q,t)\rangle_E}{\langle I(q,t)\rangle_E^2} = 1 + \beta|f(q,t)|^2, \tag{5.3}$$

$$f(q,t) = \frac{S(q,t)}{S(q)}, \tag{5.4}$$

Here, $\langle\ \rangle_E$ indicates an average over all ensembles of scatterers, and $S(q,t)$ and $S(q)$ are the dynamic and the static structure factors, respectively. For a monodisperse system, $S(q,t)$ is given by

$$S(q,t) = \frac{1}{N}\left\langle \sum_{i=1}^{N}\sum_{j=1}^{N} \exp\left\{i\mathbf{q}\cdot\left[\mathbf{r}_j(t) - \mathbf{r}_i(0)\right]\right\}\right\rangle. \tag{5.5}$$

For a nonergodic glass phase the time average and ensemble average are no longer equivalent. Pusey and van Megen[11] have proposed a procedure for estimating the ISF from the measured time-averaged intensity autocorrelation function that is more straight forward than that by measuring an average over many sub-ensembles. The model assumes that the particles are able to execute only restricted (Brownian) excursions about an amorphous distribution of fixed average positions and the correlation in these excursions decays to zero in the course of a measurement. The relationship between the density fluctuations $f(q,t)$ and the measured time averaged intensity autocorrelation function $g_T^{(2)}(q,t)$ is [11]

$$f(q,t) = 1 + (I_T/I_E)\left\{\left[g_T^{(2)}(q,t) - g_T^{(2)}(q,0) + 1\right]^{1/2} - 1\right\}, \tag{5.6}$$

where $I_T = \langle I(q) \rangle_T$ is the time-averaged intensity and is given by the average number of photon accumulated during a particular measurement. The ensemble-averaged intensity is $I_E = \langle I(q) \rangle_E$ and may be determined from the photon counts accumulated while the sample is moved gently at constant speed in the laser beam.

We have measured the structure factor $S(q)$ of a concentrated emulsion by static light scattering. Usually for a monodisperse system the measured average intensity of the scattered light is the product of the form factor of a single particle, $F(q)$ and the structure factor, which represents the spatial correlations of the particles. To extract the structure factor, we divide the measured intensity from the concentrated sample $I(q)$, by the scattering intensity of a dilute sample, where there is no spatial correlation so that $S(q)$=1. In Fig. 5.1 we show the measured structure factor of a monodisperse emulsion with a droplet radius of 0.5μm, and a volume fraction $\phi \approx 0.70$. At this high volume fraction we observe a pronounced peak at $q_m \approx \frac{2\pi}{d}$, where d can be regarded as the average distance between nearest neighbors. The structure factor shown in Fig. 5.1 is typical of a highly random packed system. The first pronounced peak results from the short range spatial correlations of the particles packed in the concentrated emulsion. However, there is no long range order since we do not observe any diffraction spots for this concentrated sample.

We are concerned more about the dynamic properties when the emulsion experiences a liquid-glass transition. Dynamic light scattering directly measures the density fluctuations by measuring the temporal autocorrelation function of scattered light. Our basic results for the density fluctuations are shown in Fig. 5.2 for three different wave vectors. We plot the intermediate scattering function for several different volume fractions for each wave vector. The volume fractions are labeled by the effective volume

fractions because the ionic nature of the SDS surfactant adsorbed on surface of each droplet results in a shell of excluded volume that effectively increases the volume fraction of the dispersed phase[12]. The first structure peak is around $\theta = 49^{\circ}$. Near the glass transition, the arrest of density fluctuations is most prominent at the structure factor peak, so we study the dynamics of the emulsion around structure peak, at volume fractions spanning from 54% to 62%.

The decay of autocorrelation of density fluctuations shown in Fig. 5.2 can be divided into three relaxation stages. The initial decay is associated with the shortest length scale motion which is usually assumed to be diffusive, and is approximated by $\exp\left[-D(q)q^2t\right]$; $D(q)$ is the wave-vector dependent short time diffusion coefficient. The corresponding diffusive motion contributes only the first few percent of the total decay of $f(q,t)$. In fact, the details of the initial decay are already out of the resolution of conventional DLS, especially near and above the glass transition. We will discuss the dynamics of this short-length scale motion in detail in the following section. The following two relaxation stages can be measured with conventional DLS and are shown clearly in Fig. 5.2. For volume fractions above 58% there is prolonged decay of the small-scale diffusive motion, causing the density correlation function to decay only very slowly to a plateau, where the decay ceases. The plateau extends over several decades in time, and at time scale of seconds, there exists a final decay of the correlation function. In contrast, for volume fractions below 58%, the plateau regime shows a continuous but gradual relaxation, followed by the final decay. As the volume fraction decreases further , the final decay starts to merge with the prolonged initial decay.

To quantitatively analyze the density fluctuations of an emulsion near the glass transition, we apply the mode coupling theory (MCT) of the glass transition. The ideal MCT has been successfully applied to the liquid-glass transition in a hard sphere colloidal system. Here we give a brief account of MCT for the interpretation of the DLS results.

Mode coupling theory describes the dynamics of a liquid to glass transition through an equation of motion for the density autocorrelation function. Close to a critical packing fraction ϕ_c, the density autocorrelation function, $f(q,t)$ shows a two step decay, signaling the existence of two distinct relaxation processes, the α and the β processes. They are characterized by two time scales, τ_α and τ_β, respectively, which are both greater than the microscopic time scale t_0. In the ideal version of the MCT (no hopping term) for $\phi < \phi_c$ and near ϕ_c, the α and the β processes take place at well separated time scales, and $f(q,t)$ decays to zero at long times, By contrast, for $\phi > \phi_c$, only the β process remains, while the α process is frozen. Then, $f(q,t)$ saturates in time to a finite positive value, $f(q,\infty)$. Physically, this behavior has the signature of an ideal glass transition from ergodic to nonergodic behavior.

Mode coupling theory concerns the β process and its crossover to the α process. In the time regime $t_0 \ll t \ll \tau_\alpha$, the density autocorrelation function can be expressed as

$$f(q,t) = f_c(q) + h(q)G(t), \tag{5.7}$$

where $f_c(q)$ is the nonergodicity parameter and represents the amplitude of the arrested structure at the critical volume fraction, ϕ_c, and $h(q)$ is called the critical amplitude. Both $f_c(q)$ and $h(q)$ can in principle be calculated from the structure factor $S(q)$ at the transition. The β correlator, $G(t)$, satisfies a scaling law,

$$G(t) = |\sigma|^{1/2} g_\pm(t / \tau_\beta), \tag{5.8}$$

where σ is the separation parameter, given by

$$\sigma = c_0(\phi - \phi_c)/\phi_c, \tag{5.9}$$

where c_0 is a material dependent constant, which is close to 1. The master scaling function $g_\pm(t)$ is q-independent and also independent of concentration. Concentration dependence enters the dynamics only through the separation parameter σ and the scaling times τ_α and τ_β which diverge as the separation parameter approaches zero:

$$\tau_\alpha = t_0|\sigma|^{-\gamma}, \qquad \gamma = 1/2a + 1/2b, \tag{5.10}$$

$$\tau_\beta = t_0|\sigma|^{-\delta}, \qquad \delta = 1/2a. \tag{5.11}$$

The critical exponent a ($0<a<0.5$) and b ($0<b<1$) are related to the exponent parameter λ as follows:

$$\lambda = \Gamma^2(1-a)/\Gamma^2(1-2a) = \Gamma^2(1+b)/\Gamma^2(1+2b), \tag{5.12}$$

where Γ is the gamma function.

The most significant feature of MCT is its factorization of the spatial and temporal variables as indicated in Eq. (5.7). It suggests that localized dynamics (β process) promote relaxation of density fluctuations to the value $f_c(q)$. The final long time decay describes relaxation of $f(q,t)$ to zero, which satisfies another scaling law,

$$f(q,t) = f_c(q)F(q,t/\tau_\alpha). \tag{5.13}$$

Here, $F(q,t)$ is the α correlator, which is a q-dependent function. The α relaxation process can be well approximated by a stretched exponential,

$$f(q,t) = f_c(q)\exp(-(t/\tau_\alpha)^{\beta_q}), \tag{5.14}$$

where β_q is the stretching exponent. Within the ideal version of MCT, α relaxation only exists on the liquid side, and the process is arrested in the glass. In the glass, β relaxation persists but saturates to a definite value at long times.

We note that on the liquid side of the transition at a time regime for $t/\tau_\beta > 1$, the relaxation of the density correlation function is shared by both the β and the α processes, i.e., the final stage of β-process is the initial part of the α decay. Therefore, the time τ_β marks the crossover from β process to α process.

In the extended MCT, a thermal hopping term is included in calculating the β correlator, $G(t)$. If there are some vacancies in a disordered system, a particle may move from one place to some vacancy. In the MCT treatment, this refers to phonon assisted transport phenomena. The mechanisms of hopping differ for different systems. The hopping term results in the final decay of the correlation function even on the glass side of the transition, restoring ergodicity to the system at sufficiently long times.

The predictions of the mode coupling theory may be given the following physical interpretation. The β process describes the dynamics of localized particle motion, as if a particle moves in a cage which is formed by its neighboring particles. As the neighboring particles are themselves caged, any mechanism for a large distance relaxation must be cooperative in nature, leading to a prolonged decay of correlations. The α process describes the breakdown of the particle cages and formation of new cages, which results in the relaxation or rearrangement of the microstructure of the dispersed phase.

To quantitatively analyze our data we begin by calculating the β correlator $G(\sigma,t)$ in the ideal MCT regime (no hopping term). For a trial exponent parameter λ, the β correlator is only σ-dependent and therefore, ϕ-dependent. We then fit the data of the autocorrelation functions of density fluctuations according to Eq. (5.7). For a certain scattering angle we first approximately locate the level of $f_c(q)$ by taking the value of the plateau of the density correlation function for the volume fraction between 0.57 and 0.58 because the plateau of the correlation function becomes flat as the volume fraction changes from $\phi = 0.57$ to $\phi = 0.58$. We then try an appropriate $h(q)$ so that the curve of the β process can be scaled onto the data. We combine the α process (Eq. (5.14) and the β process Eq. (5.7) in which we allow $G(t)$ to scale horizontally and we use τ_α as a fitting parameter to fit the final long-time decay. From the data, it is obvious that on the glass side of the concentrated emulsion, the correlation function still shows a final relaxation, *i.e.*, the plateau of $f(q,t)$ decays to zero at a long time. To fit our data, within the extended MCT, we turn on a small hopping term in calculating the β correlator so that ISF always decays to zero at long times. In doing our fit, for a chosen scattering angle we fix $f_c(q)$ and $h(q)$ since according to MCT, they are approximately independent of volume fractions near the transition regime. We choose another pair of $f_c(q)$ and $h(q)$ when we fit a group of data for a different scattering angle. This way we satisfy the constraints of MCT for the factorization of $f(q,t)$.

As shown in Fig. 5.2, using the extended MCT, the density correlation function can be fitted very well on both liquid and glass sides of the transition for different scattering angles near the structure peak. From the fitting, we extract the scaling times τ_β and τ_α and these are plotted in Fig. 5.3 as functions of ϕ. For comparison, we also plot the ϕ-dependence of the scaling times predicted by MCT(Eqs. (5.10) and (5.11)). Good agreement is obtained between the experimental scaling time and that predicted by MCT, as shown in Fig. 5.3.

The q-dependence of $f_c(q)$, and $h(q)$ is shown in Fig. 5.4. The non-ergodic parameter, $f_c(q)$, shows a peak around $q_m = 14.2(\mu\text{m})$, which is just at the structure factor peak, while the critical amplitude, $h(q)$, exhibits a shallow minimum at the structure factor peak. The solid line is the theoretical prediction by MCT for a hard sphere system[13]. Again reasonably good agreement is obtained.

We note that there exist similarities between the glass transition for a hard sphere dispersion and the for an emulsion: (1) for monodisperse emulsions, there exists a critical transition volume fraction ϕ_c, which falls between 57% and 58%, (2) the critical exponent of the transition of a monodisperse emulsion is close to that of a hard sphere system, (3) the ϕ-dependence of the scaling times for both the α and β processes obey the same scaling laws for both systems, and (4) the q-dependence of non-ergodic parameter, $f_c(q)$, and critical amplitude, $h(q)$, follow the same trend as that of a hard sphere system, where $f_c(q)$ is peaked at the structure factor peak and $h(q)$ exhibits a minimum around the structure peak. However, the distinguishing feature is obvious: for a hard sphere system the final decay(α process) arrests on the glass side of the transition[13], *i.e.*, the structure relaxation is frozen, while for an emulsion system, there always exists a final decay at long times on the glass side. We believe that this final decay results from the flexibility or shape fluctuations of liquid droplets which give the rise to the residual structure relaxation even on the glass side. This feature is even more obvious in diffusing-wave spectroscopy measurement which we will discuss in the following section.

5.3. Short Length Scale Motion of Emulsion Droplets Studied by Diffusing-Wave Spectroscopy

In the previous section we have studied the density fluctuations of concentrated emulsion near the glass transition using a conventional DLS technique. Mode coupling theory is able to explain the two-step relaxation of the density fluctuations beyond microscopic time scale. Because the individual droplet's motion is severely restricted near the glass transition, the early time relaxation of density fluctuations is out of the resolution of conventional DLS. To resolve microscopic motion of individual emulsion droplets, we apply DWS to measure the mean square displacement of the droplets. The principles and detailed measurements of DWS have been published elsewhere[14-16]. Diffusing-wave spectroscopy also measures the temporal autocorrelation function of the intensity of the scattered light. However, DWS is sensitive to a particle motion on the length scale of $\lambda/\sqrt{N}$, where λ is the wavelength of the laser light, and N is the average number of times a photon is scattered in the scattering medium, which in the transmission geometry can be approximated as $N \approx (L/l^*)^2 l^*/l$, where L is the sample cell thickness, l and l^* are the scattering mean free path and the transport mean free path of the scattering medium, respectively. It indicates that the relevant length scale can be adjusted by varying the thickness of the sample cell.

The measured temporal intensity autocorrelation functions from DWS for the emulsion sample at different volume fractions are shown in Fig. 5.5. The monodisperse droplets have a diameter of 1.4μm in diameter and are made with an oil with a viscosity of 1000 cP. We choose a sample cell with a thickness of 7 mm to ensure we can safely apply DWS by satisfy the condition $L/l^*>10$ at all times. The data shown in Fig. 5.5 are normalized intensity correlation functions for various volume fractions ranging from 15% to 80%. The data for each volume fraction are collected for two hours to increase the signal-to-noise ratio. For the high volume fraction data, we need to sample several

positions of the cell and take the average of the correlation functions to make sure that the system has been ensemble-averaged. It is interesting to note that at high volume fractions the feature of the correlation functions looks similarly to those measured by conventional DLS data, but the plateau shows up at a significantly higher volume fraction, about 62%. Above, 62%, the correlation function exhibits two step decay. The two steps are separated by an intermediate region and the extent of this region increases with the volume fraction. The first prolonged decay covers two decades of time which happens between 10^{-2} msec and 1 msec and this decay saturates at a certain value for several decades of time; then these is another decay at times around a few minutes. This is a characteristic behavior of DWS measurements for our emulsion samples which are similar to the conventional DLS data near the glass transition. We note that up to $\phi = 0.80$, where the emulsion is in deep glass phase, there still exists the pronounced final decay of the correlation function. As compared with the conventional DLS data, the two step decay of the DWS correlation functions indicates even on the length scale of $\lambda/\sqrt{N}$, there still exist two dynamic relaxation processes which may relate to the α and β processes predicted by MCT.

To analyze the DWS data, we need to invert the correlation function and obtain the physical quantity, mean square displacement, $\langle \Delta r^2(t) \rangle$. To do the inversion of the correlation function we should determine the transport mean free path, l^* independently. We measure l^* through the static transmission measurement[16], in which we compare the relative static transmission between the emulsion sample and a reference sample of known l^*. With the independently measured l^* we invert the correlation function and calculate the mean square displacement.

Figure 5.6 shows the mean square displacement for various volume fractions in a double logarithmic plot. We note the length scale that DWS is sensitive here is from a few angstroms to tens of angstroms. For motion at similar length scale, the correlation function in conventional DLS would only show decay of a few percent. Actually, we may

estimate the amount of the correlation function decay through the intermediate scattering function in the high q limit, $f(q,t) = \exp(-q^2 \cdot \langle \Delta r^2(t) \rangle / 6)$. At time scale of 1 msec, taking the corresponding $\langle \Delta r^2(t) \rangle$ from Fig. 5.6, we find that $f(q,t)$ only decays to 0.98 for $\phi = 55\%$, and $f(q,t)$ decays much less for higher volume fractions. However, on this length scale, DWS is able to reveal more detailed dynamics.

As shown in Fig. 5.6, at volume fractions below 45% we note that except for a minor transient hydrodynamic interaction effect[15], the particle motion looks like simple diffusion with $\langle \Delta r^2(t) \rangle \propto t$. In a double logarithmic plot, it shows the slope of 1 at relatively long times. This is the characteristic behavior of simple translational diffusion. It implies that oil droplets of this high viscosity behave more or less like hard spheres at low volume fractions. By contrast, at high volume fractions, the motion of the droplets is severely restricted by their neighbors and individual droplets can only move locally until the collective droplets' rearrangements occur. As shown in Fig. 5.6, at volume fractions above 55% there obviously exists a maximum mean square displacement for each individual droplet before they rearrange themselves nonlocally. We have not tried to invert the data of the second decay of the correlation function since it involves the structure relaxation and in that case the density fluctuation reflects cooperative motion of a large number of particles. And we have found the time scale of the second decay depends on the history of loading the sample and usually the characteristic decay time increases with time evolution, i.e., the sample is slowly approaching a steady state.

Colloidal dispersions at high volume fractions near or above the glass transition show similar behavior, i.e., at times shorter than the structure relaxation, there exists localized motion of each individual particle. This localized particle motion gives rise to the first relaxation of density fluctuations. To provide more quantitative analysis of individual droplet motion, we first consider what is perhaps the simplest model of this localized particle motion. We suppose that the particles are restricted to the neighborhoods of random fixed positions by a harmonic force. When an external harmonic restoring force is

added in a Langevin equation which describes the dynamics of a harmonic bound Brownian particle, the time-dependent mean square displacement of a particle is given as[17,18]

$$\left\langle \Delta r^2(t) \right\rangle = 6\left\langle \delta^2 \right\rangle \left[1 - \exp\left(-\frac{D_0 t}{\left\langle \delta^2 \right\rangle} \right) \right], \tag{5.15}$$

where $\left\langle \delta^2 \right\rangle$ is the maximum mean square displacement, D_0 is the free particle diffusion constant. It shows an exponential saturation of the mean square displacement. We note that the short-time expansion of Eq. (5.15) gives a free particle diffusion, so that a particle initially diffuses as if it were free; only over longer times is the effect of restriction imposed by the harmonic force felt.

As shown in Fig. 5.6, for volume fractions above 55%, the mean square displacement shows a gradual saturation, where the effects of restriction appear. We try to use Eq. (5.15) to fit the higher volume fraction data, and find that the fitting is very poor, even at early times(corresponding to short length scales). We find that there exists an obvious deviation from the linear relationship between $\left\langle \Delta r^2(t) \right\rangle$ and t at early time on the length scale of 10 Å. Even at that short length scale, the mean square displacement data show a stretched behavior, i.e., $\left\langle \Delta r^2(t) \right\rangle \propto t^{\alpha}$, with $0<\alpha<1$. As we know, the direct interactions between the droplets are more pronounced at high volume fractions and more complicated forces other than a simple harmonic force start to dominate. Then the mean square displacement may exhibit a more complicated functional form. Even though the physical meaning of the stretched behavior of the mean square displacement is not clear, we are still able to extract a more physical quantity, the maximum mean square displacement $\left\langle \delta^2 \right\rangle$ of an individual droplet which can be related to other macroscopic properties of emulsions.

A stable emulsion is a complex fluid that can behave both as a fluid or as a solid and can show viscoelastic behaviors when the volume fraction of dispersed phase is increased.

The elasticity is characterized by the elastic modulus which reflects the storage of mechanical energy, while the viscous behavior is characterized by the loss modulus which reflects the dissipation of energy. At low volume fractions, the loss modulus plays a dominant role in the response to an external excitation, where the system behaves like a viscous liquid. At high volume fractions the elastic modulus starts to dominate over the loss modulus where the system behaves like a solid. The unique feature is the elasticity of high volume fraction emulsions which results from the surface tension and the deformation of liquid droplets. Unlike solid sphere colloidal system the packing volume fraction of dispersed phase of an emulsion can be much higher than that of a solid dispersion because of the deformability of droplets. Because at a high volume fraction above the glass transition the motion of individual droplets is restricted locally, using dynamic light scattering, we may measure the maximum mean square displacement of the monodisperse emulsion droplets and with a simple assumption, we can relate it to the storage modulus.

The response of a complex fluid at equilibrium to thermal excitations can be probed by the ensemble averaged motion of particles dispersed in the fluid. At very high volume fractions, an individual particle motion is severely restricted by its neighbors and we may assume that the motion of an individual drop behaves as a bound oscillator whose maximum displacement is determined by the available free space for each droplet and the elasticity of the system. The elastic energy for each droplet results from deviation of a droplet from its equilibrium position, which is just the storage modulus multiplied by the square of the strain. We may express the maximum elastic energy of each droplet as

$$E = \frac{1}{2} G' \frac{\langle \delta^2 \rangle}{d^2}, \tag{5.16}$$

where G' is the storage modulus of the system and d is the diameter of an oil droplet. From the equipartition principle, each droplet carries $\frac{3}{2} k_B T$ translational kinetic energy due to the thermal excitations and this energy should balance its elastic energy for the

strain due to its maximum mean square displacement in a medium with an storage modulus, G'. The equation is then given by

$$\frac{\frac{3}{2}k_B T}{V} = \frac{1}{2}G'\frac{\langle \delta^2 \rangle}{d^2}, \tag{5.17}$$

where V is the volume occupied by a droplet. From the maximum mean square displacement we derive G' and plot it in Figure 5.7. For comparison we also plot the real part of complex shear modulus determined by mechanical means using a rheometer, making a linear stress-strain measurement. The agreement is surprisingly good. Both data show there exists a sharp increase in the modulus at volume fractions around 60%. Thus above 60% the emulsion turns from liquid like into solid like. We note that at this volume fraction the dispersed droplets almost reach random close packing, *i.e.*, packing constraints begin to force them to touch each other. Further increase of the volume fraction of the dispersed phase will cause the droplets to begin to deform, and additional surface energy is imparted on each individual droplet.

The elastic modulus in a linear viscoelastic regime is usually determined by measuring the stress response to a small strain applied mechanically through a rheometer. In the above approach we extract elastic modulus using dynamic light scattering. Dynamic light scattering measurement may be generalized to determine linear viscoelastic moduli of a complex fluid[9]. The optical measurement provides a promising technique to study rheological behaviors of complex fluids.

5.4. Conclusion

We have studied the liquid-glass transition of monodisperse emulsions using dynamic light scattering. We have shown that like a hard sphere colloidal system emulsions exhibit a liquid-glass transition at the volume fraction of dispersed phase between 57% and 58%.

We have applied mode coupling theory to analyze the intermediate scattering function and have shown that in contrast to a solid sphere dispersion, the structure relaxation in an emulsion exists even on the glass side and the α relaxation persists to much higher volume fractions of dispersed phase. The very short length scale motion of emulsion droplets has been probed by diffusing-wave spectroscopy. It shows the droplet motion near the glass transition starts to deviate from simple diffusion on length scales as short as 10Å. Thus DWS provides a sensitive method to determine the microscopic dynamics of an emulsion near the transition regime. We also shown that it is possible to extract rheological properties of emulsions using dynamic light scattering, in which we relate the mean square displacement to the storage modulus.

*

* Part of the work reported in this chapter has been published in *Encyclopedia of Emulsion Technology*, **vol.4**, ed. P. Becker, Reinhold, New York, 1995, T.G. Mason, A.H. Krall, Hu Gang, J. Bibette, and D.A. Weitz, "Monodisperse Emulsions: Properties and Uses".

REFERENCES

1. H.Z. Cummins, W.M Du, M. Fuchs, W.Götze, S. Hilebrand, Latz, G. Li and N.J. Tao, Phys. Rev. **E47**, 4223 (1993)
2. P.N. Pusey and W. van Megen, *Nature* (London) **320**, 340 (1986)
3. P.N. Pusey and W. van Megen, *Phys. Rev. Lett.* **59**, 2083 (1987)
4. W. van Megen and P.N. Pusey, *Phys. Rev.* **A43**, 5429 (1991)
5. W. van Megen and P.N. Pusey, *Phys. Rev.* **E47**, 248 (1993)
6. W. Götze, J. Phys.: *Condens. Matter* **2**, 8485 (1990)
7. M. Fuchs, I. Hofacker and A. Latz, *Phys. Rev.* **A45**, 898 (1992)
8. W. Götze and L. Sjögren, *Rep. Prog. Phys.* **55**, 241 (1992)
9. T.G. Mason, Ph.D. thesis, Princeton University (1995)
10. J. Bibette, *J. Colloid Interface Sci.* **147** 474 (1991).
11. P.N. Pusey and van Megen, *Physica* **A157**, 705 (1989)
12. T.G. Mason, A.H. Krall Hu Gang, J. Bibette and D.A. Weitz, in "*Encyclopedia of Emulsion Technology*" Vol. 4 Ed. P. Becher
13. W. van Megen and S.M. Underwood, *Phys. Rev.* **E49** 4206 (1994)
14. D.A. Weitz and D.J. Pine, in "*Dynamic Light Scattering*: The Method and Some Applications" Ed. by W. Brown, (Oxford University 1993)
15. A.J.C Ladd, Hu Gang, J.X. Zhu and D.A. Weitz, *Phys. Rev. E*, in press
16. D.J. Pine, D.A. Weitz, P.M. Chaikin, and E. Herbolzheimer, *Phys. Rev. Lett.*, **60**, 2439 (1988)
17. G.E. Uhlenbeck and L.S. Ornstein, *Phys. Rev.* **36**, 823 (1930)
18. Ming Chen Wang and G.E. Uhlenback, *Rev. Mod. Phys.*, **17**, 323 (1945)

CHAPTER VI

THERMAL FLUCTUATIONS OF THE SHAPES OF DROPLETS IN DENSE AND COMPRESSED EMULSIONS

ABSTRACT

We generalize the theory of diffusing wave spectroscopy (DWS) to include the effects of fluctuations of the amplitudes of the scattered fields. Thus DWS can be used to probe the internal dynamics of flexible particles. We study the thermally induced shape fluctuations of monodisperse emulsion droplets as a function of the droplet volume fraction, ϕ. We find that a droplet's mean-squared deviation from spherical shape increases with ϕ, while the characteristic rate of relaxation of the shape deformations decreases with ϕ. Our generalization of the theory of DWS allows us to measure the autocorrelation function of the fluctuating amplitude of the field scattered from a droplet. We use fluid dynamics and scattering theory to calculate this autocorrelation function theoretically for an isolated droplet. The significant contribution of many independent modes of deformation results in a distinctly non-exponential relaxation. The measured behavior agrees with the theory as ϕ approaches zero. At higher ϕ throughout the range of colloidal liquids we find a surprising scaling behavior which implies that particle interactions bring about the enhancement and slowing down of shape fluctuations without altering the spectrum of excited deformation modes. We relate the form of the scaling function to the particle radial distribution function. In "compressed" emulsions with ϕ as high as 0.8, shape fluctuations may be the only dynamical behavior that can occur. We

suggest that in these systems the amplitude of the shape fluctuations is related to the emulsion's elastic modulus.

6.1 . Introduction

Dispersions of one liquid in another immiscible liquid are called emulsions. Emulsions have long been of great practical interest; typical uses include foods, cosmetics, pharmaceuticals and agricultural products[1,2]. In most emulsions, the sizes of the droplets of the dispersed phase range from sub-microns to several microns. In contrast to microemulsions which are thermodynamically stable, emulsions are inherently unstable. However, by appropriately choosing the surfactant, which adsorbs on the interface between the two immiscible liquids, and stabilizes the droplets, emulsions can be kinetically stable nearly indefinitely, allowing their properties to be studied.

Emulsions exhibit many properties similar to those of dispersions of solid particles. The droplets of the dispersed phase execute Brownian motion in the fluid and the viscosity of the dispersion increases with their volume fraction. However, the physical properties of the interface are quite different; liquid droplets are flexible and their interfaces are therefore subject to thermal fluctuations. As a result, the shape of the droplets fluctuates and is itself a dynamic variable. The extra degree of freedom introduced by thermal shape fluctuations may have significant consequences for the properties of the emulsion; in particular, as the volume fraction, ϕ, is increased, the interaction between droplets may change because of this extra degree of freedom, and this may be reflected in the macroscopic properties of the emulsion. Moreover, the physical properties of the interfaces directly impact the formation and stability of an emulsion. Thus, to fully explore the differences between dispersions of solid particles and liquid droplets requires the study of the shape fluctuations of the emulsion droplets. This may lead to an improved understanding of the stability and rheological properties of emulsions.

Thermally induced fluctuations on interfaces between two fluids are the well known capillary waves. The amplitude of these capillary waves is controlled by the surface tension between the fluids, Γ, and is typically very small, of the order of ten angstroms for

the commonly encountered values of the surface tension. Nevertheless, for flat interfaces capillary waves have been observed using both light[3] and X-ray scattering[4]. Thermally excited capillary waves on the interface of liquid droplets are much more difficult to observe because of the more complex geometry and the possibility that the interfacial fluctuations are coupled to other degrees of freedom, such as the translational motion of the droplets. However, thermal interfacial fluctuations of dispersions of other flexible particles have been observed; for example, shape fluctuations of micelles and microemulsions have been studied with neutron spin echo measurements[5,6], while those of liquid membranes have been observed with X-ray scattering[7] and those of vesicles have been studied with direct space imaging[8]. These systems share a number of distinct features. They are all suspensions of self-assembled structures. As a result, the interfacial tension is essentially zero, so that shape fluctuations are typically much larger, and thus, easier to observe. These fluctuations are controlled by the interfacial rigidity or bending energy rather than by interfacial tension; consequently, the structures fluctuate about non-spherical mean shapes. Typically one has to treat these dynamics phenomenologically by defining a free energy of bending. Moreover, these structures themselves have finite lifetimes, so the dynamics of these systems can include the birth and death of the constituent structures. Each system exists only over certain ranges of dispersed phase and surfactant concentrations, so that the full range of dispersed-phase volume fraction is not accessible for study. By contrast, the constituent particles of an emulsion are fluid droplets with a spherical mean shape controlled by the surface tension. The relaxation of the shape fluctuations can be predicted by hydrodynamics; the value of the interfacial tension, Γ, can be determined from macroscopic measurements. Moreover, the volume fraction of the dispersed phase can be varied continuously from zero to almost one, allowing the volume-fraction-dependent interactions to be studied. Thus, emulsions are a useful model system for studying shape fluctuations of dispersions of flexible particles.

Despite the potential interest and importance in studying the shape fluctuations of emulsion droplets, there are significant experimental difficulties, which have prevented their observation, until recently, two breakthroughs removed obstacles that have previously stood in the way of our observing and understanding the shape fluctuations of droplets in emulsions. The first obstacle is the requirement of monodisperse emulsion droplets; since the shape fluctuations and their dynamics depend on droplet size, a polydisperse emulsion would preclude any quantitative theoretical analysis. The second major obstacle is the very small amplitude and the rapid relaxation of thermal shape fluctuations of micron-sized liquid droplets whose shape is controlled by interfacial tension. The extra surface area created by thermal deformations from a spherical shape is $\Delta A \approx k_B T/\Gamma$, where k_B is Boltzmann's constant and T is the temperature. For a typical interfacial tension of Γ=10 dynes/cm, this extra surface area is only about 40 Å^2. If the radius of the droplet is $R \approx 1$ μm, the extra surface area corresponds to a relative variance from the mean spherical shape of only ~ 10^{-7}. Moreover, the relaxation time, τ, of these fluctuations is also very short. If the viscosity of the liquid comprising the drop is much greater than that of the continuous phase, the relaxation time is given by $\tau \approx R\eta/\Gamma$; for η = 10 cP, $\tau \approx 10^{-6}$ sec. The combination of the very short time scale and very small amplitude of the thermal fluctuations of emulsion droplets presents an experimental challenge to their observation.

In this chapter we present a detailed study of the thermally induced shape fluctuations of emulsion droplets. We overcome the two major experimental obstacles; we exploit a recently developed purification technique to obtain the requisite monodisperse droplets, and we generalize diffusing-wave spectroscopy (DWS) to probe the minute amplitude of the shape fluctuations. Diffusing-wave spectroscopy extends dynamic light scattering (DLS) to the high multiple scattering limit[9], and probes dynamics on length scales much shorter than the wavelength of the incident light, λ. Several detailed discussions about the theoretical underpinnings of DWS have recently been published[10,11]. To study shape

fluctuations, we generalize the theory of DWS to account for the fluctuations in the scattering amplitude of each droplet that result from the fluctuations in its shape; this generalization can also apply more broadly to other kinds of fluctuations in the scattering amplitude. We analyze the dynamics of thermally excited shape fluctuations using a series expansion in spherical harmonics of shapes that differ only slightly from a sphere. Starting from the surface potential energy governing the dynamics, we compute the amplitudes and relaxation times of thermally induced shape fluctuations controlled by surface tension. The experimental data from DWS measurements are inverted and analyzed with the generalized theory, enabling us to clearly resolve the shape fluctuations. Excellent agreement between our experimental data and theoretical prediction is found in the limit of low droplet volume fraction, ϕ. Moreover, for the data at higher ϕ, a surprising scaling behavior is found enabling the data for all volume fractions over the range of liquid-like emulsions to be collapsed onto the curve predicted for low ϕ. We find that the characteristic decay rate of the shape fluctuations decreases linearly with increasing ϕ, while their amplitude increases. We discuss the possible origin of this behavior. Shape fluctuations persist even in compressed emulsions, i.e., emulsions with ϕ above hard-sphere close-packing values. We give a more qualitative discussion of their behavior.

This chapter is arranged as follows: in the next section, we generalize the theory for DWS by including the consequences of fluctuations of the scattering amplitude in the calculation of the temporal correlation function of the scattered electric field. In Section III, we analyze the scattering amplitude fluctuations that are caused by thermally induced shape fluctuations of particles whose shape is controlled by surface tension. Section IV contains a brief description of the preparation of monodisperse emulsions and the experimental details of the DWS measurements. In Section V, we present our experimental results. The consequences of the interactions between droplets are discussed and a simple model is proposed to attempt to interpret the volume fraction dependence. Concluding remarks are presented in Section VI.

6.2. Diffusing-Wave Spectroscopy with Form Factor Fluctuations

In order to interpret quantitatively any results obtained with a DWS experiment, we must calculate the temporal autocorrelation function of intensity fluctuations of the scattered light. For all DWS experiments this is calculated by dividing the photons into separate, diffusive paths, each containing a large number of scattering events. The probability that a photon will follow a path of length s is determined through the use of the diffusion equation for the light solved for the experimental geometry. The correlation function for each such path is calculated by assuming that the path is comprised of a sequence of $n = s/l$ scattering events, where l is the scattering mean free path. Since n is typically large, each scattering event is assumed to be independent, and thus may be treated as the average scattering event; the average is taken over all possible scattering wave vectors $\mathbf{q}$. To utilize the diffusion approximation for the transport of the light, the number of scattering events must be expressed in terms of the transport mean free path, l^*, the only length scale appropriate for diffusive light. The total correlation function is determined by summing the contributions of all possible paths, weighted by their probabilities. If the positions of the scattering particles in each path are completely uncorrelated, we need to consider only the contributions of individual paths; these can be added, assuming that all interference that contributes to the final signal comes only outside the sample, at the detector. If the scattering from some of the particles is strongly correlated, we need to consider the possible correlations of different scattering particles; this has been done in the case of scattering from solid sphere dispersions[12-15].

All these analyses of the DWS correlation functions assume that the fluctuations arise exclusively from the translational motion of the scatterers. This results in fluctuations of the phase of the light, which are detected through the interference with the light from other paths. To incorporate the effects of shape fluctuations, we must also allow the scattering intensity from each particle to fluctuate; this will result in intensity fluctuations

that occur independently from any phase fluctuations. Thus, the intensity of the light scattered from a suspension of droplets fluctuates not only because of the fluctuating phase interferences among the fields scattered by pairs of droplets as they execute relative translational motions, but also because of the fluctuating amplitude of the field scattered by each individual droplet. The time-dependent amplitudes of the scattered fields reflect the shape fluctuations. To account for these shape fluctuations, we assume that, aside from constants which disappear through later normalization, the field scattered from a liquid droplet can be written as

$$E_i(q,t) = \left[b_i(q) + \Delta b_i(q,t)\right]\exp\left\{i\mathbf{q}\cdot\mathbf{r}_i(t)\right\}. \tag{6.1}$$

Here $\mathbf{q}$ is the scattering wave vector, $\mathbf{r}_i(t)$ is the position of the center of mass of droplet i at time t, $b_i(q)$ is the average field amplitude from an individual scatterer, and $\Delta b_i(q,t)$ is the fluctuating part of the amplitude which depends on the instantaneous geometry of the scatterer.

The contribution from each independent scattering event in a DWS experiment can be expressed in terms of the dynamic structure factor, to reflect the correlations of particles inherent in a concentrated suspension[12-15]. Here we must generalize the expression given there to include the fluctuating portion of the scattering amplitude. Our goal is to obtain an expression for $g_1^n(t)$, the correlation function of the field scattered by a path with n scattering events, where we have re-cast the contribution of the amplitude fluctuations in the same functional form as the contribution of translational motions. This will allow us to adopt directly all the formalism for constructing the full correlation function in terms of the diffusion approximation for the transport of the light. Thus, the autocorrelation function of the scattered field when only single scattering events occur is

$$\left\langle E^*(q,0)E(q,t)\right\rangle = \left\langle \sum_i \sum_j \left[b_i(q) + \Delta b_i(q,0)\right]\left[b_j(q) + \Delta b_j(q,t)\right] e^{i\mathbf{q}\cdot\left[\mathbf{r}_j(t)-\mathbf{r}_i(0)\right]} \right\rangle. \tag{6.2}$$

For monodisperse particles the average scattering amplitudes are the same, so that $b_i(q)= b_j(q)= b(q)$. Furthermore, we assume that the fluctuating scattered amplitude from one drop is uncorrelated with that of other drop, or with the average amplitude. Thus,

$$\left\langle b_i(q)\Delta b_j(q,t)\right\rangle = 0, \tag{6.3a}$$

$$\left\langle \Delta b_i(q,0)\Delta b_j(q,t)\right\rangle = 0, \qquad i \neq j \tag{6.3b}$$

$$\left\langle \Delta b_i(q,0)\Delta b_i(q,t)\right\rangle = \Delta F(q,t), \tag{6.3c}$$

where $\Delta F(q,t)$ is the fluctuating portion of the scatterer form factor. The average form factor is given by

$$F(q) = [b(q)]^2. \tag{6.4}$$

In the absence of fluctuations of the form factor, the correlation function reduces to the familiar form,

$$\left\langle E^*(q,0)E(q,t)\right\rangle = NF(q)S(q,t) \tag{6.5}$$

where the dynamic structure factor is given by

$$S(q,t) = \frac{1}{N}\left\langle \sum_i \sum_j e^{\mathrm{i}\mathbf{q}\cdot\left[\mathbf{r}_j(t)-\mathbf{r}_i(0)\right]} \right\rangle \tag{6.6}$$

where the angular brackets indicate an average over all ensembles of scatterers. In the absence of correlation between particles, the terms with $i \neq j$ do not contribute and Eq. (6.6) reduces to the self-dynamic structure factor,

$$S_s(q,t) = \frac{1}{N}\left\langle \sum_i e^{\mathrm{i}\mathbf{q}\cdot\Delta\mathbf{r}_i(t)} \right\rangle, \tag{6.7}$$

which describes single particle motion.

Including the fluctuations in the form factor, the field correlation function becomes

$$\left\langle E^*(q,0)E(q,t)\right\rangle = NF(q)S(q,t) + N\Delta F(q,t)S_s(q,t), \tag{6.8}$$

where the second term in the autocorrelation function is just the time-dependent part of the scattering form factor multiplied by the *self-dynamic structure factor* and reflects the contribution of the shape fluctuations.

In DWS we measure dynamics on short length scales which typically correspond to short time dynamics. We can therefore approximate the full and self-dynamic structure factors by their behavior at short times. We write[12,14]

$$S(q,t) = S(q)\left[1 - q^2 D_0 \frac{H(q,t)}{S(q)} t\right], \tag{6.9}$$

where $D_0 = k_B T / 6\pi\eta a$ is the self-diffusion coefficient of an isolated sphere of radius a in a fluid of viscosity η, and

$$H(q,t) = \frac{1}{2D_0 t}\left\langle \frac{1}{N}\sum_{i,j=1}^{N} \hat{\mathbf{q}}\cdot\Delta\mathbf{r}_i(t)\hat{\mathbf{q}}\cdot\Delta\mathbf{r}_j(t) e^{i\mathbf{q}\cdot\Delta\mathbf{r}_{ij}} \right\rangle, \tag{6.10}$$

which accounts for the hydrodynamic interactions between the particles. In the absence of correlations, the self dynamic structure factor becomes

$$S_s(q,t) = 1 - \frac{q^2}{6}\left\langle \Delta r^2(t) \right\rangle, \tag{6.11}$$

reflecting the mean square displacement of the particles. To obtain the average single-scattering correlation function required for the construction of the DWS correlation function, we must average Eq.(6.8) over all possible angles. We transform the average over angles into an integral over $\mathbf{q}$, obtaining

$$\left\langle E^*(q,0)E(q,t)\right\rangle_q = N\left[\int F(q)S(q)qdq - \int q^3 F(q)H(q)dqD_0 t + \int \Delta F(q,t)qdq\right], \tag{6.12}$$

where we have ignored the second order small quantity, $\frac{q^2}{6}\Delta r^2(t)\cdot\Delta F(q,t)$, with the assumption $\Delta F(q,t) \ll F(q)$. To calculate $g_1''(t)$, the contribution to the DWS correlation function from a path with n scattering events, we assume that each scattering

event is independent and take the product of n q-averaged single-scattering correlation functions and normalize by the value at $t = 0$,

$$g_1^n(t) = \frac{\left\langle E^*(q,0)E(q,t)\right\rangle_q^n}{\left\langle E^*(q,0)E(q,0)\right\rangle_q^n}. \tag{6.13}$$

Keeping only the first order terms,

$$g_1^n(t) = 1 - n\frac{\int q^3 F(q)H(q,t)dq}{\int qF(q)S(q)dq} D_0 t - n\frac{\int qF(q,0)dq - \int qF(q,t)dq}{\int qF(q)S(q)dq}, \tag{6.14}$$

where $S(q)$ is the static structure factor, or $S(q,t)$ evaluated at $t = 0$. Eq.(6.14) can be approximated as

$$g_1^n(t) = \exp\left\{-n\frac{\int q^3 F(q)H(q,t)dq}{\int F(q)S(q)qdq} D_0 t - n\frac{\int \Delta F(q,0)qdq - \int \Delta F(q,t)qdq}{\int F(q)S(q)qdq}\right\}, \tag{6.15}$$

since $\int q^3 F(q)H(q,t)dqD_0 t$, $\int \Delta F(q,t)qdq \ll \int F(q)S(q)qdq$. This approximation expresses the q-averaged, n-event scattering field correlation function as the exponential of a time-dependent function. This is the same form that arises in the treatment of systems that have only translational dynamics. Thus we have incorporated amplitude fluctuations in the desired form.

To use the diffusion approximation for light propagation through the medium, we describe the diffusive step length l of the diffusing light in terms the transport mean free path l^*, which is defined by[16]

$$\frac{l^*}{l} = \frac{2k_0^2 \int qF(q)S(q)dq}{\int q^3 F(q)S(q)dq}, \tag{6.16}$$

where k_0 is the wave number of the light in the continuous phase of the emulsion. The number of scattering events can then be expressed in terms of the path length normalized

by the transport mean free path, $n = \frac{s}{l^*}\left(\frac{l^*}{l}\right)$ where Eq.(6.16) is used for the factor in the parentheses. We introduce the following notation

$$[S] = \frac{\int q^3 F(q) S(q) dq}{\int q^3 F(q) dq}, \tag{6.17}$$

which is the structure factor as averaged in a DWS experiment, and

$$[H] = \frac{\int q^3 F(q) H(q,t) dq}{\int q^3 F(q) dq}, \tag{6.18}$$

which is the similarly averaged hydrodynamic interaction factor. We note here that the DWS average includes a weighting by $q^3 F(q)$ and strongly emphasizes the high-q region of both $S(q)$ and $H(q,t)$.

The averaging of DWS also modifies the effects of the shape fluctuations. The equilibrium total cross section is defined as the q-averaged form factor,

$$\sigma_0 = \int F(q) q dq, \tag{6.19}$$

while

$$\Delta\sigma(t) = \int \Delta F(q,t) q dq \tag{6.20}$$

defines the time-dependent total cross section deviation function as the q-averaged autocorrelation of the fluctuating portion of the scattering amplitude.

Introducing these definitions into Eq.(6.15), we express the correlation function for the field scattered from a path of length s as

$$g_1^s(t) = \exp\left\{-\frac{2k_0^2 s}{l^*[S]}\left[[H] D_0 t + \frac{l_0^*}{2k_0^2 l_0}\frac{\Delta\sigma(0) - \Delta\sigma(t)}{\sigma_0}\right]\right\}. \tag{6.21}$$

The first term in the exponent is identical to the expression obtained in the absence of amplitude fluctuations, while the second term reflects the effects of the amplitude

fluctuations. The quantity l_0^*/l_0 is defined by Eq.(6.16) with $S(q)$ set equal to one. It may be interpreted as the ratio of the transport and scattering mean free paths for light diffusing through a suspension of scatterers among which there are no spatial correlations, and reflects our assumption that the shape fluctuations of one droplet are uncorrelated with those of any other droplet. Thus, the shape fluctuations result in a contribution to the correlation function that adds to the contribution of translational motions. The shape fluctuation contribution increases from zero and saturates at a value proportional to $\Delta\sigma(0)/\sigma_0$, reflecting the relaxation of deformed shapes. Because the shape fluctuation contribution is additive, it competes with the contribution of translational motion; as a result, it should be observable only if shape deformations relax in less time than is required for significant translational motions. The full DWS correlation function is obtained by summing over all paths, weighted by the probability, $P(s)$, that a photon follows a path of lengths s:

$$g_1(t) = \int P(s) \exp\left\{ -\frac{2k_0^2 s}{l^*[S]} \left[[H] D_0 t + \frac{l_0^*}{2k_0^2 l_0} \frac{\Delta\sigma(0) - \Delta\sigma(t)}{\sigma_0} \right] \right\} ds. \qquad (6.22)$$

We note that the autocorrelation function resembles the Laplace transform of the probability distribution function $P(s)$. The quantity $P(s)$ depends explicitly on the shape and illumination of the scattering cell. We determine it for any given experimental geometry by solving the diffusion equation with appropriate boundary conditions[9,11]. The transport mean free path $l^*$and the DWS-averaged structure factor $[S]$ can also be measured or calculated independent of the measurement of $g_1(t)$. The right side of Eq.(6.22) is therefore a known function of the quantity in square brackets. From a tabulation of this function and the measured value of g_1 at a given time t, we are thus able to obtain the value of the quantity in square brackets at time t. We refer to this procedure as the inversion of the DWS correlation function; this inversion is unrelated to Laplace transform inversion. The first term in the square bracket describes the contribution to the

correlation decay from the apparent diffusion. Collective effects in these translational motions are described by $[H]$. For the case of relatively large particles satisfying $R \geq \lambda$, the high-q weighting of the DWS averages allows us to approximate $[H]D_0 t$ as $\langle \Delta r^2(t) \rangle / 6$. In this case DWS probes the mean square displacement $\langle \Delta r^2(t) \rangle$[11]. The second term contains the effects of the amplitude fluctuations. Its prefactor l_0^*/l_0 must be evaluated in the limit of zero volume fraction and has no volume fraction dependence. It is clear from Eq.(6.22) that DWS probes the relative fluctuations of the cross section. Like $\langle \Delta r^2(t) \rangle$, their contribution to the decay of $g_1(t)$ increases from zero at $t = 0$, but it saturates at long times, while $\langle \Delta r^2(t) \rangle$ and its contribution continues to increase. It is also clear why very small motions can be detected with DWS: for long paths, $s/l^* \gg 1$; this large factor in Eq.(6.22) allows small values of the quantity in the square brackets to contribute to the decay of $g_1(t)$. The signal arises from the sum of a large number of independent amplitude fluctuations. They would not be detectable without the advantage of multiple scattering.

We note that the derivation is independent of the nature of the amplitude fluctuations; not only shape fluctuations but other phenomena, such as rotational motion of aspherical particles, can also result in a similar contribution.

6.3. Dynamics of Shape Fluctuations of Emulsion Droplets

The fluctuations in the shape of an emulsion droplet result from capillary waves on its interface. Their amplitudes are determined by the thermal energy which excites them and by the interfacial tension, Γ, which controls them. A change in shape results in an increase of the interfacial area, ΔA, and therefore an increase of the surface potential energy. Since the fluids are incompressible, the droplet volume remains fixed, and a change in surface area results in a change in shape. The thermal energy $k_B T$ is much less than the total surface potential energy ΓR^2, so $k_B T \approx \Gamma \Delta R^2 \ll \Gamma R^2$. We must calculate the fluctuating shape of the droplets due to the thermally excited capillary waves, and the scattering cross section of this fluctuating shape.

To calculate the fluctuating shape, we express the surface potential energy as a sum of spherical harmonics and use the equipartition theorem to assign each mode an energy of $k_B T/2$. Because of thermal excitation, the liquid drop has at any instant a non-spherical shape. The surface potential energy, E, can be written as

$$E = \Gamma A = \Gamma \int_0^{\pi} \int_0^{2\pi} \left[r^2 + \frac{1}{2}\left(\frac{\partial r}{\partial \theta}\right)^2 + \frac{1}{2\sin^2\theta}\left(\frac{\partial r}{\partial \varphi}\right)^2 \right] \sin\theta \, d\theta \, d\varphi, \tag{6.23}$$

where we take the surface tension, Γ, as a constant, by assuming the fluctuating amplitude is small so that the effect of surface dilation on Γ is negligible. Here A is the surface area of the distorted sphere and $r(\theta,\varphi,t)$ is its instantaneous radius as a function of polar angles θ and φ. We expand $r(\theta,\varphi,t)$ in a series of spherical harmonics, $Y_{lm}(\theta,\varphi)$ [5,6,17],

$$r(\theta,\varphi,t) = r_0 \left(1 + \sum_{l=2}^{l_{\max}} \sum_{m=-l}^{m=l} a_{lm}(t) Y_{lm}(\theta,\varphi) \right), \tag{6.24}$$

where $l = 0$, $l = 1$ are excluded because they represent a dilation and translation of the drop, and where r_0 is the zeroth order term in the expansion. Thus, the surface energy is

$$E = 4\pi\Gamma r_0^2\left(1+\frac{1}{8\pi}\sum_{l=2}^{l_{\max}}\sum_{m=-l}^{m=l}(-1)^m\left[l(l+1)+2\right]a_{lm}a_{l,-m}\right). \tag{6.25}$$

Since the volume is conserved,

$$\frac{4\pi}{3}R^3 = \iint\frac{1}{3}\left[r(\theta,\varphi)\right]^3\sin\theta d\theta d\varphi, \tag{6.26}$$

where R is the radius of the undistorted spherical droplet. Neglecting higher-order terms, we can determine the first order term, using the constraint of Eq.(6.26),

$$r_0 = R\left(1-\frac{1}{4\pi}\sum_{l=2}^{}\sum_{m=-l}^{m=l}a_{lm}a_{l,-m}(-1)^m\right). \tag{6.27}$$

Then, the expression for the potential energy becomes

$$E = 4\pi\Gamma R^2\left(1+\frac{1}{8\pi}\sum_{l=2}^{l_{\max}}\sum_{m=-l}^{m=l}\left[l(l+1)-2\right]\left|a_{lm}\right|^2\right). \tag{6.28}$$

Here we have an excess surface free energy because of shape fluctuations. According to the equipartition principle, we take the ensemble average of Eq.(6.28) and give each mode an energy of $\frac{1}{2}k_BT$ to obtain the mean square amplitude of each mode,

$$\left\langle\left|a_{lm}\right|^2\right\rangle = \frac{k_BT}{\Gamma R^2}\frac{1}{l(l+1)-2}. \tag{6.29}$$

In the case of an emulsion system, the shape fluctuations for each mode take place at low Reynolds number, where convective and inertial terms in the Navier-Stokes equations can be neglected[18]. The differences in the normal components of the viscous stresses are balanced by the Laplace pressure of the deformed surface and the fluid velocities are continuous. These boundary conditions determine the relaxation of the deformed droplet to spherical shape. Thus, in this overdamped limit, the autocorrelation function of the fluctuating amplitude is given by

$$\left\langle a_{lm}^*(0)a_{l'm'}(t)\right\rangle = \frac{k_BT}{\Gamma R^2}\frac{\delta_{ll'}\delta_{mm'}}{l(l+1)-2}e^{-\omega_l t}, \tag{6.30}$$

where the decay rate for modes l is given by [19]

$$\omega_l = \frac{l(l+2)(2l+1)}{2(2l^2+4l+3)}\frac{\Gamma}{\eta R}. \tag{6.31}$$

In general, ω_l depends on the viscosities of both fluids[20]; we have assumed that the viscosity η of the interior is much greater than that of the surrounding fluid. We note that asymptotically $\omega_l \sim l$, reflecting the fact that the dynamics are controlled by surface tension; by contrast, $\omega_l \sim l^3$ when the dynamics are controlled by the interfacial rigidity[17].

To calculate the far field scattering amplitude from these shape fluctuations, $b(q,t)$, we should use the exact Mie scattering theory[21], suitably generalized to treat non-spherical scatterers. But as a first approximation, we restrict the calculation to the dipole contribution, using the Rayleigh-Gans (RG) approximation[21]. We recognize that this is not strictly correct, and test the errors introduced by this approximation later. The instantaneous scattering amplitude $b(q,t)$ can be expressed as:

$$b(q,t) = \frac{1}{V}\int_V e^{i\mathbf{q}\cdot\rho'} d^3\rho' \tag{6.32}$$

where $\mathbf{q}$ is the scattering vector, V is the volume of the scatterer, and the integration vector ρ' connects the origin with a point inside the scatterer. The upper limit $\rho_{\max}$ for its magnitude is just the instantaneous, direction-dependent radius of the droplet, which we express as a series expansion of spherical harmonics

$$\rho_{\max}(\theta,\varphi) = R\left(1 + \sum_{l=2}^{l=l_{\max}} \sum_{m=l}^{m=-l} a_{lm} Y_{lm}(\theta,\varphi)\right), \tag{6.33}$$

where we now neglect the distinction between R and r_0 and a_{lm} are expansion coefficients whose autocorrelators have been determined in Eq.(6.30).

The plane wave in Eq.(6.32) can also be expressed as a series expansion:

$$e^{iq\rho'\cos\gamma} = \sum_{l=0}^{\infty}(2l+1)i^l j_l(q\rho')P_l(\cos\gamma), \tag{6.34}$$

where $j_l(q\rho')$ and $P_l(\cos\gamma)$ are the l^{th}-order spherical Bessel function and Legendre polynomial, and γ is the angle between the scattering vector **q** and the integration vector ρ'. Completing the integration of Eq.(6.32), we arrive at the time-dependent form factor $F(q,t)$ which is the autocorrelation function of the scattering amplitude[5]:

$$F(q,t) = \langle b^*(q,0)b(q,t)\rangle = \left(\frac{3j_1(qR)}{qR}\right)^2 + \frac{1}{4\pi}\sum_{l=2}(2l+1)(3j_l(qR))^2\langle a_l^*(0)a_l(t)\rangle. \tag{6.35}$$

A DWS experiment probes the q-averaged form factor. Thus, we integrate Eq.(6.35) over q, obtaining the total scattering cross section, apart from a constant prefactor depending on the relative refractive index which we may omit since it cancels with normalization. The cross section consists of the constant part, σ_0, and the time-dependent part, $\Delta\sigma(t)$, defined previously by Eqs.(6.19) and (6.20). Within the RG approximation, the explicit expressions are

$$\sigma_0 = \pi\int_0^{\pi}(1+\cos^2\theta)\left(\frac{3j_1(qR)}{qR}\right)^2\sin\theta d\theta \tag{6.36}$$

and

$$\Delta\sigma(t) = \frac{k_B T}{4\pi\Gamma R^2}\sum_{l=2}\frac{2l+1}{l(l+1)-2}g_l\exp(-\omega_l t), \tag{6.37}$$

where g_l is given by

$$g_l = \pi\int_0^{\pi}(1+\cos^2\theta)(3j_l(qR))^2\sin\theta d\theta. \tag{6.38}$$

In Eqs.(6.36) and (6.37), the scattering wave number is $q = 2k_0\sin(\theta/2)$, where k_0 is the wave number of the incident radiation in the continuous phase of the emulsion. The factor $1+\cos^2\theta$ is appropriate for an unpolarized incident beam[21] and reflects the effect that multiply scattered light is completely depolarized. The coefficients g_l depend only on k_0R and express the scattering efficiency of each deformation mode. They become negligible

when $l \gg k_0 R$, since the length scale of the features described by such modes is much smaller than the wavelength of the radiation. This behavior of g_l makes the assignment of a cut-off mode number unnecessary in Eq.(6.37), although such a cut-off l_{max} is required in Eq.(6.25) to avoid a logarithmic divergence of the surface energy E. Thus, for a given droplet size and laser wavelength, only a finite number of modes contribute to the scattering. For example, we find that the series converges for $l \approx 20$ for a 1.4 μm diameter droplet and $k_0 = 16.3 \mu m^{-1}$.

Because of the large refractive index mismatch, Δn, between oil and water, the criterion $\Delta n k_0 R \ll 1$ for the validity of the Rayleigh-Gans approximation does not strictly hold for an emulsion droplet. Nevertheless, it appears that the RG theory is sufficiently accurate to describe our system. We arrive at this conclusion by calculating with the Mie theory the exact form factor of an undeformed sphere and comparing the result with that found from the RG theory. Thus, a calculation of the constant part of the total cross section in absolute units yields σ_0 = 0.995 μm^2 from Mie theory and 0.999 μm^2 from RG theory. Moreover, we also use the exact calculation for spheres in an ad hoc procedure that tests the accuracy with which the RG theory determines the scattering power of non-spherical shapes. To accomplish this, we use identities satisfied by Bessel functions to re-write Eq.(6.38) for the dominant coefficient g_2, which describes the scattering from ellipsoidal deformations, in terms of the derivative with respect to qR of the form factor of an undeformed sphere. We then use the Mie theory to evaluate this form factor and its derivative exactly. We find that the values obtained by this method and by direct evaluation of Eq.(6.38) agree to about 10%, the value directly predicted by the RG theory being the lower of the two. Thus we conclude that applying the RG theory to our scattering measurements allows us to infer the essential behavior of shape fluctuations, with an uncertainty of about 10%. Hereafter, we use the Rayleigh-Gans approximation exclusively, since it allows us to directly evaluate the contribution to the correlation function due to shape fluctuations through Eqs.(6.31) and (6.36)-(6.38).

6.4. Experimental Method

Our emulsion samples are three component suspensions consisting of dispersed oil, continuous water, and SDS (sodium dodecylsulfate) surfactant on the interfaces. The SDS surfactant molecules play two roles in the emulsification process. First, they lower the interfacial tension and thereby make it easy to create small droplets. Second, they stabilize the dispersed droplets against coalescence once they are formed. Mechanical energy is added to the three-component system by mixing oil, water and surfactant with a Kitchen Aid mixer. The ratio of the three components is adjusted to facilitate the formation of emulsions. The peak of the size distribution of the emulsion droplets can be controlled by varying the mixing time and the shear rate exerted by the mixer. Crude emulsions with droplet sizes ranging from 0.1 μm to 2 μm are first prepared in highly concentrated form. The polydisperse emulsions are purified with the technique of fractionated crystallization, which is based on the liquid-solid phase transition induced by the attractive depletion interaction. The attractive interaction between the droplets arises from the non-compensated pressure exerted by surfactant micelles in the suspension. The detailed purification principles have been summarized in the literature[22]. By adjusting the micelle concentration we obtain highly monodisperse emulsions after eight steps of the purification process. The polydispersity is about 6% of the average radius, and is sufficiently low that the samples form colloidal crystals, analogous to hard-sphere dispersions at appropriate volume fractions[23]. Because the droplets are deformable, their volume fraction can be increased to well above hard sphere close packing values. This is accomplished by putting the emulsion in a dialysis bag, which is immersed in a large reservoir containing water, SDS, and a hydrophilic polymer, dextran, with molecular weight (MW) of 500,000. Dextran is chosen because the osmotic pressure and surfactant chemical potential can be independently controlled in a SDS-dextran water mixture by varying the polymer concentration and surfactant concentration. The dialysis bag is made

of a cellulosic membrane with a MW cutoff of 50,000. It is permeable to water and surfactant, but impermeable to the oil droplets and polymer. Thus, taking advantage of the osmotic pressure, we can increase the volume fraction by pumping the excess water out of the bag. Then the volume fraction is measured directly by weighing a portion of sample before and after drying in a vacuum oven, maintained at room temperature. The weight fractions are converted to volume fractions under the assumption that the density of the droplets is the same as the density of the bulk oil. This enables us to study the effects of the volume fraction of the droplets on their shape fluctuations.

The standard experimental setup for DWS in transmission is used[15]. The beam from an Ar^+ laser is focused on one side of the sample cell containing the emulsion, and scattered light is collected from the other side. The Ar^+ laser operates in a single longitudinal mode at a wavelength of 514.5 nm in vacuum. Single mode operation is essential because our detection system is sufficiently fast to be able to detect the beats between neighboring longitudinal modes of the laser, which occur at 125 MHz. Moreover, operating in a single mode ensures that the coherence length of the light is larger than the longest diffusive light paths in the sample.

To enable us to study the very fast phenomena of interest, we use a cross-correlation technique. The scattered light is divided into two equal portions and is detected with two photomultiplier tubes (PMT). The outputs of these are cross-correlated. This method reduces the deleterious effects of afterpulsing in the individual PMT's, which otherwise introduce a spurious correlation at short times. The cross-correlation technique also reduces the effects of dead times in the PMT's and counting electronics, and, provided that the count rate in each tube is not too large, allows measurements at faster time scales.

Our detection optics are optical fibers. We use two different types, single mode and multi-mode. In both cases, the beam splitter is integrated into the fibers, greatly simplifying the alignment. The multimode fiber has a core diameter of 100 μm, and standard two-pinhole optics are used to collect the light. A lens is used to image the fiber

face onto the face of the sample and an aperture at the lens is adjusted to limit the range of scattering vectors collected by the fiber core, which serves as the second pinhole. In the case of a single mode fiber, the light is collected by a graded index (GRIN) lens of 0.25 pitch, which is integrated on the fiber cable. The single mode fiber collects only the light incident on the face of the GRIN lens which is of a single spatial mode. This arrangement results in a much higher spatial coherence factor, while maintaining a high light-collecting efficiency[24]. Moreover, the single mode fiber receiver offers the possibility of working with an arbitrarily large scattering volume and with an arbitrary working distance.

Like all forms of dynamic light scattering, a DWS experiment measures the temporal autocorrelation function of the fluctuations of the scattered light intensity. The intensity correlation function is related to the field correlation function through the Siegert relationship,

$$g_2(t) = 1 + \beta|g_1(t)|^2. \tag{6.39}$$

The spatial coherence factor β depends on the number of coherence areas detected by the optics.

The scattering system here consists of liquid oil droplets dispersed in water. The average radius of the oil droplets is R = 0.7 μm. The polydispersity (normalized rms radius deviation) is about 6%. The index of refraction of the oil is 1.401; since the refractive index of water n is 1.33, the system scatters light very strongly. With the volume fraction above 5% and the sample cell thickness of 4 mm, the high multiple scattering limit can easily be reached in the transmission geometry. Similar emulsions were prepared from oils of two different viscosities, $\eta = 12$ cP and $\eta = 1000$ cP.

6.5. Experimental Results

A typical autocorrelation function from the emulsion with the 12 cP oil is shown in Fig. 6.1. The data are obtained using an emulsion with $\phi = 0.35$, and they have been

normalized with the background subtracted, so that we plot $|g_1(t)|^2$. Only the initial decay is shown, to emphasize the deviation of the data from the behavior expected for a suspension of solid spheres at the same volume fraction. The behavior expected for hard spheres can be predicted from the measured scaling form[15], and is shown by the solid line. The data clearly deviate from the expected behavior; similar deviation is observed at all volume fractions. By contrast, the correlation function from an identical emulsion made from 1000 cP oil does agree very well with the prediction for solid spheres, as shown in Fig. 6.2. Moreover, similar good agreement is observed for initial decay of the correlation function for all volume fractions of this emulsion up to $\phi = 0.45$.

The origin of the discrepancy is the fluctuations in the shape of the emulsion droplets. Their relaxation rate scales with the viscosity of oil; for droplets with higher viscosity, this relaxation rate is so slow that the decay of the correlation function is dominated by the translational motion of the droplets, so the shape fluctuations cannot be distinguished. By contrast, for the droplets with the low viscosity, the shape fluctuations relax sufficiently rapidly that they can be clearly distinguished from the translational motion of the droplets.

To analyze the dynamics of the shape fluctuations, we invert the DWS intensity autocorrelation function as described in Section II and so obtain the quantity appearing in square brackets in Eq.(6.22). To set the absolute level of these data, we need to know the transport mean free path, l^*, and the DWS averaged structure factor, $[S]$. We evaluate $[S]$ from its definition (Eq.(6.17)), using the Mie theory to calculate the scattering form factor $F(q)$ and the expression for the total static structure factor for hard spheres, $S(q,\phi)$, that is obtained with the Percus-Yevick approximation[25]. The value of l^* can, in principle, be obtained by two independent methods. It can be calculated from the Mie scattering theory with particle correlations taken into account through the use of a theoretical structure factor[16]. Alternatively, we can determine it experimentally by measuring the static transmission through the sample[9]. The static transmission is proportional to l^*; by comparing the measured transmission with that of a reference sample

of identical thickness, and in the same optical configuration, we obtain the value of l^* relative to that of the reference sample. By using as a reference sample a hard sphere suspension of relatively low volume fraction, we ensure that the reference value of l^* can be calculated with reasonable accuracy. Comparing the values we obtain for l^* using these two methods, we assign a 10 % experimental uncertainty to the inverted correlation functions.

The inverted data for the two emulsions are plotted in Figure 6.3, with open symbols used for the emulsion of 1000 cP oil and solid symbols used for the emulsion of 12 cP oil. The data consist of a sum of a contribution due to the translational portion, and another contribution due to the relaxation of the amplitude fluctuations $\left(\Delta\sigma(0)-\Delta\sigma(t)\right)/\sigma_0$. Since the droplets are relatively large, the translational contribution is given directly by the mean square displacement, $\left\langle \Delta r^2(t)\right\rangle$. As illustrated in Fig. 6.3, for the emulsion made of the high viscosity oil, the inverted data follow the curve predicted for solid spheres, shown by the solid line. In this case, the theory includes only the self-translational portion $\left\langle \Delta r^2(t)\right\rangle$, but incorporates the consequences of hydrodynamic interactions[15]. As probed by dynamic light scattering, the emulsion of the high viscosity oil is indistinguishable from a suspension of rigid spheres because here large translational displacements occur during the much longer relaxation time for shape fluctuations. The contribution from the shape fluctuations is therefore negligible in comparison with the contribution from translations. By contrast, an emulsion made of the lower viscosity oil exhibits distinct additional dynamics, shown by the solid circles in Fig. 6.3. At early times these data fall significantly above those of the heavy oil and those expected for solid spheres; at later times the data merge with the purely translational dynamics.

To investigate the relaxation of shape fluctuations more clearly, we separate the contributions of translational motion and shape fluctuations by subtracting the mean square displacement from the inverted data. We can do this subtraction because the mean square displacement can be calculated accurately: the pre-diffusional Brownian motion of

an isolated particle has been calculated theoretically[26], while measurements performed on rigid hard spheres have established a scaling of the theory with volume fraction that accounts for interactions[13-15]. We plot $R^2\Delta\sigma(t)/\sigma_0$ for $\phi = 0.35$ on a log-linear scale in Figure 6.4; we multiply the normalized cross section deviation function $\Delta\sigma(t)/\sigma_0$ by R^2 since by doing so we obtain a quantity closely related to the autocorrelation function of fluctuations of the droplet radius. To establish this connection, we introduce here the radius correlation function of a fluctuating droplet using Eqs.(6.24) and (6.30),

$$\frac{1}{4\pi}\int\langle(r(0)-R)(r(t)-R)\rangle d\Omega = \frac{k_BT}{4\pi\Gamma}\sum_{l=2}^{l_{max}}\frac{2l+1}{l(l+1)-2}\exp(-\omega_l t). \qquad (40)$$

Comparing Eqs.(6.37) and (6.40), we see that the difference between the radius correlation function and $R^2\Delta\sigma(t)/\sigma_0$ is just the appearance in the latter of the coefficients g_l/σ_0 which characterize the scattering strength of each deformation mode relative to the scattering strength of the undeformed sphere. Hereafter we will call $R^2\Delta\sigma(t)/\sigma_0$ the shape fluctuation correlation function. It is the radius correlation function when the contributions of the deformation modes are taken with an intensity weighting.

The curves shown in Fig. 6.4 have been calculated from Eqs.(6.36-8) together with overall re-scalings of the amplitude and time scale, to be described below. For the dashed curve, we include only the first term, $l = 2$, in the sum over deformation modes, resulting in a purely exponential decay. Comparison of this curve with the data makes evident the distinctly non-exponential relaxation of shape fluctuations. However, we obtain excellent agreement with the data when we include more modes, up to $l_{max} = 17$ (solid line). In a practical sense, the mode sum converges and the computed curve is insensitive to the value of l_{max} provided it is chosen larger than 10. On the other hand, the fit to the data is noticeable poorer if we choose $l_{max} = 5$ or less, indicating that higher order deformation modes contribute significantly.

In Fig. 6.5 we show logarithmic plots of the shape fluctuation correlation functions $R^2\,\Delta\sigma(t)/\sigma_0$ measured with emulsions whose droplet volume fractions cover the range $0.07<\phi<0.55$. The amplitudes of the shape fluctuations increase with ϕ. Fig. 6.5 also shows the shape fluctuation correlation function of an isolated droplet as predicted by the theory without adjustments of any kind. The data appear to fall on curves which differ from the theoretical curve only by ϕ-dependent vertical and horizontal shifts. This surprising scaling behavior indicates that the relative strength and relaxation rates of the deformation modes of interacting droplets are the same as those of an isolated droplet. To test this suggestion, for each data set we scale the theoretical curve by treating as ϕ-dependent two fitting parameters. These are the amplitude of the correlation function, $R^2\,\Delta\sigma(t=0;\phi)/\sigma_0$, and the overall factor, $\omega(\phi)$, that applies to the l-dependent mode relaxation rates ω_l. By comparison, the prediction of the theory for these parameters, for $\phi=0$, is

$$\frac{R^2\Delta\sigma(t=0;\phi=0)}{\sigma_0}=\frac{k_BT}{4\pi\Gamma\sigma_0}\sum_{l=2}g_l\frac{2l+1}{l(l+1)-2}=52\,\text{Å}^2 \tag{41}$$

and

$$\omega(\phi=0)=\frac{\Gamma}{\eta R}=1.2\text{x}10^6\text{sec}^{-1}. \tag{42}$$

In Figure 6.6 we plot the measured and theoretical shape fluctuation correlation functions, normalized by their fitted amplitudes to the theoretical amplitude of 52 Å^2, versus scaled time $\omega(\phi)t$. All the data do indeed collapse onto a single master curve. Furthermore, the measured data approach the theoretical curve given in Eqs.(36-8) as ϕ approaches zero: the extrapolation of the fitted $\omega(\phi)$ to $\phi=0$ gives a value identical to the predicted value of $1.2\text{x}10^6\text{sec}^{-1}$. Similarly the extrapolated value of the amplitude $R^2\Delta\sigma(t=0;\phi=0)/\sigma_0$ is 70 Å^2. The discrepancy with the predicted value 52 Å^2 may reflect the error introduced by the Rayleigh-Gans approximation, the error in our values for the scattering and transport mean free paths l and l^*, or the error incurred by our

simple linear extrapolation of the amplitude-volume fraction relation defined by our two least concentrated samples.

To examine the ϕ-dependence of shape fluctuations, we plot in Fig. 6.7 the relaxation rate scaling function, $\omega(\phi)$, normalized by its theoretical value at $\phi = 0$, 1.2×10^6 sec^{-1}. The normalized scaling function is well represented by $\omega(\phi)/\omega(0) = 1 - 0.78\phi$. The ϕ-dependence is relatively weak in the sense that there is no sign of the shape deformation relaxation rate extrapolating to zero as the volume fraction increases toward $\phi \approx 0.63$, the value of random close packing of spheres, which is the limiting value for packing undeformed spheres; above this value, the droplets must be permanently deformed in order to pack together. The ϕ-dependence is also linear, despite the high concentrations. Nevertheless, the behavior of the relaxation rate may be indirectly related to the ϕ-dependence of the effective viscosity of the emulsion, even though the latter is strongly non-linear over the volume fraction range our measurements cover. A similar linear form for the shape relaxation rate was recently predicted for the $l = 2$ modes as part of a theory for the non-linear ϕ-dependence of the effective viscosity of a non-dilute suspension of deformable droplets[27]. The predicted coefficient was 1.4, larger than the value 0.78 which we obtain; however this theory was restricted to the case of equal viscosities of the oil and water. In our experimental system, the droplet viscosity is an order of magnitude higher than the viscosity of the solvent. Since under these conditions the relaxation rate of the shape fluctuations of an isolated droplet is less sensitive to the viscosity of the solvent, it is plausible that the effects of the solvent-mediated interactions considered by the theory are less effective as well.

The ϕ-dependence of the amplitude of the fluctuations exhibits different behavior. We show this in Fig. 6.8, where we plot the shape correlation function amplitude, $R^2 \Delta\sigma(t = 0; \phi)/\sigma_0$, normalized by the theoretical value at $\phi = 0$, 52 Å^2. We designate the normalized amplitude more completely by $\Delta\sigma(\phi)/\Delta\sigma(0)$. The data increase sharply, by a factor of about two at higher volume fractions. This increase in the amplitude of the shape

fluctuations with ϕ is very surprising. It suggests that the energy driving shape fluctuations increases as ϕ increases. A possible source for this extra energy is the energy of translational motion, which may couple to shape fluctuations through collisions of the droplets. According to this view, we attribute the strong non-linear increase of the amplitude of shape fluctuations to the rapid increase of the frequency of collisions as the system becomes denser. The probability of two droplets colliding should scale with the number of pairs of droplets touching one another, which is given by $\phi g(2,\phi)$, where $g(2,\phi)$ is the pair correlation function evaluated at the contact distance, $2R$. This suggests a functional form for the normalized shape fluctuation amplitude $\Delta\sigma(\phi)/\Delta\sigma(0) = 1+C\phi g(2,\phi)$. The expression assigns extra deformation to those droplets that are in contact with one or more neighbors; the fraction these colliding drops make out of the total number of drops is proportional to $\phi g(2,\phi)$. We treat C as adjustable and use the Carnahan-Starling equation of state for hard spheres, $g(2,\phi) = (1-\phi/2)/(1-\phi)^3$ [28]. The fit with C=0.2 is shown in Fig. 8 as the smooth curve. We obtain good agreement with the measured shape-fluctuation amplitudes. We emphasize, however, that while this model gives reasonable agreement with data, it is nevertheless only a crude approximation. In particular, very recent work by Cai suggests that our expression is fundamentally wrong at low volume fraction[29]. Thus whereas our expression gives C as the coefficient for the linear term in an expansion of $\Delta\sigma(\phi)/\Delta\sigma(0)$ in powers of ϕ, Cai's analytic calculation of this first coefficient gives $3k_BT/2\pi\Gamma R^2 \approx 4\text{x}10^{-7}$. At higher ϕ, however, our data and our model expression do agree qualitatively with Cai's 2D simulation of droplet shape fluctuations. Another possibility is that the shapes of neighboring droplets may fluctuate in a correlated way at higher ϕ. In that case, the measured $\Delta\sigma(\phi)/\Delta\sigma(0)$ may reflect the effects of spatially correlated amplitude fluctuations whose existence was ignored in deriving Eq.(6.22). Alternatively it is also possible that the translational motion of the liquid droplets differs in some way from that of hard spheres, contrary to what we

assumed in isolating the contribution of the shape fluctuations. This could also have the effect of modifying the measured amplitude at higher ϕ.

All of the data discussed to this point involved emulsions whose volume fractions were well below the limit of random close packing, and thus possessed liquid-like translational dynamics. However, since droplets are deformable, we can prepare emulsions with much higher volume fractions; then their translational motion is arrested, much like a colloidal glass. Nevertheless, we continue to see in DWS measurements an early decay on a time scale that seems to evolve continuously from the time scale of the shape fluctuations of droplets in less concentrated emulsions. We illustrate this behavior in Fig. 6.9, where we plot the inverted correlation functions for a series of volume fractions of the emulsion made from the oil with the lower viscosity of 12 cP. At low volume fractions, the shape fluctuations are clearly distinguished from the translational motion as an early-time region of lower slope on the logarithmic plots of the inverted correlation functions. Here, the translational motion persists after the shape fluctuations have decayed, reflecting the diffusive motion of the droplets. By contrast, as ϕ is increased, the translational motion is depressed at longer times; for $\phi = 0.65$ and above, it is fully arrested, suggesting that all the remaining dynamics result solely from the shape fluctuations. We cannot give a full analysis of these measurements. A starting point for understanding compressed emulsions, however, is furnished by the example of the colloidal glass of rigid spheres[30]. At and above the glass transition, this system becomes non-ergodic, so that the decay of the properly averaged autocorrelation function saturates at a finite value[31]. The cause of this saturation is the arrest of translational motions: particles do not execute displacements past some maximum value. Therefore, in compressed emulsions, shape fluctuations can remain significant in comparison with translations for longer times. In fact, when the translational motion is completely arrested at high ϕ, even the more slowly relaxing shape fluctuations of droplets of high viscosity oils can be resolved. Thus, we can obtain some idea of the separate contributions of shape

fluctuations and translations to the dynamics of compressed emulsions by studying the effect of the oil viscosity. Shown in Figure 6.10 are the measured intensity autocorrelation functions obtained from two emulsions with $\phi = 80\%$. The solid symbols are the data for an emulsion of 12 cP oil, while the open symbols are for one of 1000 cP oil. Both sets of data exhibit a decay to the same absolute level, but the characteristic times are markedly different. Although only the initial decay is shown in Fig. 6.10, at longer times, both sets of data decay fully, presumably due to slow relaxations of droplet configurations. Thus, the measured correlation functions are automatically obtained with the proper ergodic averaging[31]. The inverted data are shown in Fig. 6.11, where the solid and open symbols again represent the data for the 12 and 1000 cP oils respectively. The two sets of data saturate at the same final value, but the characteristic relaxation time for the emulsion of the less viscous oil is somewhat more than one order of magnitude shorter than that of the emulsion of the more viscous oil. The ratio of the two relaxation times is substantially less than the ratio of the viscosities, however, that would be expected from the viscosity dependence of the characteristic relaxation times of isolated droplets. The observed deviation from the expected behavior indicates that the shape fluctuation relaxation rate in a highly compressed emulsion is not controlled solely by the viscosity of the oil, and, instead, additional effects also contribute.

Finally, the fact that the saturation value of the decay of the correlation function is completely independent of viscosity indicates that it does not depend on the dynamics. Instead, it presumably relates to the effects of elasticity of these concentrated emulsions; the elastic modulus is in fact found to be independent of the viscosity of the oil[32]. Moreover, the ϕ-dependence of the saturation level tracks that of elastic modulus[32]. This demonstrates the intrinsic relationship between the shape fluctuations of the droplets and the macroscopic properties of the emulsion.

6.6. Conclusions

In this paper we have generalized the theory of diffusing-wave spectroscopy by incorporating the effects of amplitude fluctuations in the scattering intensity. The formulas we derived can be applied to study dynamic phenomena in which the form factor is time dependent, and the amplitude fluctuations of the scattered light reflect the dynamics of the shape, size, or rotation of scatterers. The detection of these fluctuations makes DWS a more generally useful and applicable technique. We apply this new method to the study of thermally induced shape fluctuations of emulsion droplets whose geometry is controlled by surface tension. Since the surface potential energy of a droplet is much higher than k_BT, the deformation of drop induced by the thermal energy is only a small fraction of its size. This deformation would not be detectable using conventional dynamic light scattering because of its small amplitude and fast relaxation. However, it is feasible using DWS, since the decay of the correlation function results from the combined fluctuations of the large number of scatterers that comprise the scattering path, allowing minute changes in each individual scatterer to be detected. Here, we are able to probe changes in the shapes of the scatterers corresponding to length scales as short as a few angstroms.

From our generalization of the theory for DWS we isolate the contribution of the shape fluctuations and investigate the ϕ-dependence of the characteristic relaxation rate and amplitude of the fluctuations. Very good agreement is obtained between the theory of an isolated droplet and experimental values at low volume fractions. The relaxation behavior exhibits a distinctly non-exponential decay. We conclude that in addition to the lowest mode (l = 2), higher-order fluctuating modes are excited and relax with shorter time constants. However, we found a remarkable scaling behavior of the relaxation process over volume fraction. All data can be scaled onto the correlation function predicted for the shape relaxation of an isolated droplet. Upon extrapolating the scaling

functions to $\phi = 0$, excellent agreement with the theoretically predicted amplitude and characteristic relaxation rate is observed. The characteristic relaxation rate exhibits a linear decrease with volume fraction, while the amplitude of the shape fluctuations shows a non-linear increase. We speculate that the ϕ-dependence of the amplitude of the shape fluctuations is a consequence of collisions and the additional energy transferred from interparticle interaction into the interfacial degrees of freedom. We account for these collisions by relating the ϕ-dependent shape fluctuation amplitude to the radial distribution function at contact. The rapid increase of collisions with volume fraction results in a strong, non-linear increase in the amplitude of shape fluctuations. However, to fully account for the ϕ-dependence, further theoretical work is clearly required; for example, recent computer simulation also exhibit similar behavior[29].

The flexibility of liquid droplets is one of their most distinguishing features; it controls many of their unique properties. The shape fluctuations studied here directly probe this flexibility. Moreover, as the volume fraction increases, shape fluctuations can lead to significant modifications of the properties of the interacting droplets. In particular, these shape fluctuations may make a significant contribution to the onset of an elastic modulus, which occurs as ϕ is increased sufficiently to deform the droplets permanently. The effects of increasing interactions on the shape fluctuations may provide new insight into this important problem. Another important issue is the potential connection between coalescence and shape fluctuations of emulsion droplets. In order to induce coalescence, rupture of the liquid film between the droplets must take place. The rupture of the thin film is usually due to thermal or mechanical fluctuations which result in the stretching of the liquid surface and the formation of surface waves that grow in amplitude until coalescence occurs. Thus, the techniques reported here may provide a new method for probing the stability of emulsions; shape fluctuations may be a critical precursor of coalescence, one of the key mechanisms by which an emulsion is destroyed.

We acknowledge valuable discussions with J. Bibette, W. Cai, T. Lubensky, and S.T. Milner.

*

* The work of this chapter will appear in *Physical Review* **E**, Hu Gang, A.H. Krall and D.A. Weitz, "Thermal Fluctuations of the Shapes of Droplets in Dense and Compressed Emulsions". A short version has been published in *Physical Review Letters*, Hu Gang, A.H. Krall and D.A. Weitz, "Shape Fluctuations of Interacting Fluid Droplets", **73** 3435(1994).

REFERENCES

1. P. Becher, *Emulsion: Theory and Practice*, (Reinhold, New York, 1965).

2. L.L. Schramm, *Emulsions: Fundamentals and Applications in the Petroleum Industry*, (ACS, Washington, D.C., 1992).

3. R.H. Katyl and U. Ingard, *Phys. Rev. Lett.* **20**, 248 (1968).

4. M.K. Sanyal, S.K. Sinha, K.G. Huang and B.M. Ocko, *Phys. Rev. Lett.* **66**, 628 (1991).

5. J.S. Huang, S.T. Milner, B. Farago and D. Richter, *Phys. Rev. Lett.* **59**, 2600 (1987).

6. B. Farago, D. Richter, J.S. Huang, S.A. Safran and S.T. Milner, *Phys. Rev. Lett.* **65**, 3348 (1990).

7. C.R. Safinya, D. Roux, G.S. Smith, S.K. Sinha, P. Dimon, N.A. Clark and A.M. Belloq, *Phys. Rev. Lett.* **57**, 2718 (1986).

8. H.P. Duwe, J. Kaes and E. Sackmann, *J. Phys. (Paris)* **51**, 945 (1990).

9. D.J. Pine, D.A. Weitz, P.M. Chaikin and E. Herbolzheimer, *Phys. Rev. Lett.* **60**, (1988).

10. D.A. Weitz and D.J. Pine, in *Dynamic Light Scattering*, W. Brown, Ed. (Oxford University Press, Oxford, 1992).

11. D.A. Weitz, J.X. Zhu, D.J. Durian, H. Gang and D.J. Pine, *Physica Scripta* **T49**, 610 (1993).

12. J.-Z. Xue, X.-L. Wu, D.J. Pine and P.M. Chaikin, *Phys. Rev. A* **45**, 989 (1992).

13. J.X. Zhu, D.A. Weitz and R. Klein, in *Photonic Band Gaps and Localization*, C. Soukoulis, Eds. (Plenum, New York, 1993).

14. A.J.C. Ladd, H. Gang, J.X. Zhu and D.A. Weitz, *Phys. Rev. Lett.* **74**, 318 (1995).

15. A.J.C. Ladd, H. Gang, J.X. Zhu and D.A. Weitz, *Phys.Rev.E,* in press.

16. P.E. Wolf, G. Maret, E. Akkermans and R. Maynard, *J. Phys. (Paris)* **49**, 63 (1988).

17. S.T. Milner and S.A. Safran, *Phys. Rev. A* **36**, 4371 (1987).

18. H. Lamb, *Hydrodynamics*, (Dover, New York, 1932).

19. R.G. Cox, *J. Fluid Mech.* **37**, 601 (1969).

20. S.J. Choi and W.R. Schowalter, *Phys. Fluids* **18**, 420 (1974).

21. M. Kerker, *The Scattering of Light and Other Electromagnetic Radiation*, (Academic Press, New York, 1969).

22. J. Bibette, *J. Coll. Interface Sci.* **147**, 474 (1991).

23. P.N. Pusey and W. van Megan, *Nature* **320**, 340 (1986).

24. J. Ricka, *Applied Optics* **32**, 2860 (1993).

25. W. Hess and R. Klein, *Advances in Physics* **32**, 173 (1983).

26. E.J. Hinch, *J. Fluid Mech.* **72**, 499 (1975).

27. M. Schwartz and S.F. Edwards, *Physica A* **167**, 589 (1990).

28. J.F. Brady, *J. Chem. Phys.* **99**, 567 (1993).

29. W. Cai, pre-print.

30. W. van Megan and S.M. Underwood, *Phys. Rev. E* **49**, 4206 (1994).

31. P.N. Pusey and W. van Megan, *Physica A* **157**, 705 (1989).

32. T.G. Mason et al., *Phys. Rev. Lett.*, submitted.

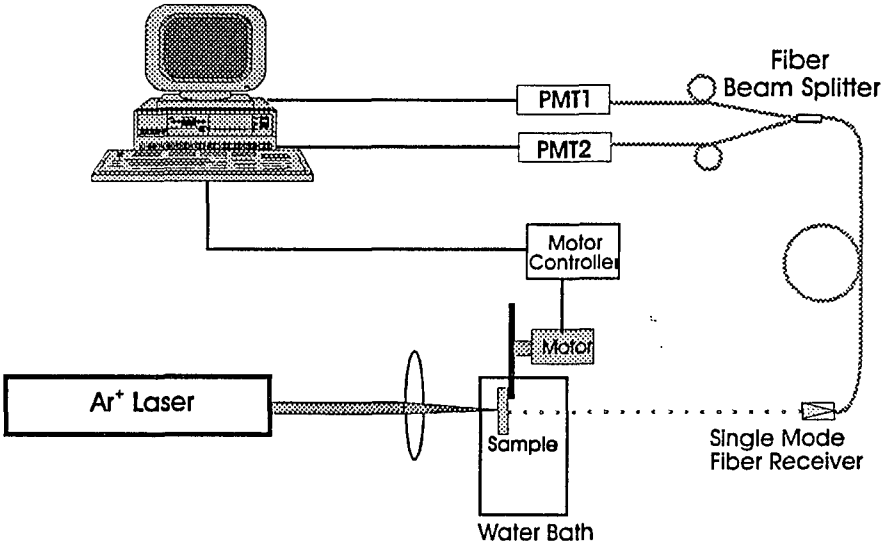
Fiber
Beam Splitter
PMT1
PMT2
Motor
Controller
Motor
Ar+ Laser
Sample
Single Mode
Fiber Receiver
Water Bath

Fig. 2.1

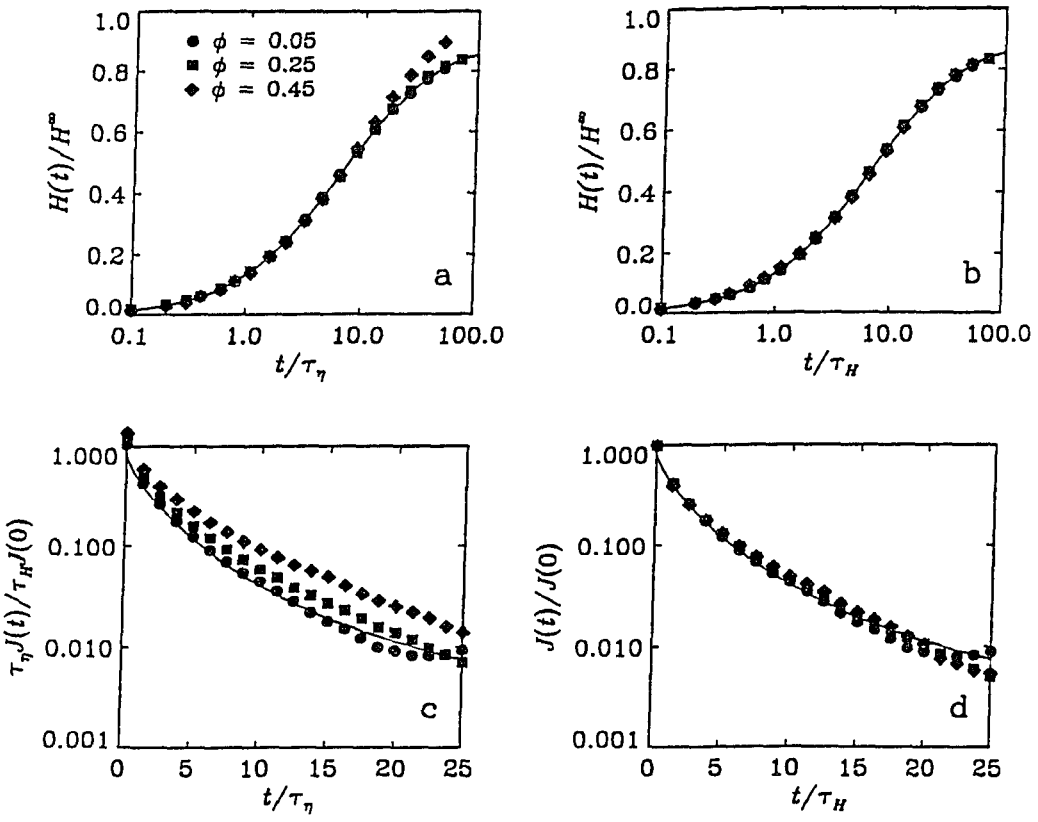
1.0
0.8
0.6
0.4
0.2
0.0
$H(t)/H^{\infty}$
ϕ = 0.05
ϕ = 0.25
ϕ = 0.45
a
0.1
1.0
10.0
100.0
t/τ_{η}
b
t/τ_{H}
1.000
0.100
0.010
0.001
$\tau_{\eta}J(t)/\tau_{H}J(0)$
c
0
5
10
15
20
25
$J(t)/J(0)$
d

Fig. 3.1

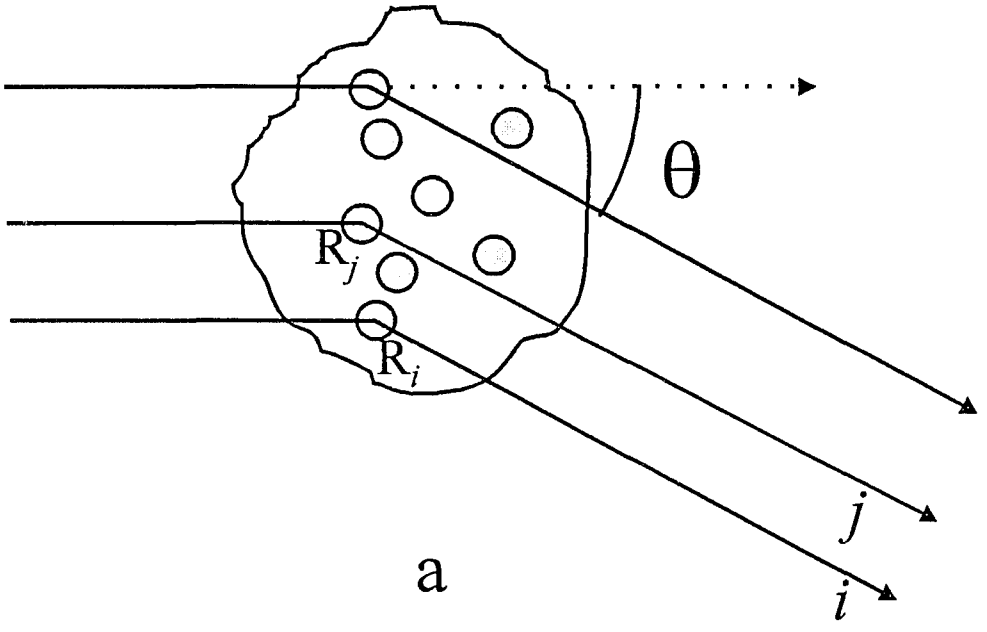
θ
R_j
R_i
j
i

a

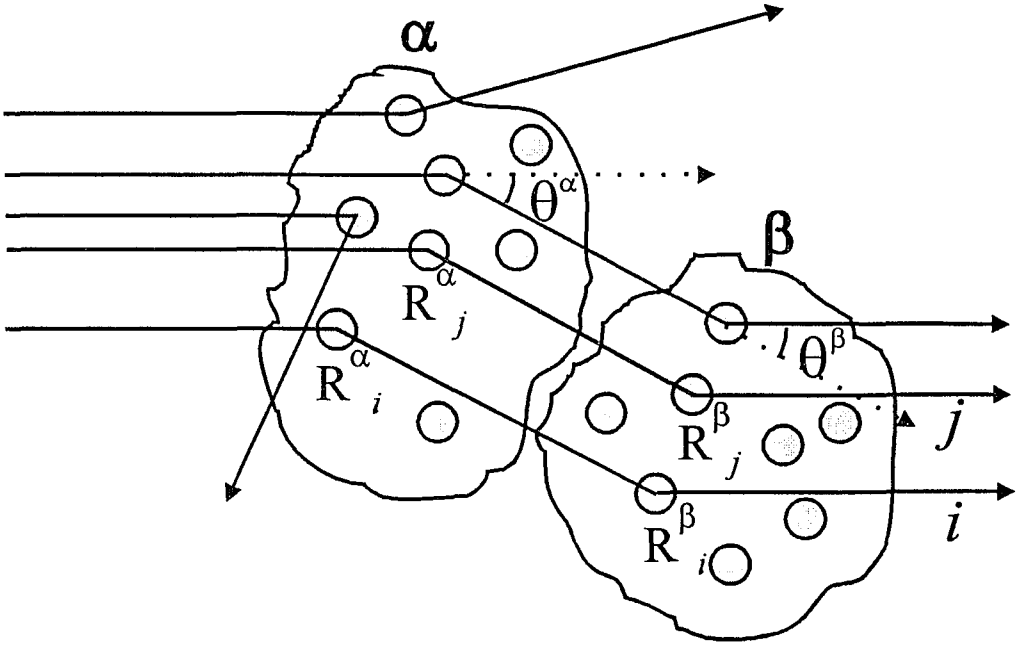
α
β
θ^{α}
θ^{β}
R^{α}_{j}
R^{α}_{i}
R^{β}_{j}
R^{β}_{i}
j
i

b

Fig. 3.2

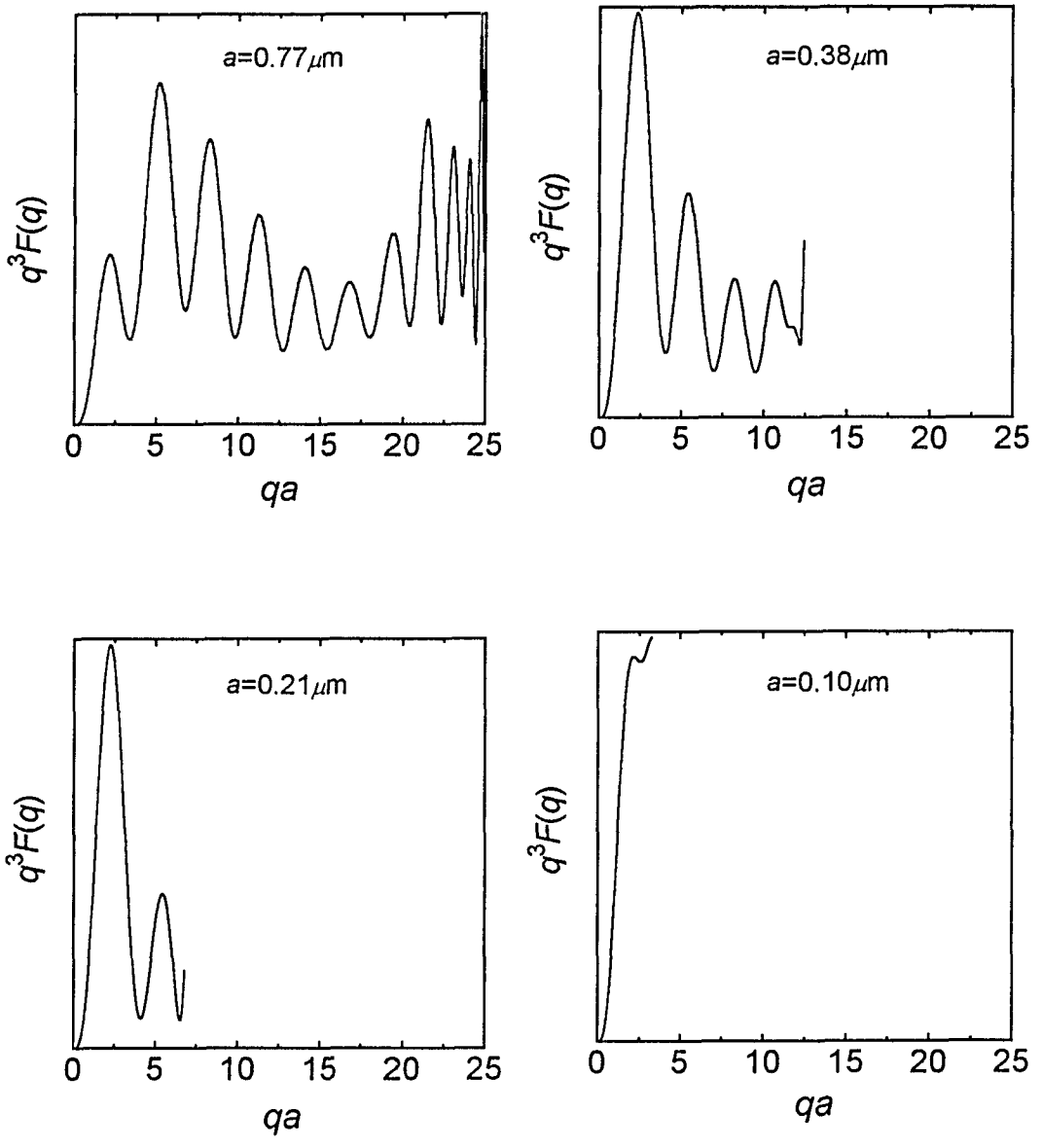

Fig. 3.3

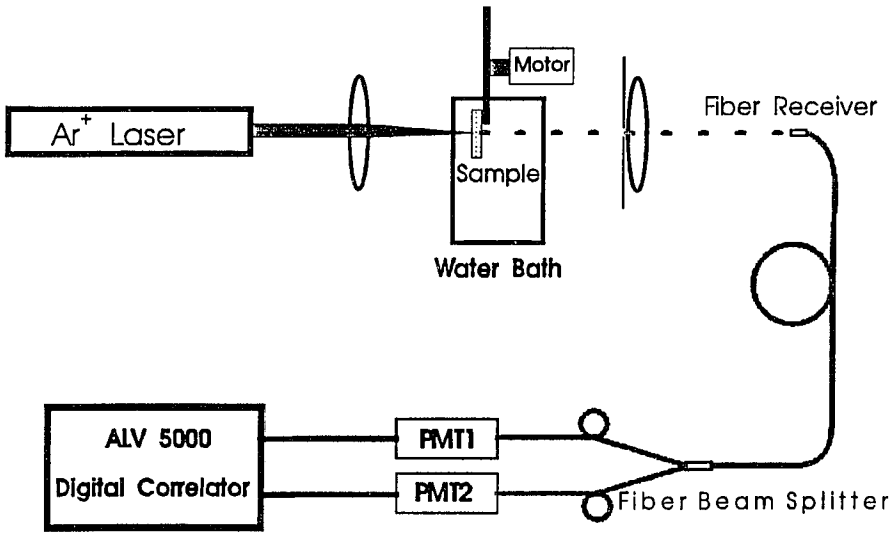
Motor
Ar+ Laser
Sample
Fiber Receiver
Water Bath
ALV 5000
Digital Correlator
PMT1
PMT2
Fiber Beam Splitter

Fig. 3.4

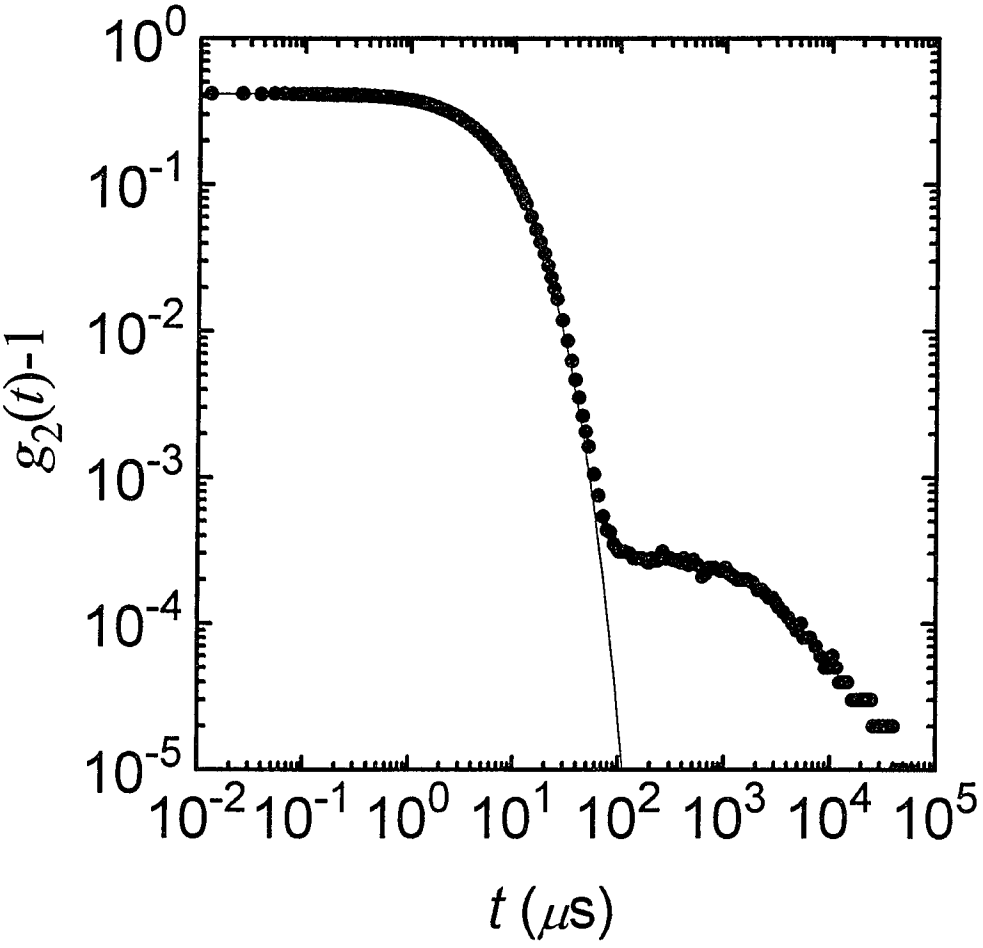
10^0
10^{-1}
10^{-2}
10^{-3}
10^{-4}
10^{-5}
$g_2(t)$-1
10^{-2} 10^{-1} 10^0 10^1 10^2 10^3 10^4 10^5
t (μs)

Fig. 3.5

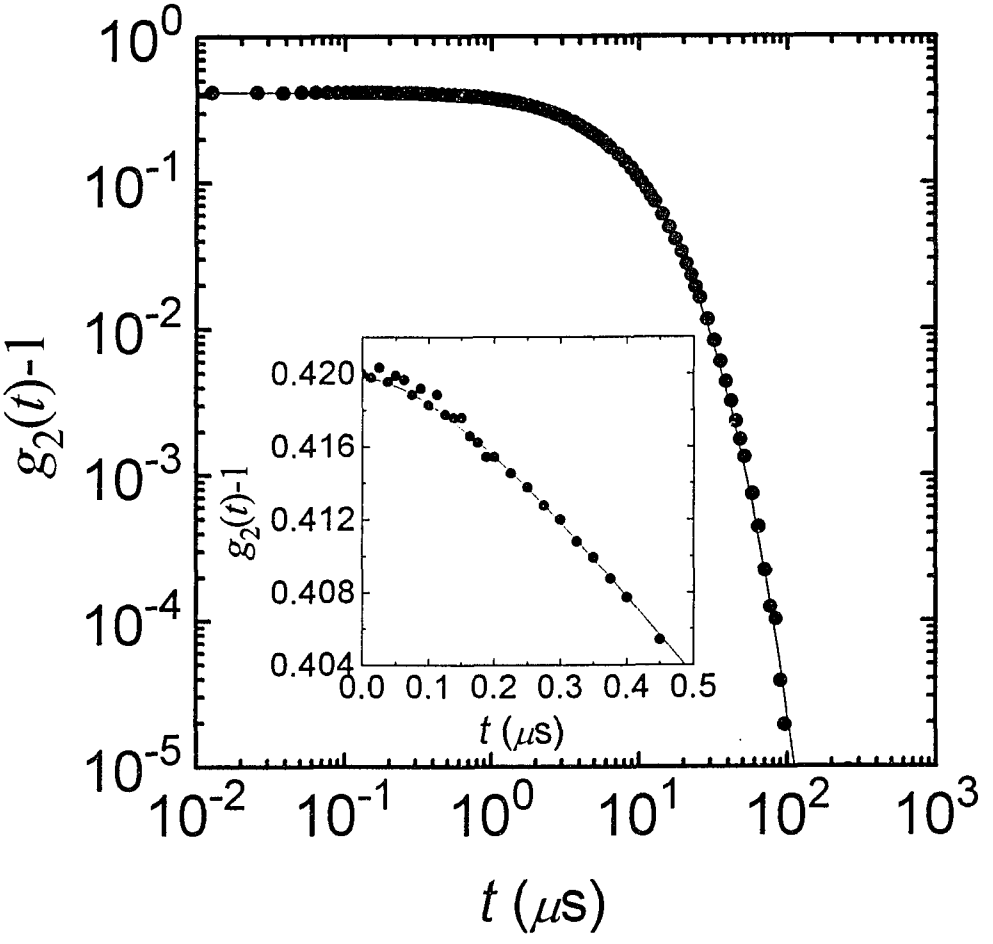
10^0
10^{-1}
10^{-2}
10^{-3}
10^{-4}
10^{-5}
$g_2(t)$-1
10^{-2}
10^{-1}
10^0
10^1
10^2
10^3
t (μs)
0.420
0.416
0.412
0.408
0.404
$g_2(t)$-1
0.0
0.1
0.2
0.3
0.4
0.5
t (μs)

Fig. 3.6

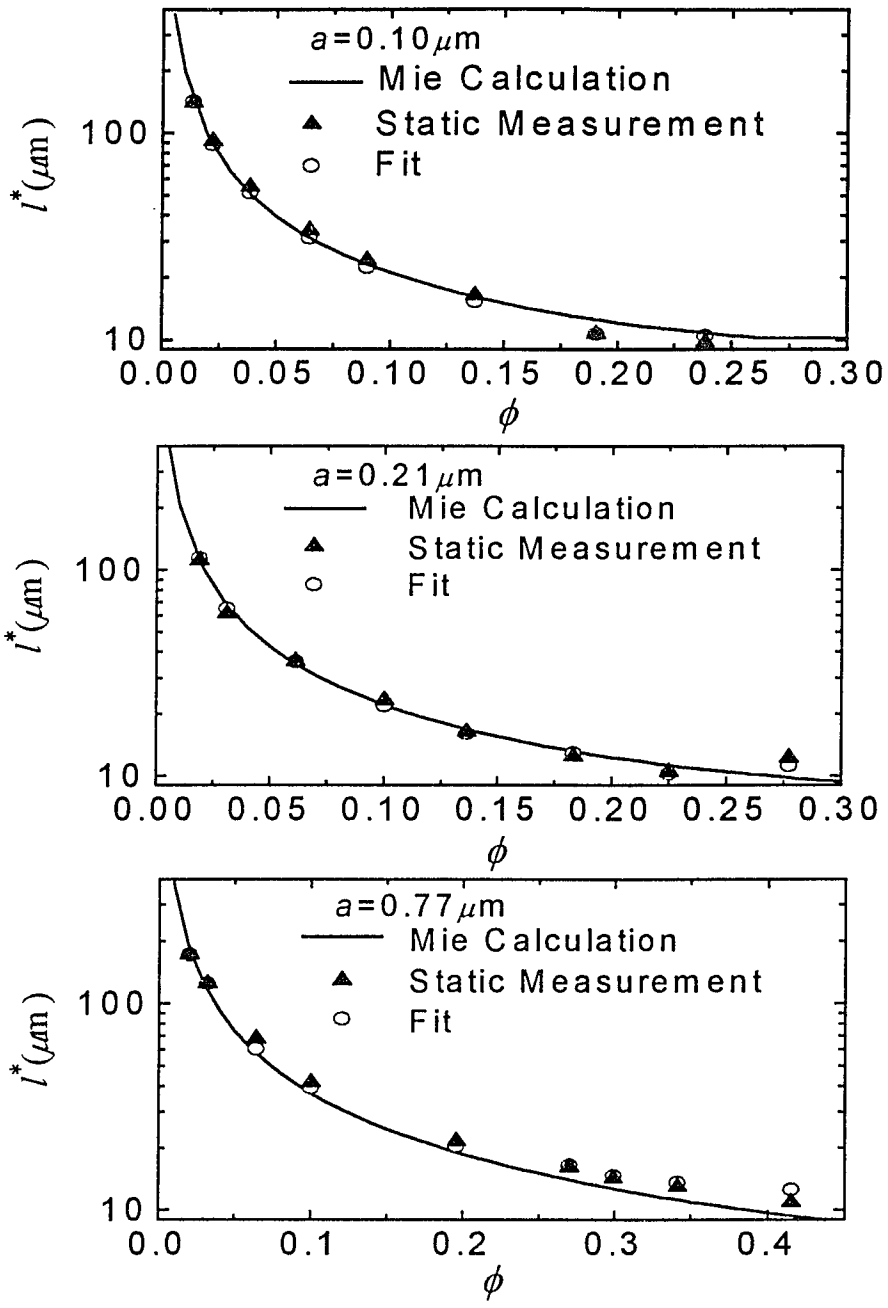
a=0.10μm
Mie Calculation
Static Measurement
Fit
l*(μm)
100
10
0.00 0.05 0.10 0.15 0.20 0.25 0.30
φ
a=0.21μm
Mie Calculation
Static Measurement
Fit
l*(μm)
100
10
0.00 0.05 0.10 0.15 0.20 0.25 0.30
φ
a=0.77μm
Mie Calculation
Static Measurement
Fit
l*(μm)
100
10
0.0 0.1 0.2 0.3 0.4
φ

Fig. 3.7

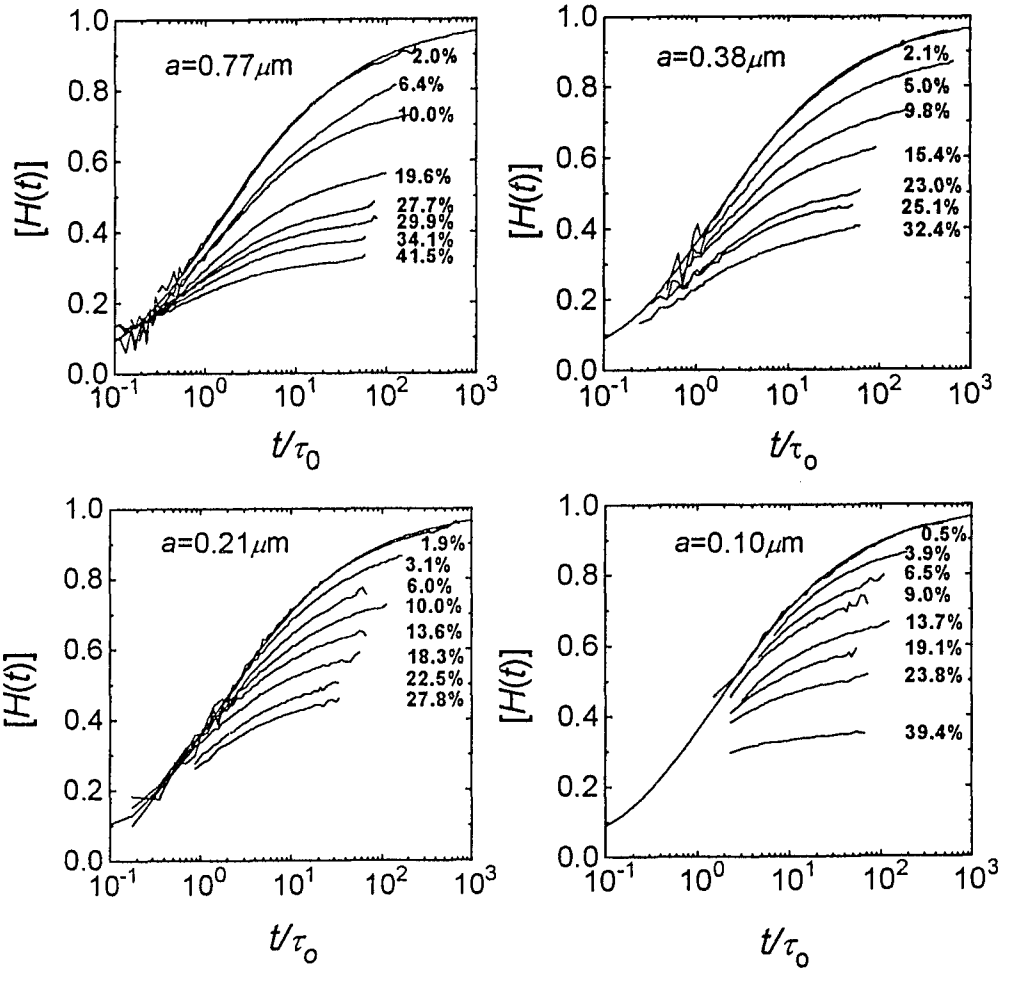
a=0.77μm
2.0%
6.4%
10.0%
19.6%
27.7%
29.9%
34.1%
41.5%
a=0.38μm
2.1%
5.0%
9.8%
15.4%
23.0%
25.1%
32.4%
a=0.21μm
1.9%
3.1%
6.0%
10.0%
13.6%
18.3%
22.5%
27.8%
a=0.10μm
0.5%
3.9%
6.5%
9.0%
13.7%
19.1%
23.8%
39.4%
[H(t)]
t/τ0
t/τo

Fig. 3.8

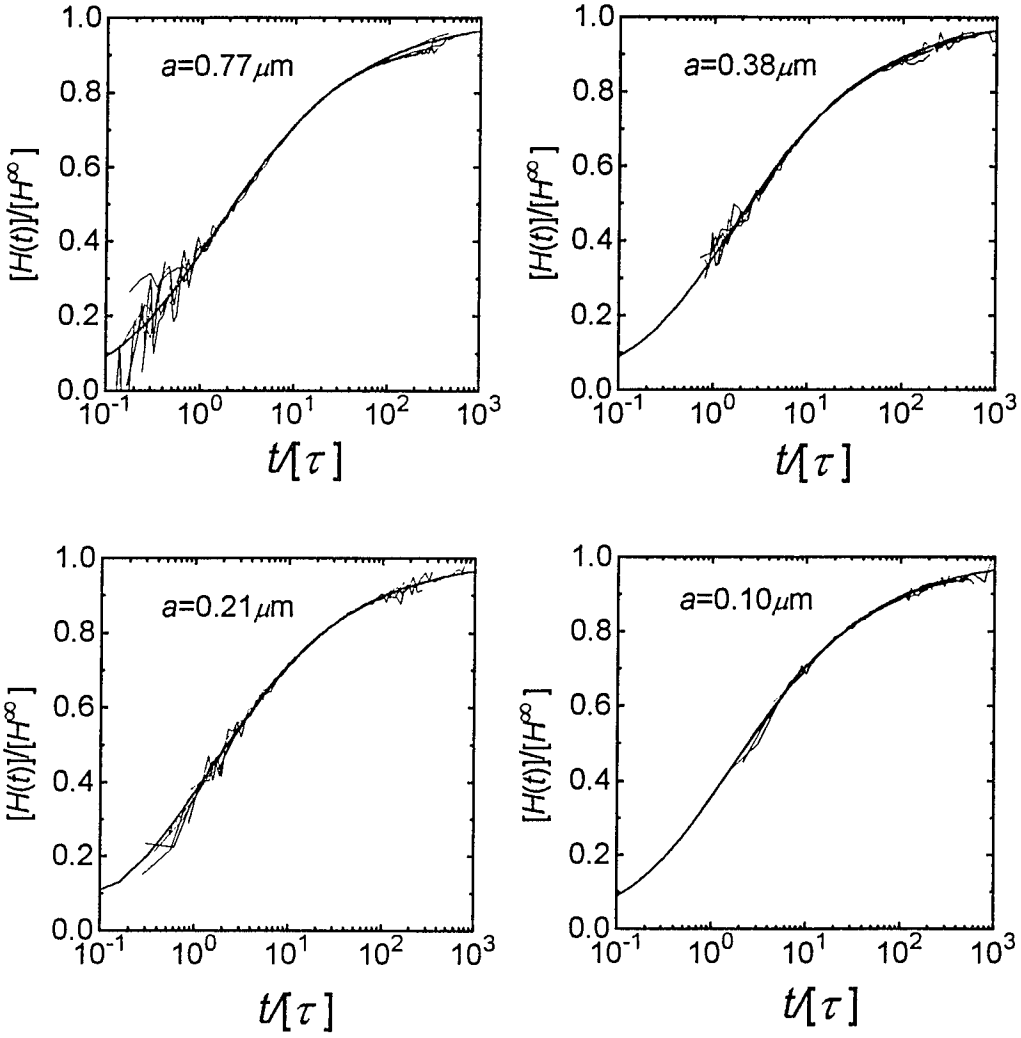
a=0.77μm
a=0.38μm
a=0.21μm
a=0.10μm
[H(t)]/[H∞]
t/[τ]
1.0
0.8
0.6
0.4
0.2
0.0
10^-1
10^0
10^1
10^2
10^3

Fig. 3.9

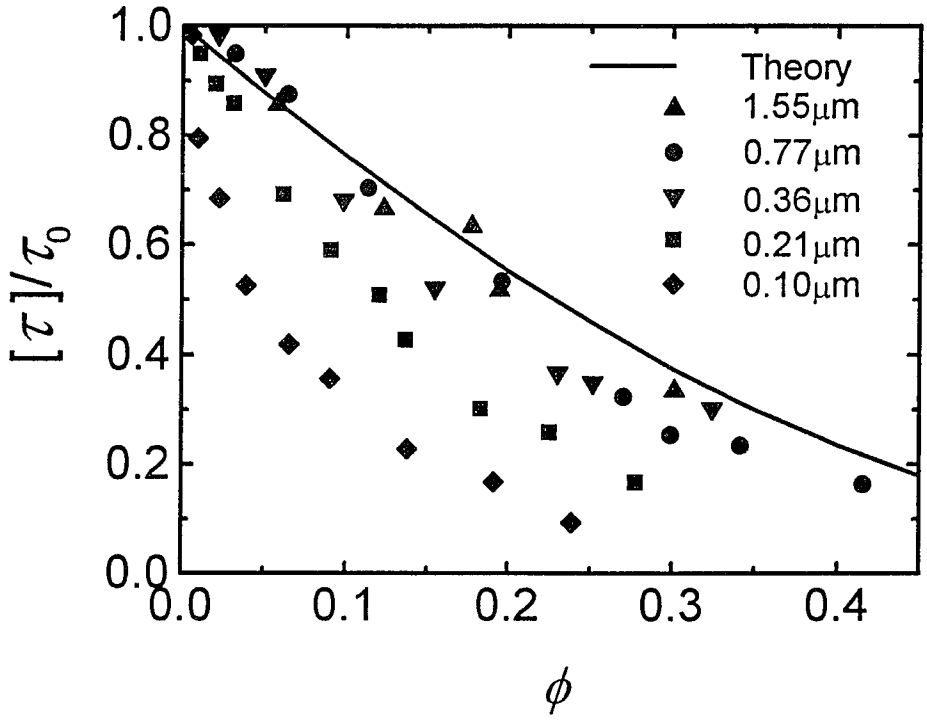
1.0
0.8
0.6
0.4
0.2
0.0
0.0
0.1
0.2
0.3
0.4
$[\tau]/\tau_0$
ϕ
Theory
1.55μm
0.77μm
0.36μm
0.21μm
0.10μm

Fig. 3.10

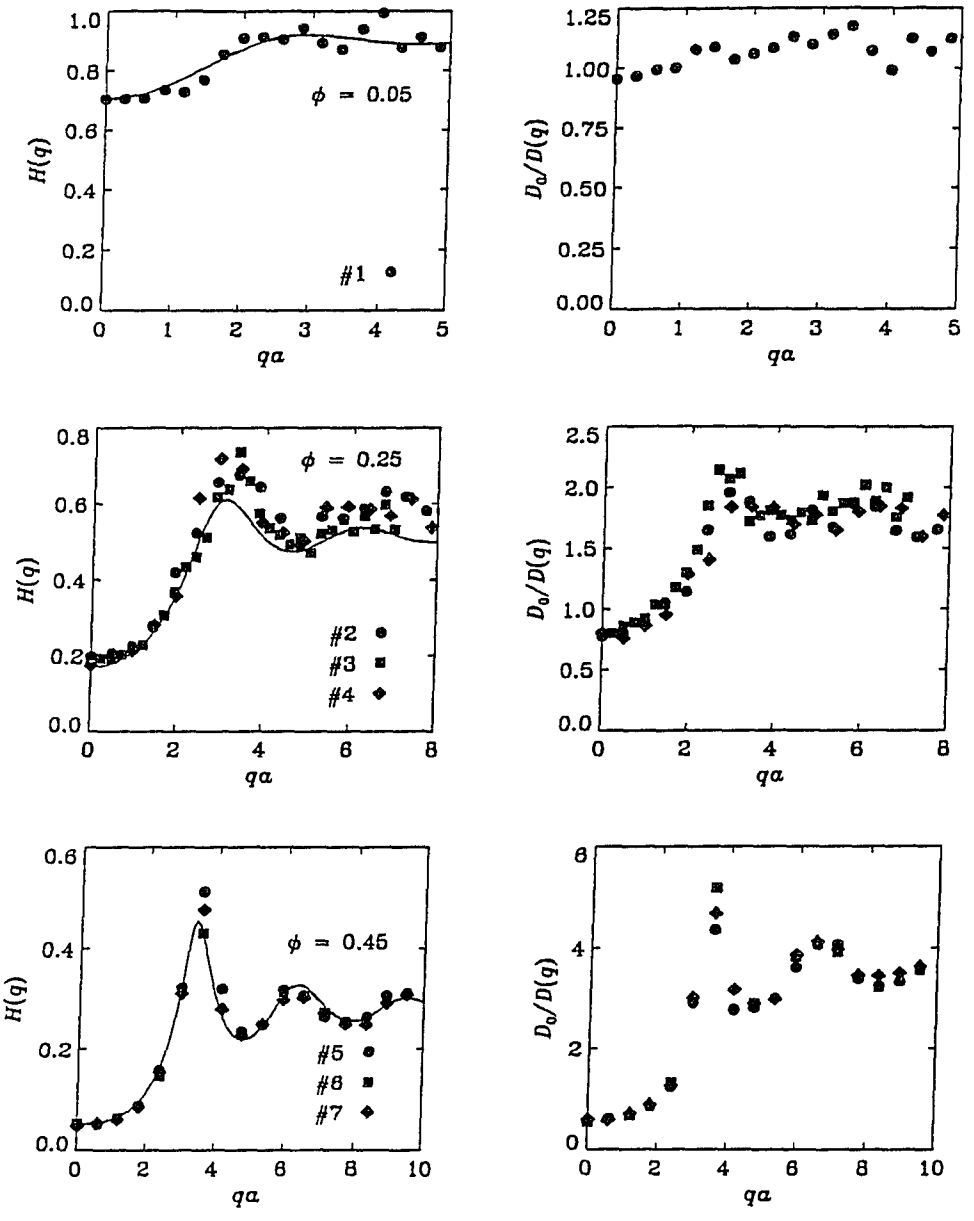

Fig. 3.11

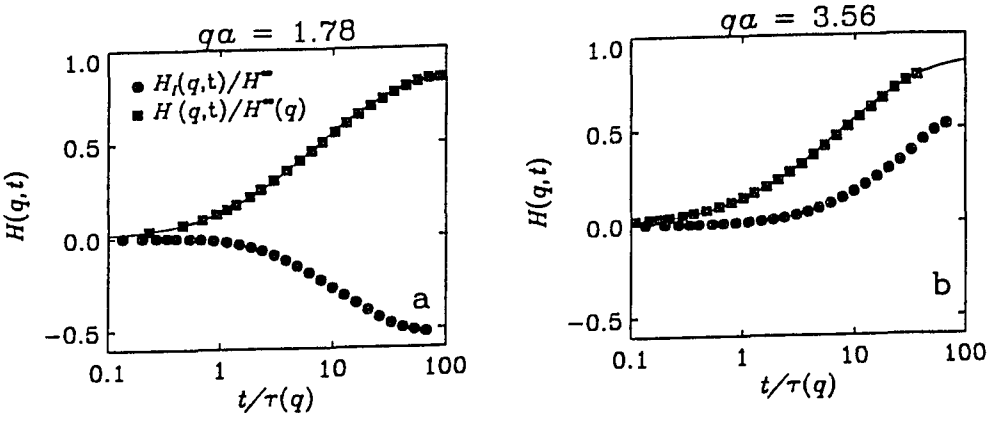

Fig. 3.12

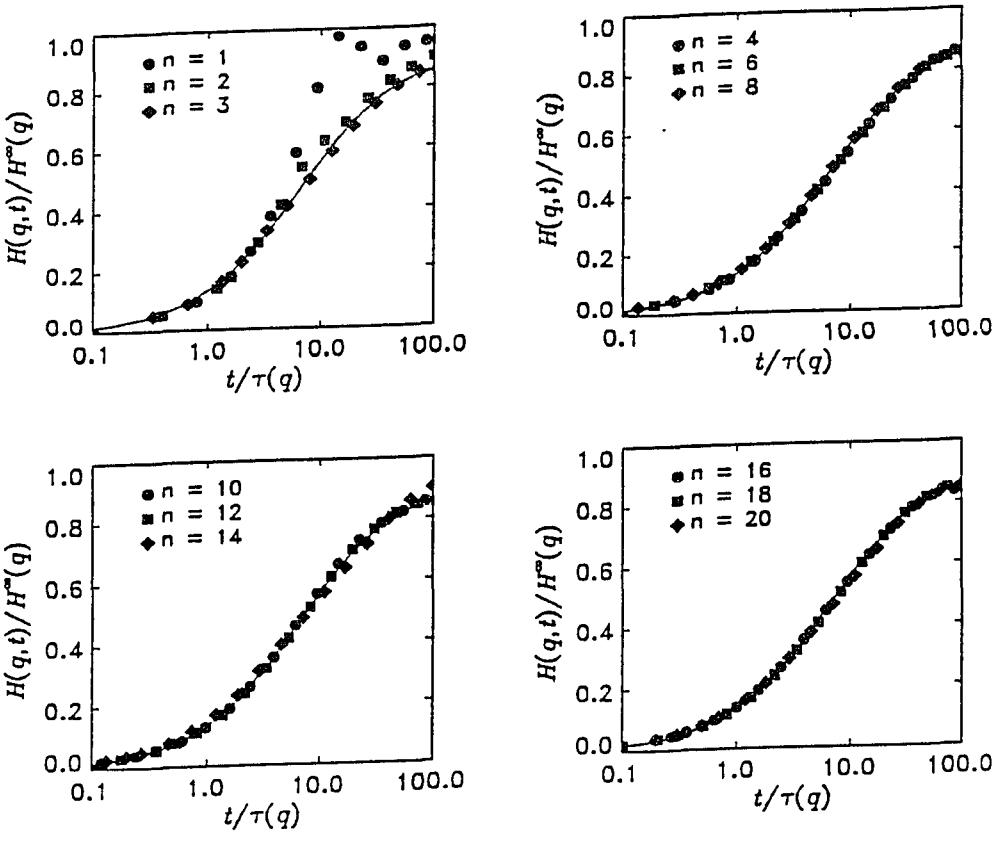
n = 1
n = 2
n = 3
n = 4
n = 6
n = 8
n = 10
n = 12
n = 14
n = 16
n = 18
n = 20
$H(q,t)/H^{\infty}(q)$
$t/\tau(q)$
0.0
0.2
0.4
0.6
0.8
1.0
0.1
1.0
10.0
100.0

Fig. 3.13

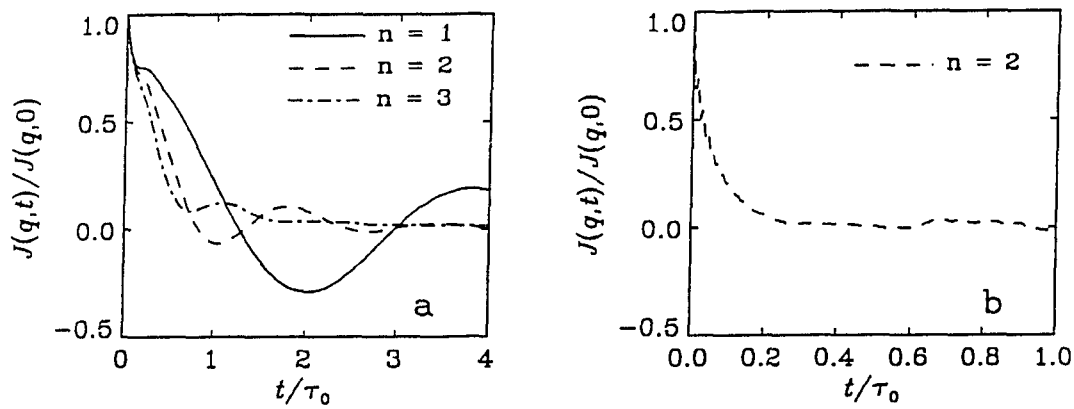
1.0
0.5
0.0
−0.5
J(q,t)/J(q,0)
n = 1
n = 2
n = 3
a
0
1
2
3
4
t/τ0
1.0
0.5
0.0
−0.5
J(q,t)/J(q,0)
n = 2
b
0.0
0.2
0.4
0.6
0.8
1.0
t/τ0

Fig. 3.14

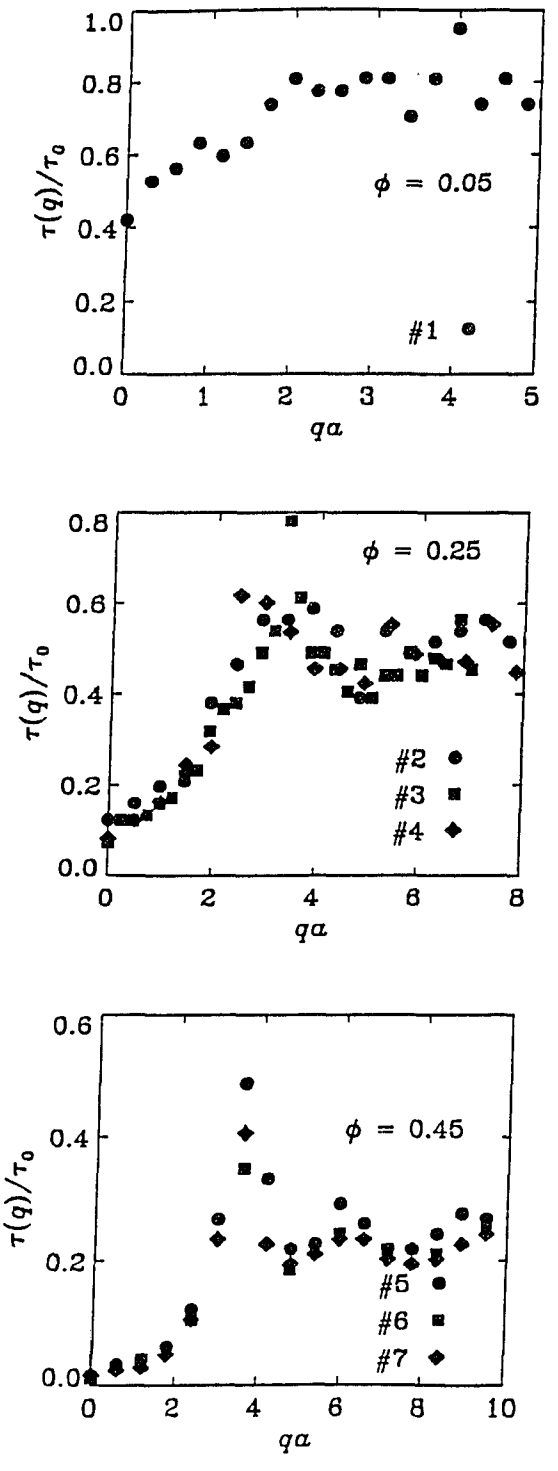
1.0
0.8
0.6
0.4
0.2
0.0
τ(q)/τ₀
ϕ = 0.05
#1
0
1
2
3
4
5
qa
0.8
0.6
0.4
0.2
0.0
τ(q)/τ₀
ϕ = 0.25
#2
#3
#4
0
2
4
6
8
qa
0.6
0.4
0.2
0.0
τ(q)/τ₀
ϕ = 0.45
#5
#6
#7
0
2
4
6
8
10
qa

Fig. 3.15

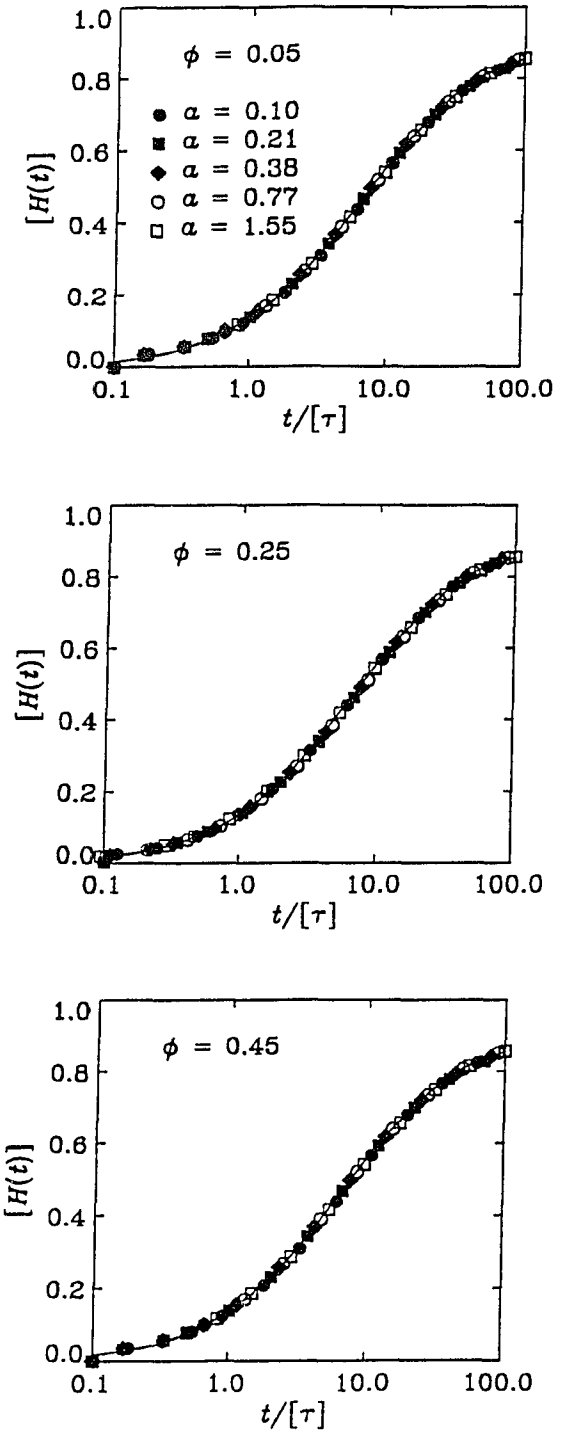
ϕ = 0.05
a = 0.10
a = 0.21
a = 0.38
a = 0.77
a = 1.55
[H(t)]
t/[τ]
ϕ = 0.25
[H(t)]
t/[τ]
ϕ = 0.45
[H(t)]
t/[τ]

Fig. 3.16

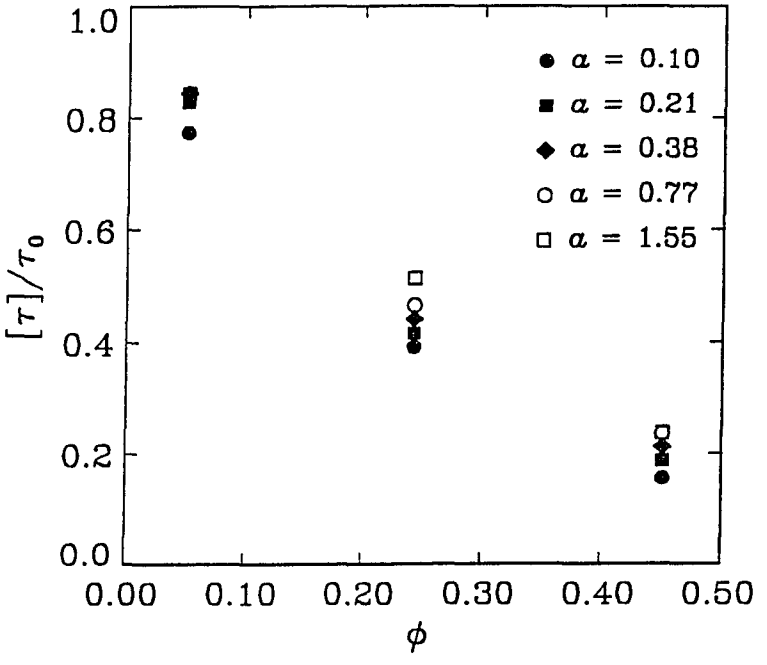
1.0
0.8
0.6
0.4
0.2
0.0
$[\tau]/\tau_0$
0.00
0.10
0.20
0.30
0.40
0.50
ϕ
a = 0.10
a = 0.21
a = 0.38
a = 0.77
a = 1.55

Fig. 3.17

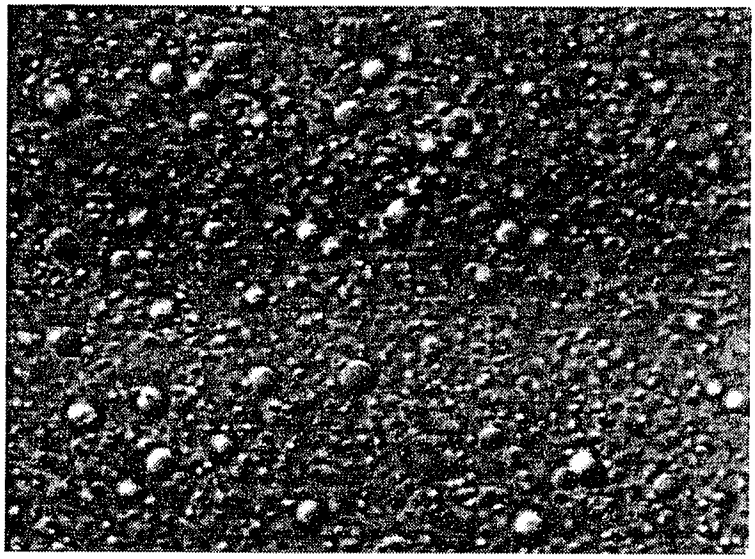

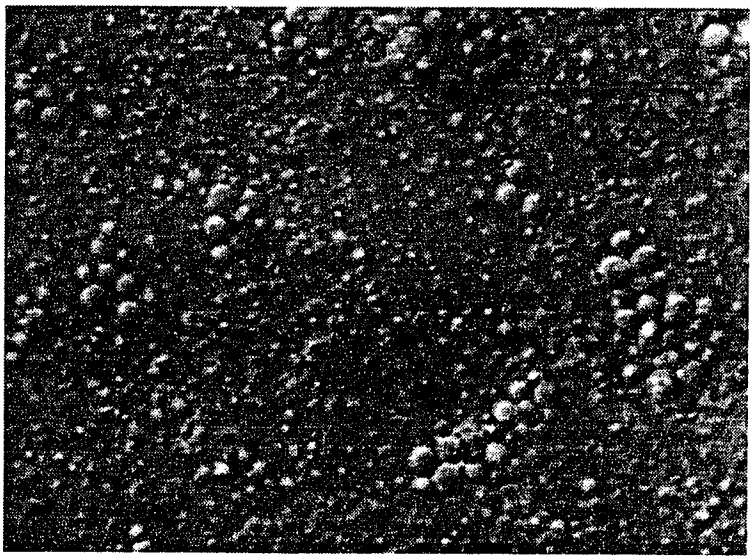

Fig. 4.1

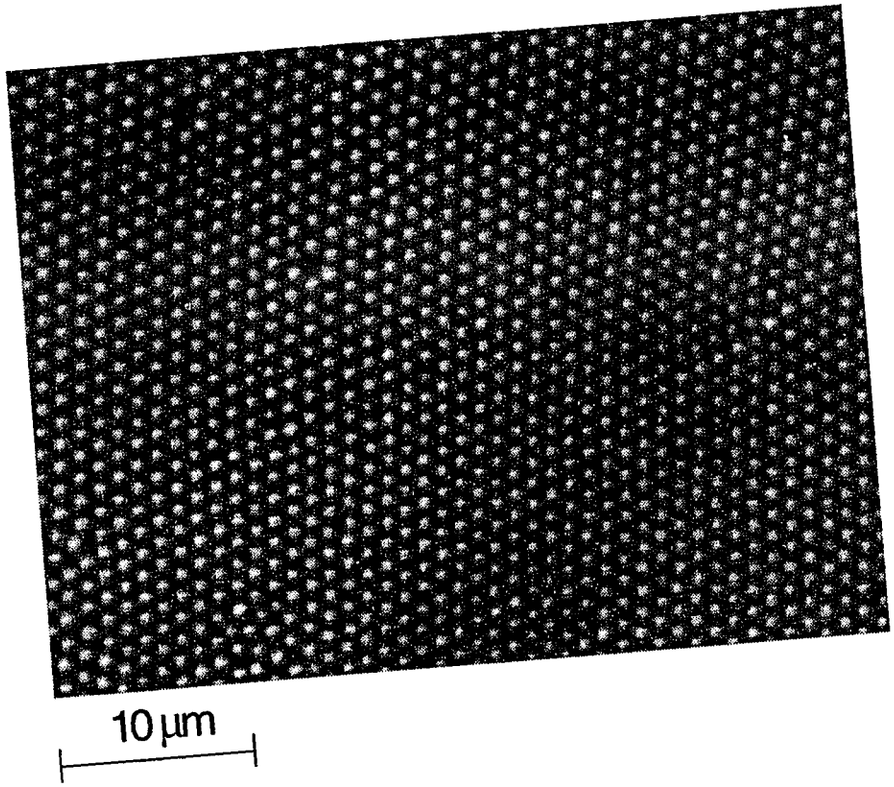

Fig. 4.2

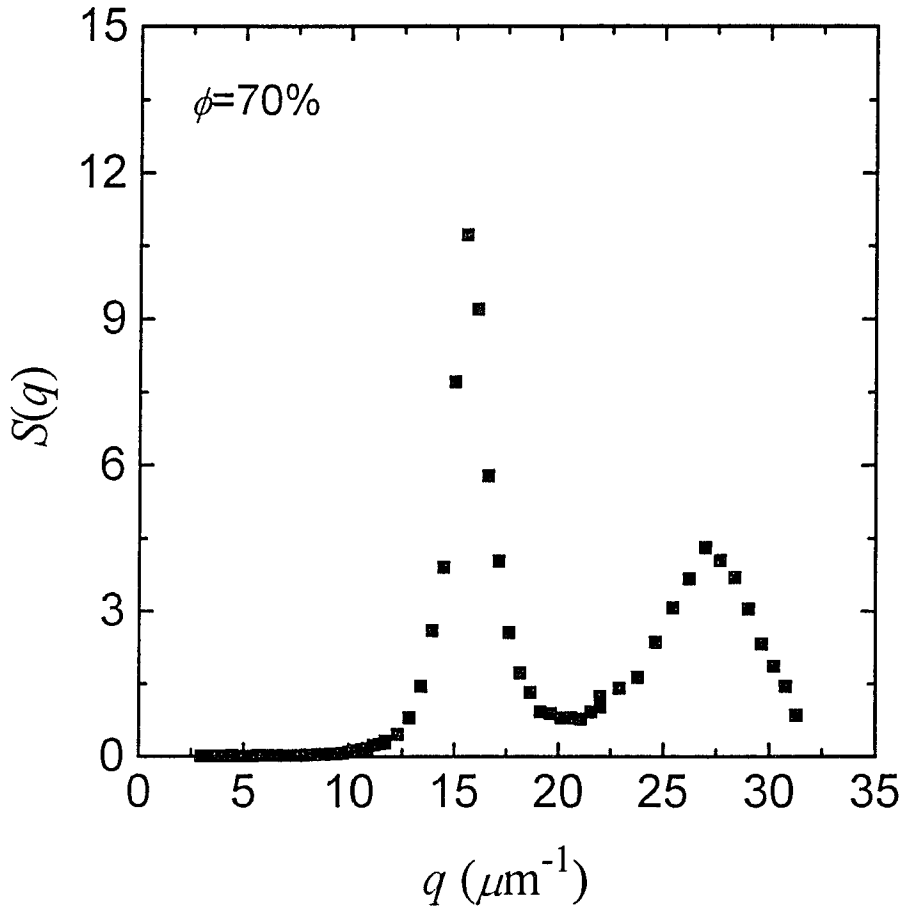

Fig. 5.1

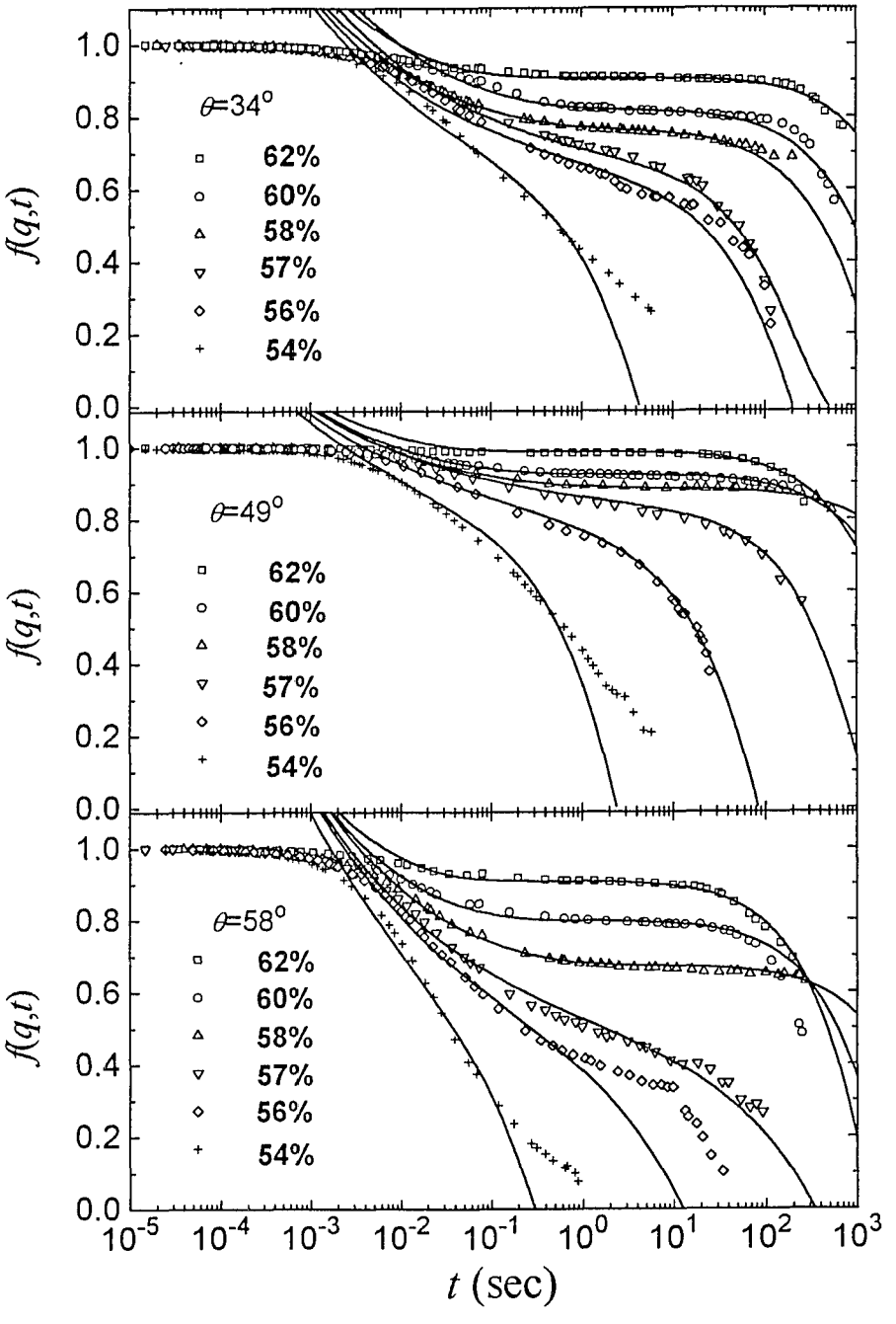

Fig.5.2

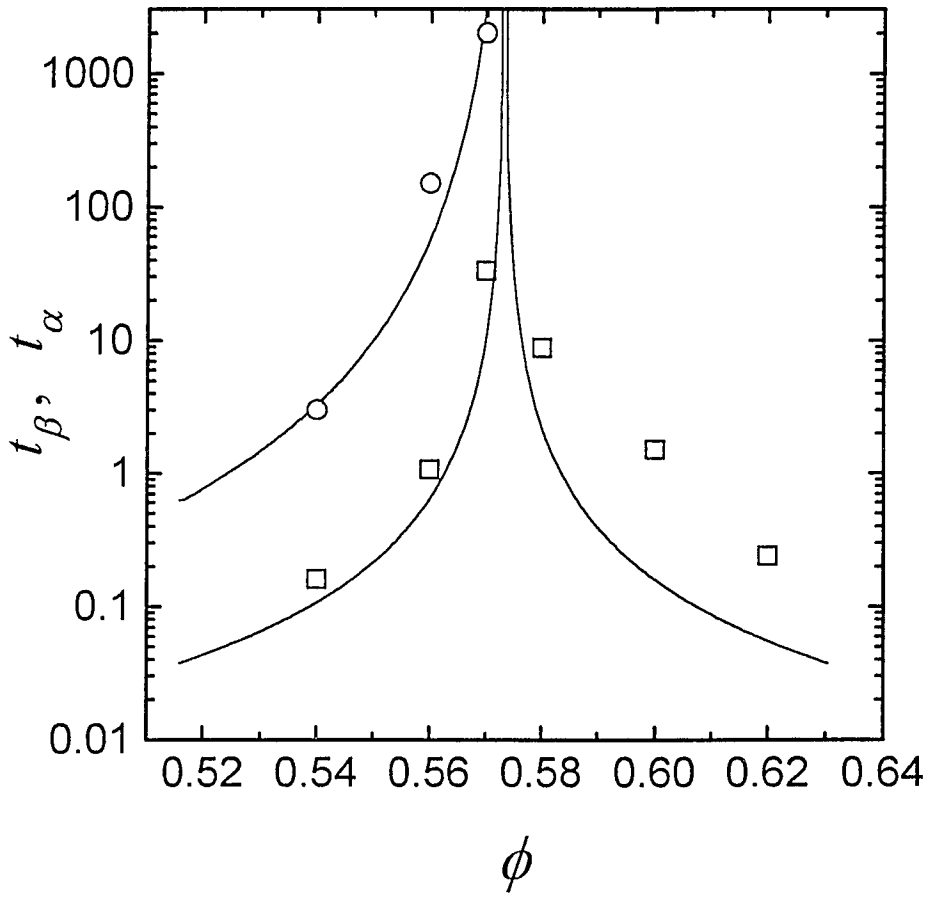
1000
100
10
1
0.1
0.01
t_β, t_α
0.52
0.54
0.56
0.58
0.60
0.62
0.64
ϕ

Fig. 5.3

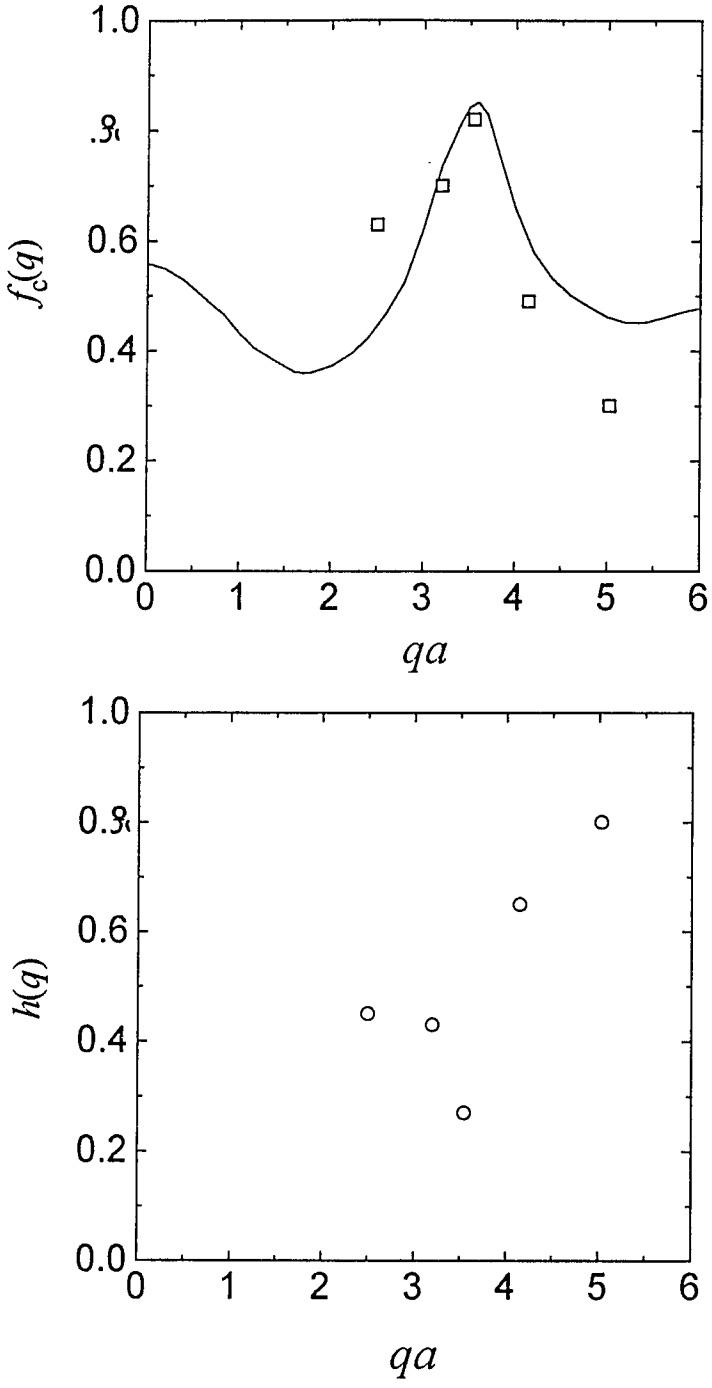

Fig. 5.4

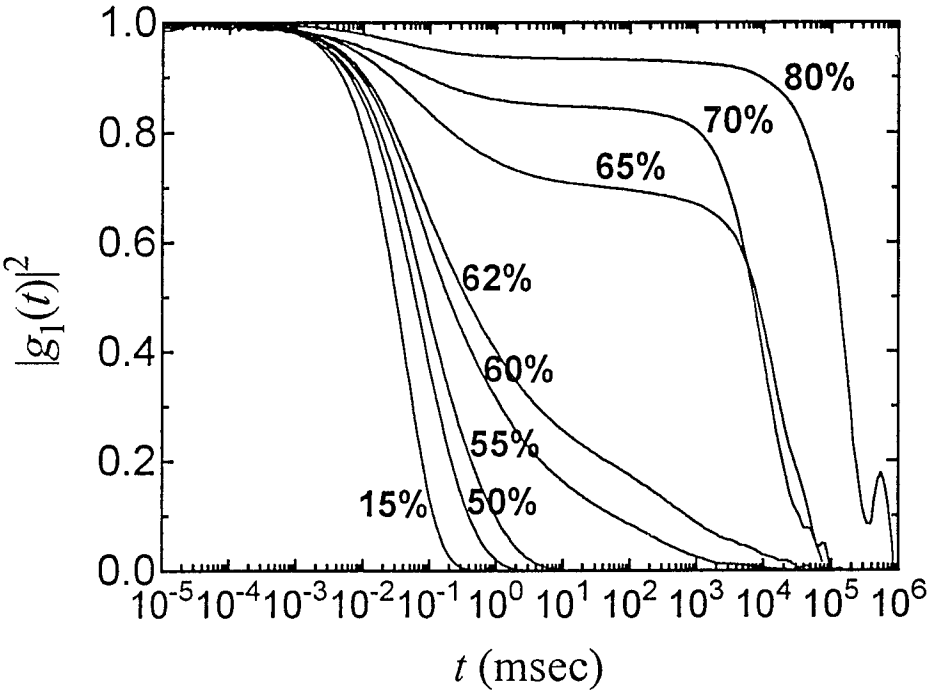
1.0
0.8
0.6
0.4
0.2
0.0
$|g_1(t)|^2$
80%
70%
65%
62%
60%
55%
50%
15%
10^{-5} 10^{-4} 10^{-3} 10^{-2} 10^{-1} 10^{0} 10^{1} 10^{2} 10^{3} 10^{4} 10^{5} 10^{6}
t (msec)

Fig. 5.5

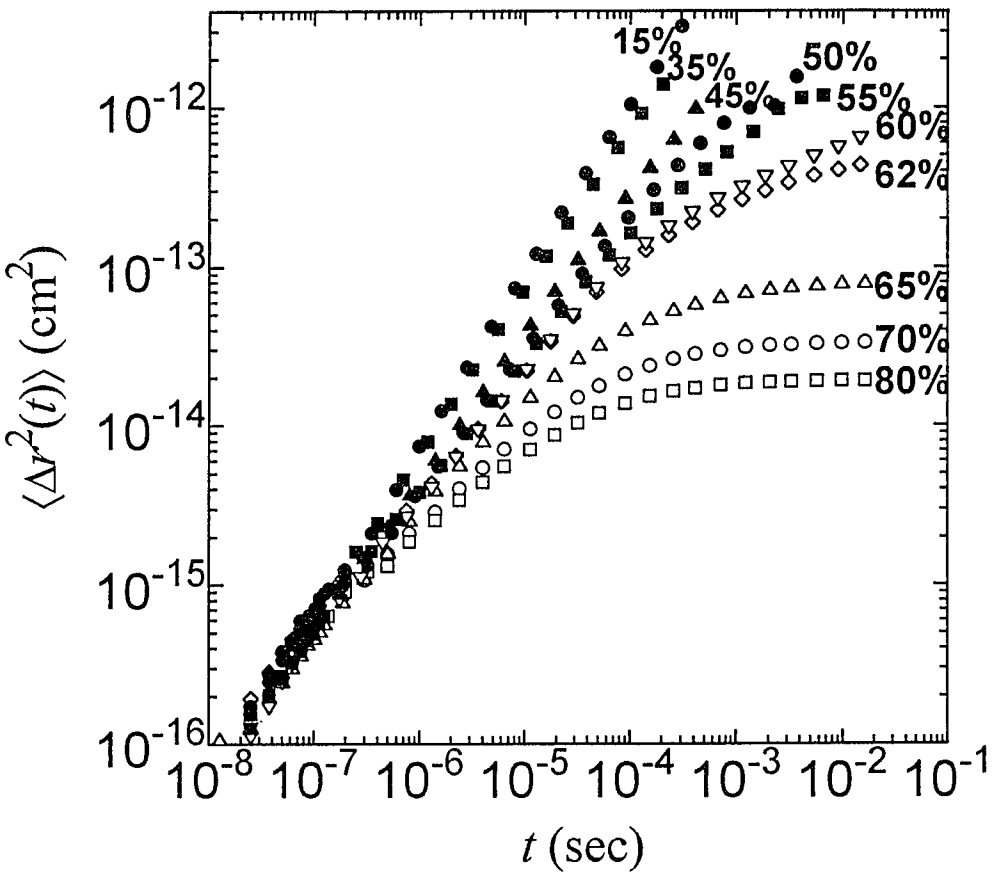
15%
35%
50%
45%
55%
60%
62%
65%
70%
80%
10^{-12}
10^{-13}
10^{-14}
10^{-15}
10^{-16}
$\langle \Delta r^2(t) \rangle$ (cm^2)
10^{-8} 10^{-7} 10^{-6} 10^{-5} 10^{-4} 10^{-3} 10^{-2} 10^{-1}
t (sec)

Fig. 5.6

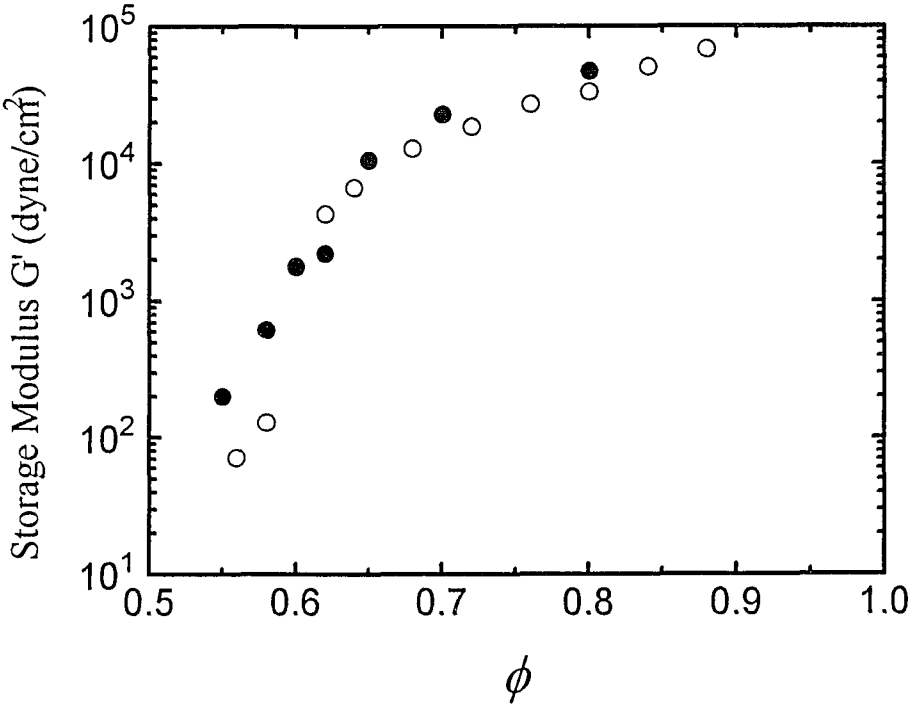
Storage Modulus G' (dyne/cm²)
10⁵
10⁴
10³
10²
10¹
0.5
0.6
0.7
0.8
0.9
1.0
φ

Fig. 5.7

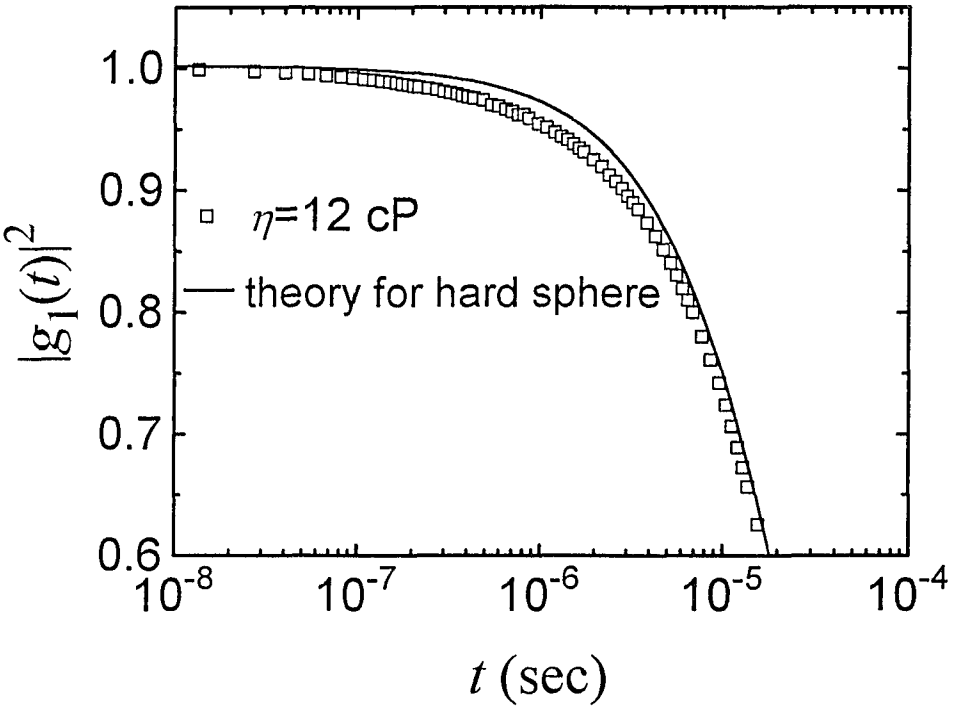
1.0
0.9
0.8
0.7
0.6
$|g_1(t)|^2$
η=12 cP
theory for hard sphere
10^{-8}
10^{-7}
10^{-6}
10^{-5}
10^{-4}
t (sec)

Fig. 6.1

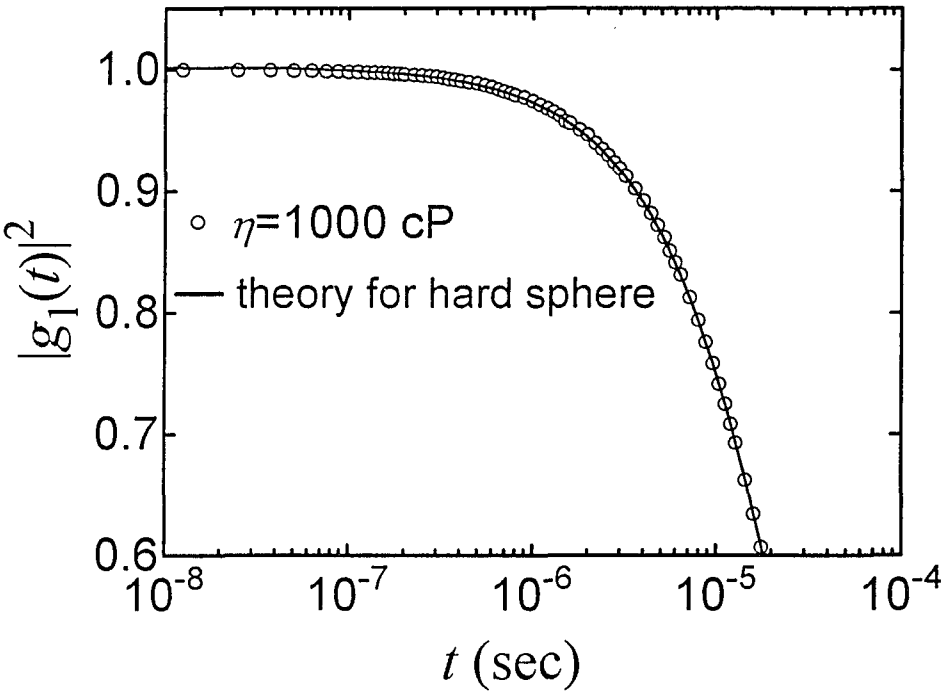
1.0
0.9
0.8
0.7
0.6
$|g_1(t)|^2$
η=1000 cP
theory for hard sphere
10^{-8}
10^{-7}
10^{-6}
10^{-5}
10^{-4}
t (sec)

Fig. 6.2

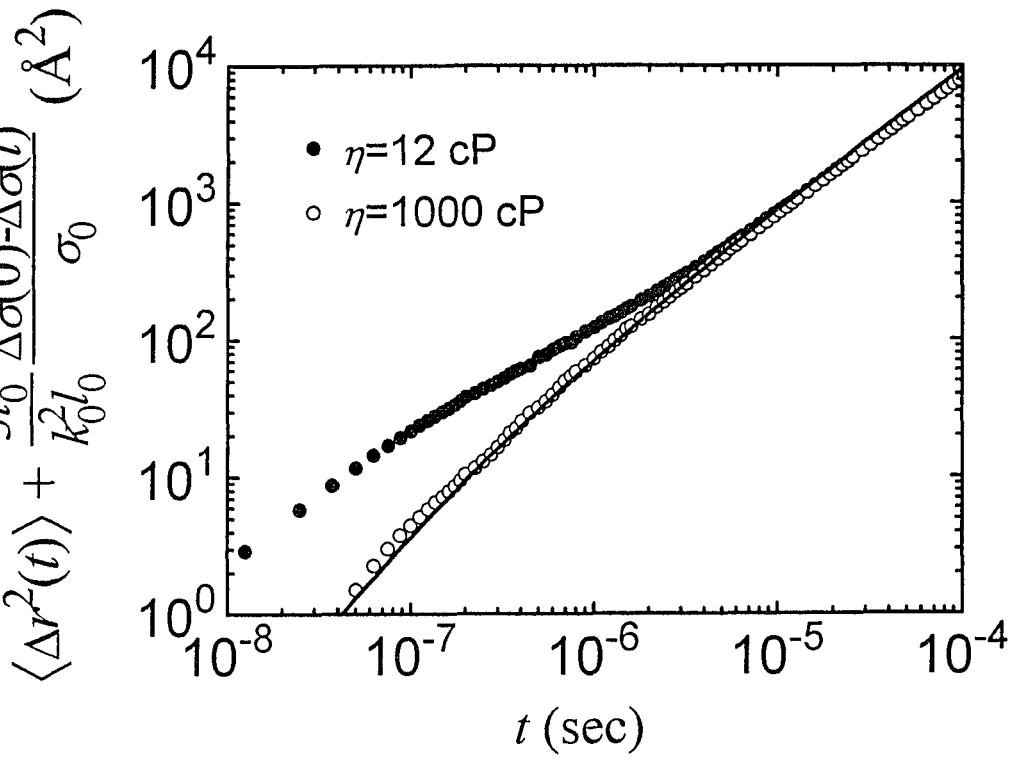
$\langle \Delta r^2(t) \rangle + \frac{3l_0^*}{k_0^2 l_0} \frac{\Delta\sigma(0)-\Delta\sigma(t)}{\sigma_0}$ (Å^2)
10^4
10^3
10^2
10^1
10^0
η=12 cP
η=1000 cP
10^{-8}
10^{-7}
10^{-6}
10^{-5}
10^{-4}
t (sec)

Fig. 6.3

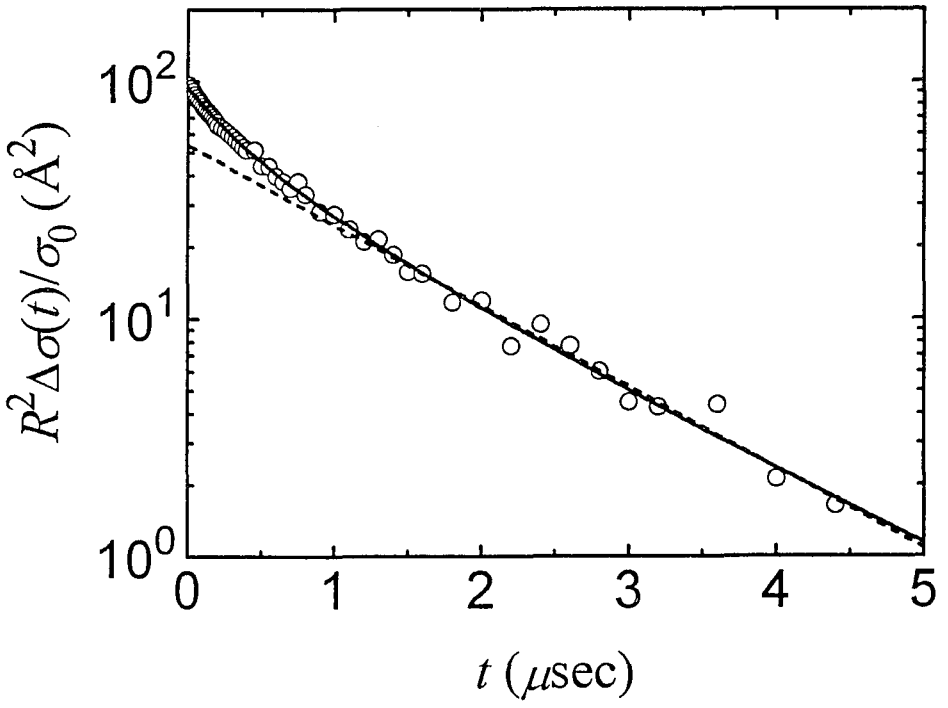

Fig. 6.4

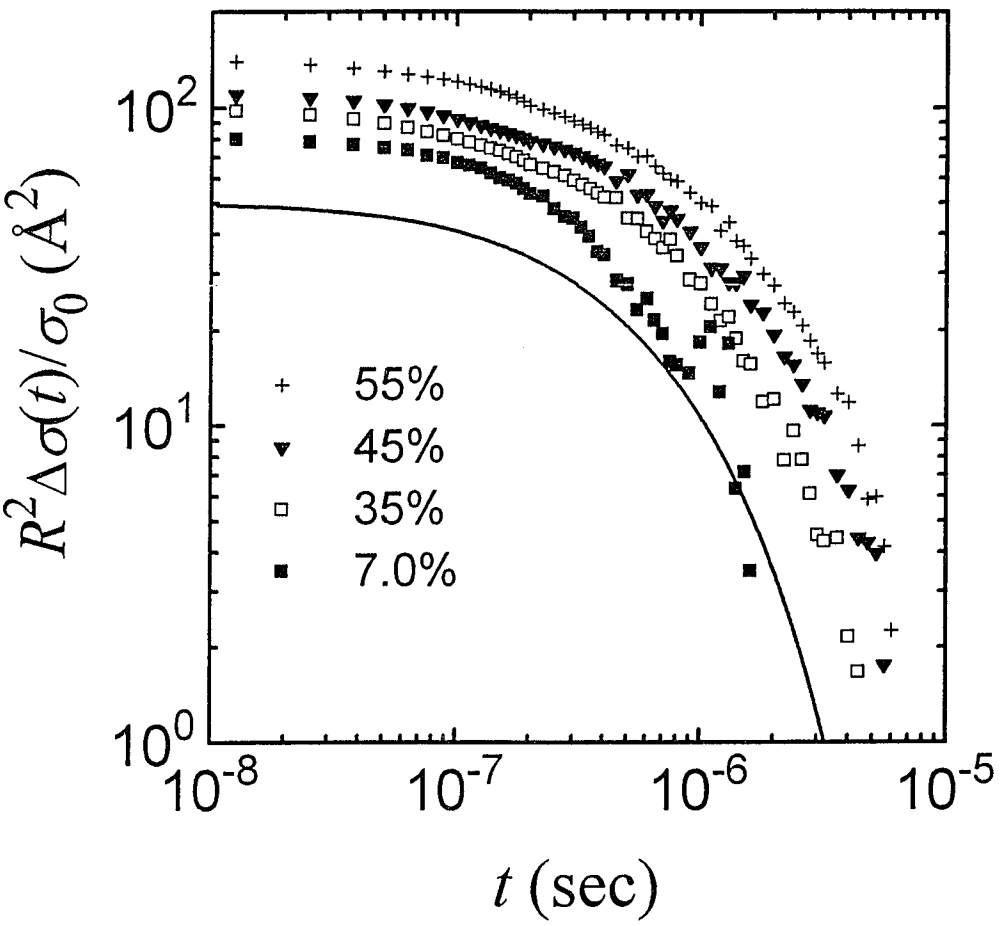
$R^2\Delta\sigma(t)/\sigma_0$ (Å^2)
10^2
10^1
10^0
55%
45%
35%
7.0%
10^{-8}
10^{-7}
10^{-6}
10^{-5}
t (sec)

Fig. 6.5

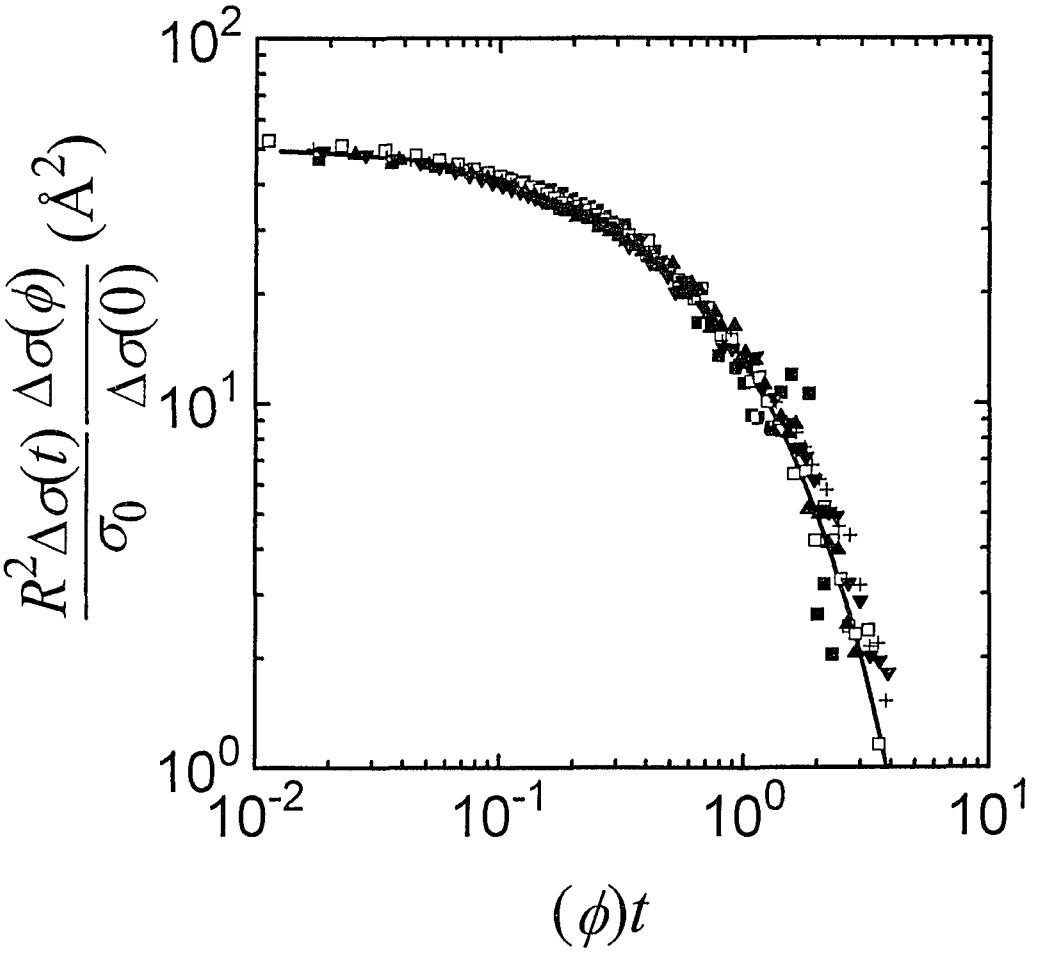
10^2
10^1
10^0
10^{-2}
10^{-1}
10^0
10^1
$\frac{R^2\Delta\sigma(t)}{\sigma_0}\frac{\Delta\sigma(\phi)}{\Delta\sigma(0)}$ (Å^2)
$(\phi)t$

Fig. 6.6

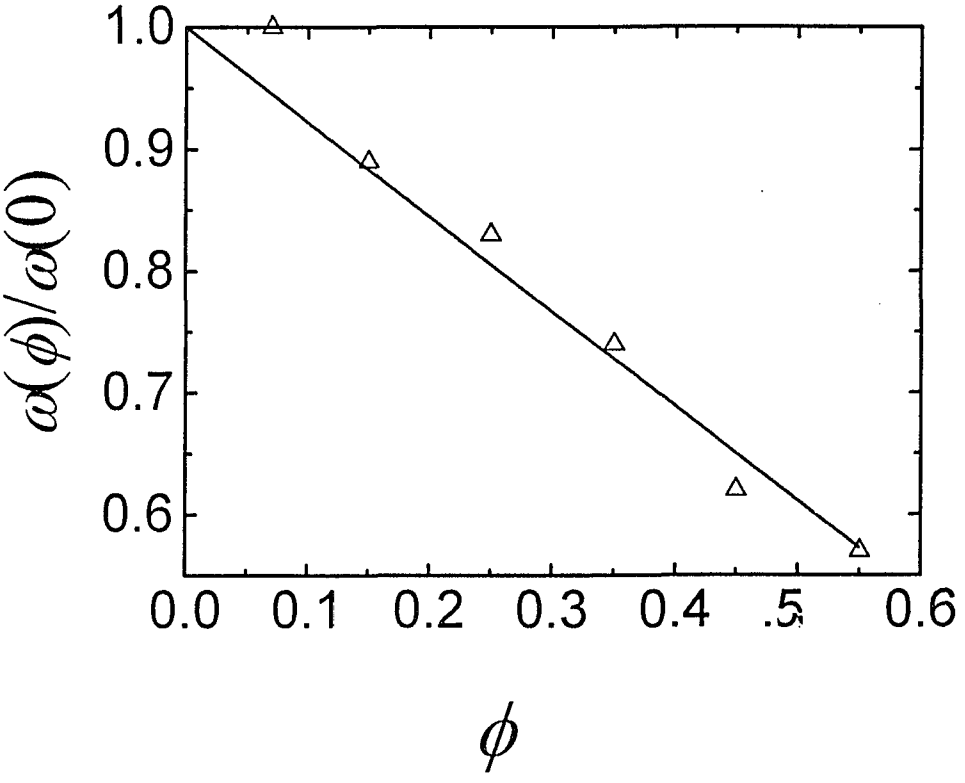

Fig. 6.7

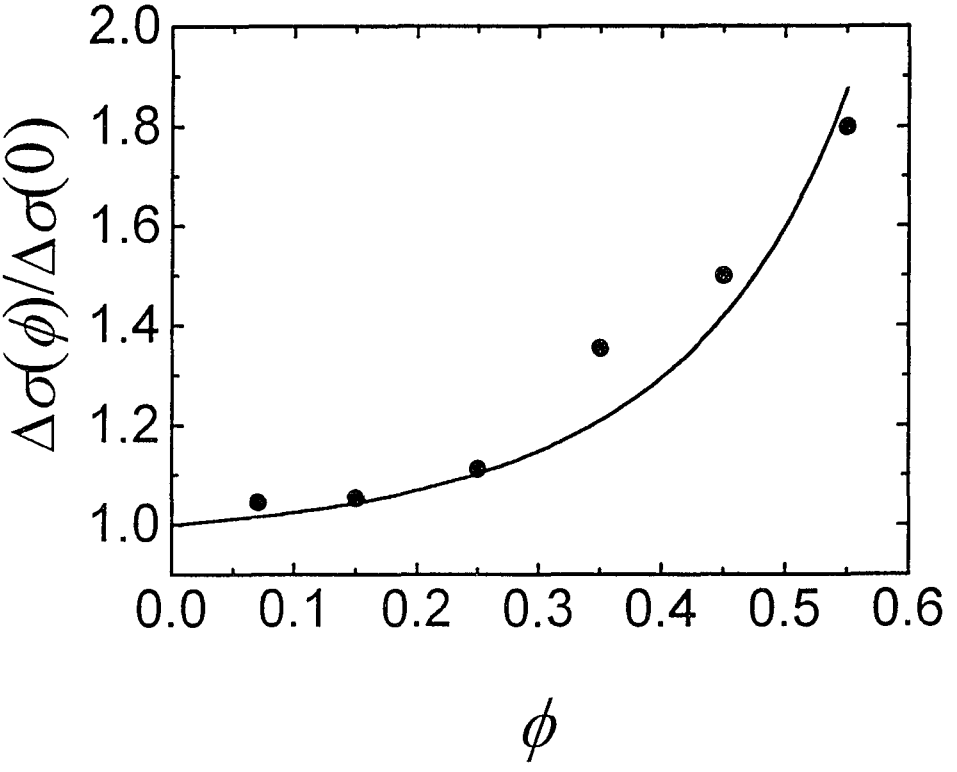
2.0
1.8
1.6
1.4
1.2
1.0
$\Delta\sigma(\phi)/\Delta\sigma(0)$
0.0
0.1
0.2
0.3
0.4
0.5
0.6
ϕ

Fig. 6.8

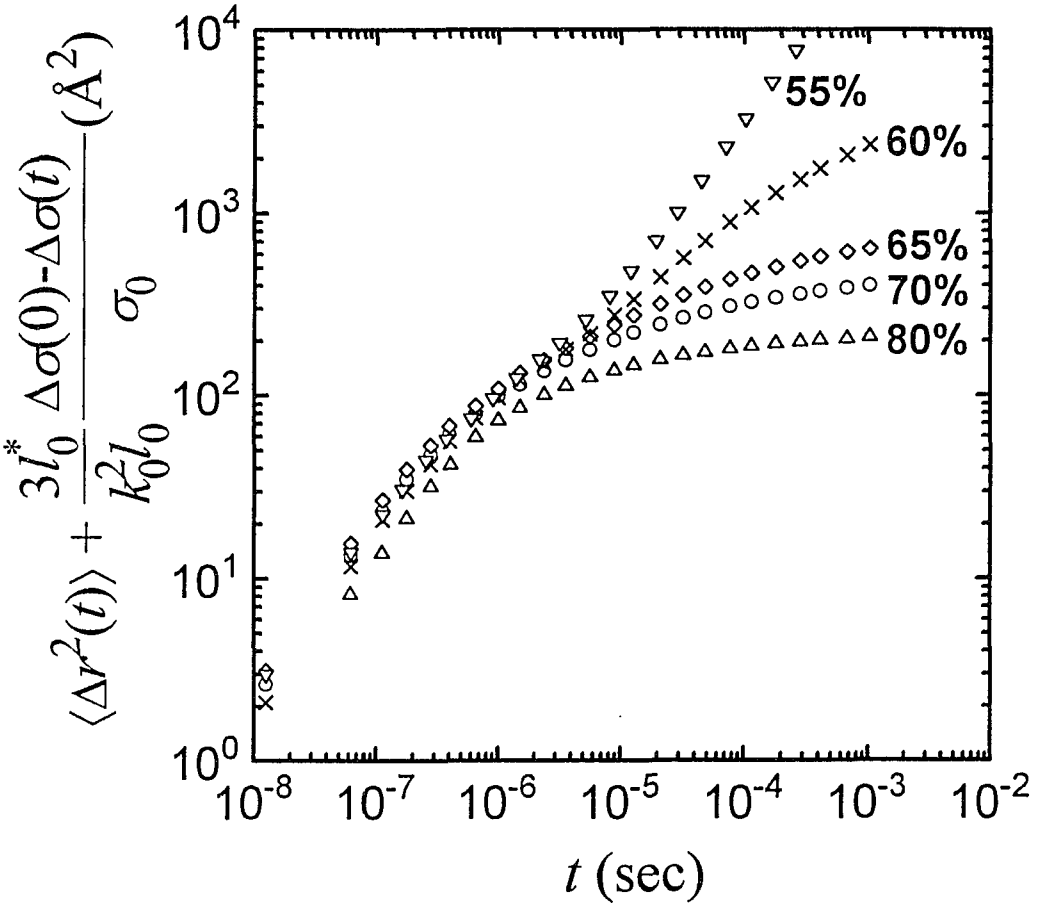
$\langle \Delta r^2(t) \rangle + \frac{3l_0^*}{k_0^2 l_0} \frac{\Delta\sigma(0)-\Delta\sigma(t)}{\sigma_0}$ (Å^2)
10^4
10^3
10^2
10^1
10^0
55%
60%
65%
70%
80%
10^{-8}
10^{-7}
10^{-6}
10^{-5}
10^{-4}
10^{-3}
10^{-2}
t (sec)

Fig. 6.9

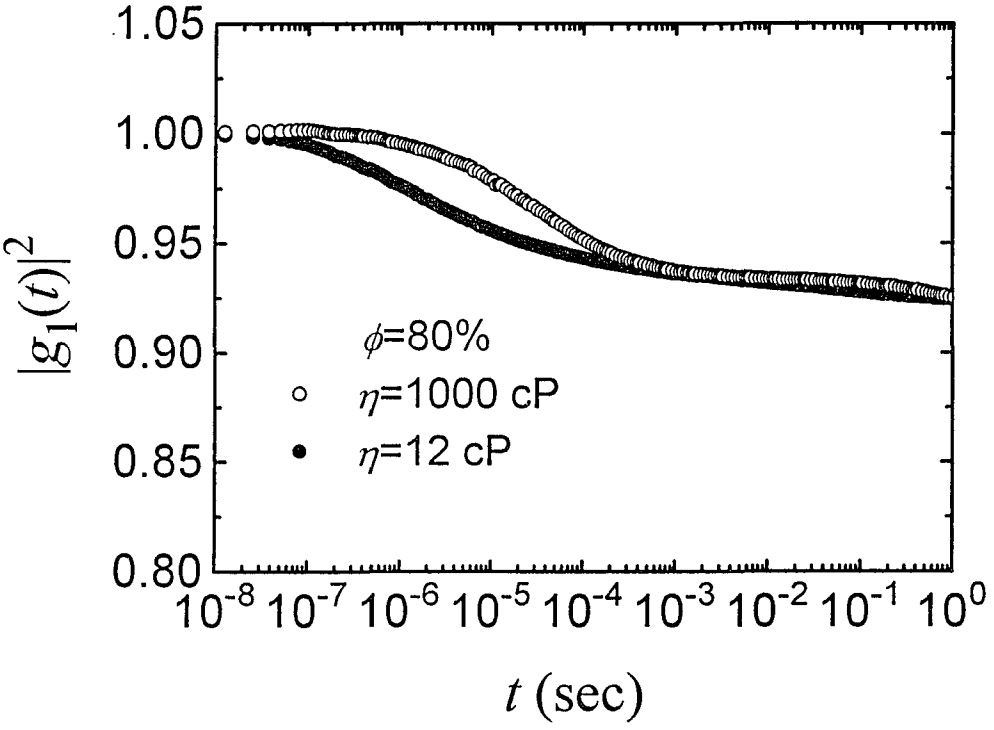
1.05
1.00
0.95
0.90
0.85
0.80
$|g_1(t)|^2$
ϕ=80%
η=1000 cP
η=12 cP
10^{-8} 10^{-7} 10^{-6} 10^{-5} 10^{-4} 10^{-3} 10^{-2} 10^{-1} 10^{0}
t (sec)

Fig. 6.10

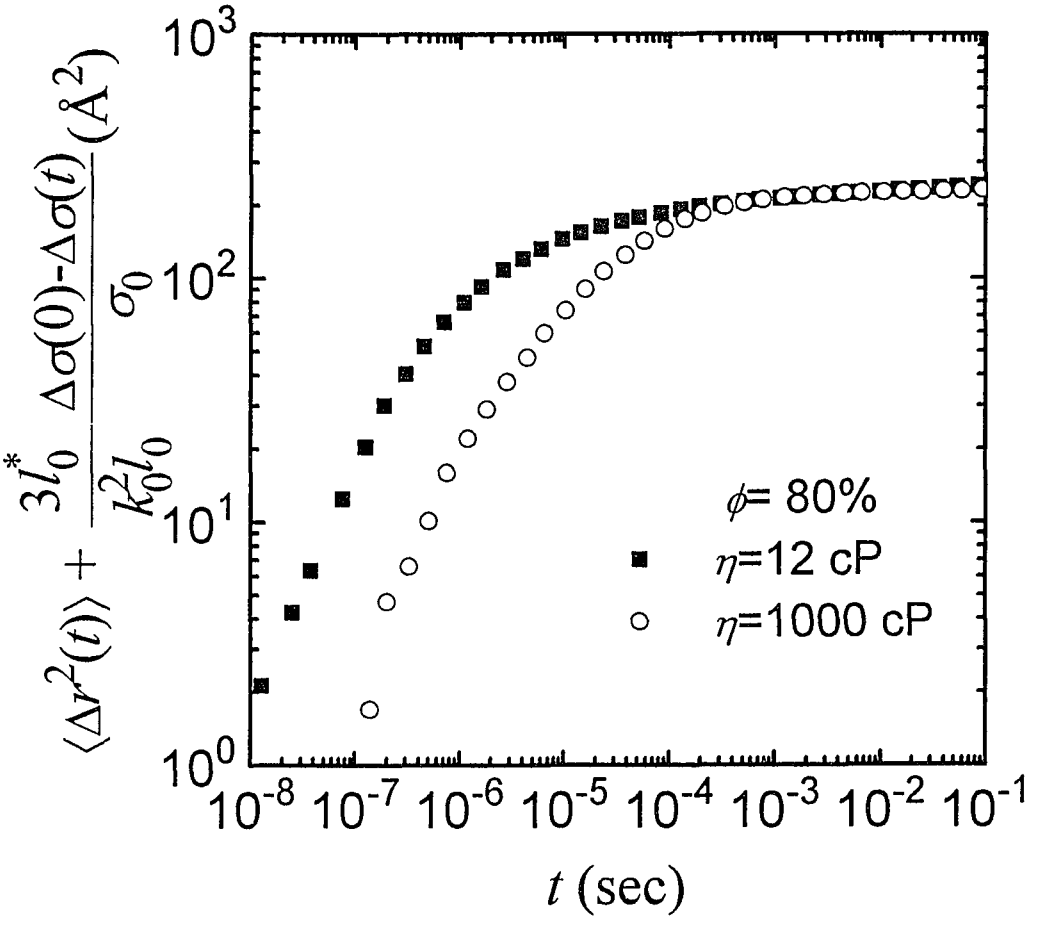
$\langle \Delta r^2(t) \rangle + \frac{3l_0^*}{k_0^2 l_0} \frac{\Delta\sigma(0)-\Delta\sigma(t)}{\sigma_0} (\text{Å}^2)$
10^3
10^2
10^1
10^0
10^{-8} 10^{-7} 10^{-6} 10^{-5} 10^{-4} 10^{-3} 10^{-2} 10^{-1}
t (sec)
ϕ= 80%
η=12 cP
η=1000 cP

Fig. 6.11

Biliography

Becher, P., *Emulsions: Theory and Practice* (Reinhold, New York, 1965).

Beenakker, C.W.J. and Mazur, P. Physica **A126**, 349 (1984).

Beenakker, C.W.J. and Mazur, P. Physica **A120**, 388 (1983).

Berne, B.J. and Pecora, R., *Dynamic Light Scattering*; Wiley; New York, 1976

Bibette, J. Roux, D. and Nallet, F., *Phys. Rev. Lett.* **65** 2470 (1990).

Bibette, J., *J. Coll. Inter. Sci.* **147** 474 (1991).

Bibette, J. Roux, D. and Pouligny B., *J. Physique* II **2** 401 (1992).

Bibette, J., Morse, D.C. Witten, T.A. and Weitz, D.A., *Phys. Rev. Lett.* **69** 2439 (1992).

Brady, J.F. and Bossis, G. Ann. Rev. Fluid. Mech. **20**, 111 (1988).

Brady, J.F., *J. Chem. Phys.* **99**, 567 (1993).

Brown, R.G.W., Ridley, K.D. and Rarity, J.G., *Appl. Opt.* **26** 2383 (1987).

Brown, R.G.W., *Appl. Opt.* **26** 4846 (1987).

Burstyn, H.C. and Sengers, J.V., Phys. Rev. **A27**, 1071 (1983).

Cai, W., pre-print

Choi, S.J. and Schowalter, W.R., *Phys. Fluids* **18**, 420 (1974)

Chu, B. *Laser Light Scattering,* Academic: New York, 1974.

Clercx, H.J.H. and Schram, P.P. J.M., *Physica* **174A**, 325 (1991).

Cox, R.G., *J. Fluid Mech.* **37** 601 (1969).

Cummins, H.Z., Du, W.M., Fuchs, M., Götze, W., Hilebrand, S., Latz, A., Li, G., and Tao, N.J., *Phys. Rev.* **E47**, 4223 (1993)

Cummins, H.Z., Pike, E.R. eds., *Photon Correlation and light spectroscopy*. Plenum, New York, 1973.

Cummins, H.Z., Pike, E.R. eds., *Photon Correlation Spectroscopy and velocimetry*, Plenum Press, New York, 1976.

Dautet, H., Deschamps, P., Dion, B., MacGregor, A.D., McIntyre, R.J.,Trottier, C. and Webb, P.P., *Appl. Opt.* **32** 3894 (1993).

de Gennes, P.G. *Scaling Concepts in Polymer Physics* (Cornell University Press, Ithaca, 1979).

Dodd, T., Sangani, A.S., Hammer, D.A. and Koch, D.L., *J. Fluid Mech.* (1995), in press.

Dhadwal, H.S. and Chu, B., *Rev. Sci. Instrum.* **60** 845 (1989).

Duwe, H.P., Kaes, J. and Sackmann, E., *J. Phys.* (Paris) **51** 945 (1990).

Einstein, A., *Ann. d. Physik* **17** 549 (1905).

Farago, B., Richter, D., Huang, J.S, Safran, S.A. and Milner, S.T., *Phys. Rev. Lett.* **65** 3348 (1990).

Fuchs, M. Hofacker, I. and Latz, A. *Phys. Rev.* **A45** 898 (1992).

Fraden, S. and Mret, G. *Phys. Rev. Lett.* **65** 512 (1990).

Götze, W., *J. Phys.* : *Condens. Matter* **2** 8485 (1990).

Götze, W. and Sjögren, L., *Rep. Prog. Phys.* **55** 241 (1992).

Haller, H.R., Destor, C. and Cannel, D.S., *Rev. Sci. Instrum.* **54** 973 (1983).

Hansen, J.P. and McDonald, I.R., *Theory of Simple Liquid*, Academic Press, San Diego, 1985.

Happel, J. and Brenner, H. *Low-Reynolds Number Hydrodynamics* (Martinus Nijhoff, Dordrecht, 1986).

Hasimoto, H., *J. Fluid Mech.* **5**, 317 (1959).

Hess, W. and Klein, R. *Adv. Phys.* **32**, 173 (1983).

Hinch, E.J., *J. Fluid Mech.* **72**, 499 (1975).

Huang, J.S., Milner, S.T. Farago, B. and Richter, D., *Phys. Rev. Lett.* **59** 2600 (1987).

Ishimaru, A., *Wave Propagation and Scattering in Random Media.* Academic; New York 1978

Jäckle, J. *Rep. Proc. Phys.* **49** 171 (1986).

Jones, R.B. and Pusey, P.N., . **42,** 137 (1991).

Kao, M.H., Yodh, A.G. and Pine, D.J. *Phys. Rev. Lett.* **70**, 242 (1993).

Katyl, R.H. and Ingard, U., *Phys. Rev. Lett.* **20** 248 (1968).

Kerker, Milton, *The Scattering of Light and Other Electromagnetic Radiation* (Academic, New York, 1969).

Ladd, Anthony. J.C., Hu Gang, Zhu, J.X. Weitz, D.A., *Phys. Rev. Lett.* **74** 318 (1995).

Ladd, A.J.C., *J. Fluid Mech.* **271**, 285 (1994).

Ladd, A.J.C., *J. Fluid Mech.* **271**, 311 (1994).

Ladd, A.J.C., *Phys. Rev. Lett.* **70**, 1339 (1993).

Ladd, A.J.C., *J. Chem. Phys.* **88**, 5051 (1988).

Ladd, A.J.C., Colvin, M.E. and Frenkel, D., *Phys. Rev. Lett.* **60**, 975 (1988).

Ladd, A.J.C., *J. Chem. Phys.* **93**, 3484 (1990).

Ladd, A.J.C., Hu Gang, Zhu, J.X. and Weitz, D.A., *Phys. Rev. E*, in press

Lagendijk, A., Vreeker, R. and DeVries, P., *Phys. Lett.* **A136** 81 (1989)

Lamb, H., *Hydrodynamics* (Dover, New York, 1932).

Landau, L.D. and Lifshitz, E.M., *Fluid Mechanics* (Addison-Wesley, London, 1959).

Lissant, K.J., *Emulsion and Emulsion Technology*, Vol. **6**, M. Dekker, New York, 1974

Lissant, K.J., *Demulsification: Insustrial Applications*; Surface Science Series **13** Dekker: New York, 1983.

MacKintosh, F.C. and John, S. *Phys. Rev.* B **40**, 2383 (1989).

Maret, G. and Wolf, P.E., *Z. Phys.* **B65** 409 (1987).

Mason, T.G., et. al., *Phys. Rev. Lett.*, submitted.

Milner, S.T. and Liu, A.J., Phys. Rev. E **48**, 449 (1993).

O'Donnell, K.A., *J. Opt. Soc. Am.* **72** 191 (1982).

Pine, D.J., Weitz, D.A., Chaikin, P.M. and Herbolzheimer, E., *Phys. Rev. Lett.* **60** 1134 (1988).

Pine, D.J., Weitz, D.A., Zhu, J.Z. and Herbolzheimer, E., *J. Phys.* (France) **51** 2101 (1990).

Pine, D.J., Weitz, D.A., Maret, G., Wolf, P.E., Chaikin, P.M. and Herbolzheimer, E., in *Scattering and Localization of Classical Waves in Random Media*, Sheng, P., Ed., World Scientific, Singapore, 1990.

Pusey, P.N. and Tough, R.J., *Faraday Disc. Chem. Soc.* **76** 123 (1983).

Pusey, P.N., *J. Physique* **48** 709 (1987).

Pusey, P. N. and van Megen, *Nature* (London) **320** 340 (1986).

Pusey, P. N. and van Megen, W., *Phys. Rev. Lett.* **59** 2083 (1987).

Pusey, P. N. and van Megen, *Physica*, **A157** 705 (1989).

Pusey, P.N. and Tough, R.J.A. in *Dynamic Light Scattering: Applications of Photon Correlation Spectroscopy*, edited by R. Pecora (Plenum, New York, 1985).

Qiu, X., Wu, X.L., Xue, J.Z., Weitz, D.A. and Chaikin, P.M., *Phys. Rev. Lett.* **65** 516 (1990).

Ricka, J., *Appl. Opt.* **32** 2860 (1993).

Roson, M.J., *Surface and Interfacial Phenomena*, 2nd Ed.; Wiley, New York, 1989.

Russel, W.R., D.A. Saville and Schowalter, W.R., *Colloidal Dispersions*, Cambridge; New York, 1989.

Safinya, C,R., Roux, D. Smith, G.S., Sinha, S.K., Dimon, P., Clark, N.A. and Belloq, A.M., *Phys. Rev. Lett.* **57** 2718 (1986).

Sanyal, M.K., Sinha, S.K., Huang, K.G. and Ocko, B.M., *Phys. Rev. Lett.* **66** 628 (1991).

Schramm, L.L. *Emulsions*: Fundamentals and Applications in the Petroleum Industry, American Chemistry Society, Washington, DC 1992.

Schwartz, M. and Edwards, S.F., *Physica* **A167**, 589 (1990)

Sumner, C.G., Clayton's *The Theory of Emulsions and Their Technical Treatment*, 5th Ed. Blakiston, New York, 1954.

Tanaka, T. and Benedek, G.B., *Appl. Opt.* **14** 189 (1975).

Uhlenbeck, G.E. and Ornstein, L.S. *Phys. Rev.* **36** 823 (1930).

van Megen, W. and Pusey, P. N., *Phys. Rev.* **A43** 5429 (1991).

van Megen, W. and Pusey, P. N., *Phys. Rev.* **E47** 248 (1993).

van Megen, W., Ottewill, R.H. Owens, S.M. and Pusey, P.N., *J. Chem. Phys.* **82**, 508 (1985).

Van Saarloos, W. and Mazur, P., *Physica* **A120**, 77 (1983).

Vrij, A., *Pure Appl. Chem.* **48** 471 (1976).

Weitz, D.A., Pine, D.J. Pusey, P.N. , and Tough, R.J.A., *Phys. Rev. Lett.* **63**, 1747 (1989).

Weitz, D.A. and Pine, D.J., Diffusing-Wave Spectroscopy, in "*Dynamic Light Scattering*"Brown, W., Ed., Oxford University Press, Oxford (1992).

Weitz, D.A, Zhu, J.X., Durian, D.J. and Pine, D.J., Principle and Applicaitons of Diffusing-Wave Spectroscopy, in *Structure and Dynamics of Strongly Interacting Colloids and Supramolecular Aggregates in solution*, Chen, S.H., Huang, J.S. and Tartaglia, P., Ed., Kluwer, Dordrecht (1992).

Weitz, D.A., Zhu, J.X., Durian, D.J., Hu Gang and Pine, D.J., *Physica Scripta* **T49** 610 (1993).

Wang, M.C. and Uhlenbeck, G.E., *Rev. Mod. Phys.*, **17** 323 (1945).

Wolf, P.E., Maret, G. Akkermans, E. and Maynard, R., *J. Phys.* (France) **49** 63 (1988).

Xue, J.Z., Wu, X.L., Pine, D.J. and Chaikin, P.M., *Phys. Rev.* **A45**, 989 (1992).

Zhu, J.X., Weitz, D.A. and Klein, R. in *Localization and Propagation of Classical Waves in Random and Periodic Structures*, Soukoulis, C.M., Ed., Plenum, New York, 1993.

Zhu, J.X., Pine, D.J. and Weitz, D.A., *Phys. Rev.* **A44** 3948 (1991).

Zhu, J.X. *et al.*, *Phys. Rev. Lett.* **68**, 2559 (1992).

Zúñiga, I. and Español, P., *Phys. Rev. Lett.* **71**, 3665 (1993).

Zwanzig, R. and Bixon, M., *Phys. Rev.* **A2**, 2005 (1970).